UNIVERSITY OF CALIFORNIA
RIVERSIDE

Properties and Applications of Composites With One-Dimensional van der Waals Materials

A Dissertation submitted in partial satisfaction
of the requirements for the degree of

Doctor of Philosophy

in

Electrical Engineering

by

Zahra Barani Beiranvand

September 2022

Dissertation Committee:
Dr. Alexander A. Balandin, Chairperson
Dr. Alexander Khitun
Dr. Xi Chen

The Dissertation of Zahra Barani Beiranvand is approved:

Committee Chairperson

University of California, Riverside

Acknowledgments

First and foremost, I would like to express my gratitude to my esteemed supervisor, Professor Alexander Balandin, for giving me the privilege and honor to join and work in his laboratories, Phonon Optimized Engineered Materials (POEM) and the Nano Device Laboratory (NDL). His guidance and advice carried me throughout this research. I am certain without his help, support, and encouragement, I could not have made any progress in my academic career.

My gratitude extends to Dr. Alexander Khitun and Dr. Xi Chen for accepting to serve on my dissertation committee. Their immense knowledge and vast experience have always encouraged me in my academic research.

My appreciation for Dr. Fariborz Kargar is beyond words. Without his great help in theoretical interpretation and, more importantly, *his tea preparation skills*, I would not be able to undertake this journey.

I am deeply indebted to Dr. Roger Lake, Dr. Sergey Rumyantsev, Dr. Lorenzo Mangolini, Dr. Tina Salguero, Dr. Yassamin Ghafouri, and Dr. Mykhaylo Balinsky, with whom I had the honor of collaborating on different projects.

I am extremely grateful to my parents, Ali Barani and Banoo Yavarnezhad, for all their love, care, and sacrifices. I sincerely appreciate my sister, Maryam Barani, my brother, Reza Barani, and my beautiful niece, Afra Kashefi. They encouraged and supported me in every single step toward this path.

I would like to express my sincerest appreciation to some of my most influential friends and colleagues: Bahman Kargar, Roghiyeh Vosoogh, Mehrdad Kargar, Marie Balandin,

Dr. Vahid Mardanloo, Dr. Saba Baraghani, Dr. Elahe Aghapour, Dr. Salar Rahili, Dr. Evan Wigton-Jones, Sara Shirmohammad, Dr. Ruben Arash Salgado, Dr. Amirmahdi Mohammadzadeh, Dr. Subhajit Ghosh and all the previous and current students in POEM and NDL labs.

Finally, many thanks to my best friends, Elahe Babaei, Amin Zanganeh, Dr. Khosro Monsef, Maedeh Taheri, Narges Zarinkamar, Aneseh Mehrak; they are the definition of trust and friendship.

The text and figures of this dissertation, in part or in full, are a reprint of the material as it appears in the following journals and/or proceedings [1–3]:

[1] Z. Barani, F. Kargar, Y. Ghafouri, S. Ghosh, K. Godziszewski, S. Baraghani, Y. Yashchyshyn, G. Cywiński, S. Rumyantsev, T.T. Salguero, A.A. Balandin, Electrically Insulating Flexible Films with Quasi-1D van der Waals Fillers as Efficient Electromagnetic Shields in the GHz and Sub-THz Frequency Bands, Advanced Materials. 33 (2021) 2007286. https://doi.org/10.1002/ADMA.202007286. Reprinted with permission, Copyright © 2021, Wiley - VCH VERLAG GMBH & CO. KGAA.

[2] Z. Barani, F. Kargar, Y. Ghafouri, S. Baraghani, S. Sudhindra, A. Mohammadzadeh, T.T. Salguero, A.A. Balandin, Electromagnetic-Polarization-Selective Composites with Quasi-1D van der Waals Fillers: Nanoscale Material Functionality That Mimics Macroscopic Systems, ACS Applied Materials & Interfaces. 13 (2021) 21527–21533.

https://doi.org/10.1021/acsami.1c03204. Reprinted with permission, Copyright © 2021 American Chemical Society.

[3] Z. Barani, K. Stelmaszczyk, F. Kargar, Y. Yashchyshyn, G. Cywiński, S. Rumyantsev, A.A. Balandin, Efficient terahertz radiation absorption by dilute graphene composites, Applied Physics Letters. 120 (2022) 063104. https://doi.org/10.1063/5.0079891. Reprinted with permission, Copyright © 2022 AIP Publications.

The co-author A. A. Balandin, listed in the above publications, directed and supervised the research, which forms the basis for this dissertation. The work in Balandin group was supported, in part, by the National Science Foundation (NSF) program Designing Materials to Revolutionize and Engineer our Future (DMREF) via a project DMR-1921958 entitled Collaborative Research: Data-Driven Discovery of Synthesis Pathways and Distinguishing Electronic Phenomena of 1D van der Waals Bonded Solids; the Semiconductor Research Corporation (SRC) contract 2018-NM-2796 entitled One-Dimensional Single-Crystal van-der-Waals Metals: Ultimately-Downscaled Interconnects with Exceptional Current-Carrying Capacity and Reliability; and by the Proof of Concept (POC) project of the Office of Technology Partnerships (OTP), the University of California, Riverside (UCR).

ABSTRACT OF THE DISSERTATION

Properties and Applications of Composites With One-Dimensional van der Waals Materials

by

Zahra Barani Beiranvand

Doctor of Philosophy, Graduate Program in Electrical Engineering
University of California, Riverside, September 2022
Dr. Alexander A. Balandin, Chairperson

This dissertation research addresses the properties and engineering applications of polymer-based composites with fillers comprised of quasi-one-dimensional (1D) van der Waals materials. The investigated materials include transition metal trichalcogenides containing 1D structural motifs that enable their exfoliation into bundles of atomic threads. These quasi-1D van der Waals nanostructures are characterized by extremely large aspect ratios of up to ~10^6. In the course of the investigation, we developed original techniques and methods for preparing composites with quasi-1D van der Walls fillers. It was established that the resulting polymer composites with low loadings of quasi-1D $TaSe_3$ fillers have excellent electromagnetic interference shielding properties in the X-band GHz and EHF sub-THz frequency ranges. The unusual feature of these composites is that they

provide electromagnetic shielding while remaining DC electrically insulating. Such unique characteristics were attributed to the effective coupling of the electromagnetic waves to the high-aspect-ratio electrically-conductive $TaSe_3$ atomic-thread bundles even when the filler concentration is below the electrical percolation threshold. In addition, we developed approaches for synthesizing polymer composite films with aligned quasi-1D $TaSe_3$ van der Waals fillers. The composite material functionality, embedded at the nanoscale level, was achieved by mimicking the design of an electromagnetic aperture grid antenna. Measurements conducted in the X-band frequency range demonstrate that the electromagnetic transmission through such films can be varied significantly by changing the relative orientations of the quasi-1D fillers and the polarization of the electromagnetic wave. The results obtained in this dissertation research are important for high-frequency communication technologies, which require electromagnetic shielding films that are flexible, lightweight, corrosion-resistant, inexpensive, and electrically insulating. The polarization-sensitive polymer films with quasi-1D fillers can be used in future communication systems that require selective electromagnetic interference shielding.

Table of Contents

List of Figures

List of Tables

Chapter 1 One-Dimensional van der Waals Materials

1.1 Properties of Quasi-One-Dimensional vdW Materials

The explosive growth of interest in two-dimensional (2D) layered van der Waals materials, such as graphene and transition metal dichalcogenides (TMDs) MX_2, where M = transition metals and X = S, Se, Te, has resulted in numerous breakthroughs in physics and is expected to lead to important practical applications [1–8]. Recently, a different group of layered van der Waals materials with quasi-one-dimensional (1D) crystal structures has attracted significant attention: the transition metal trichalcogenides (TMTs). These compounds contain 1D motifs comprised of MX_3 atomic chains that are weakly bound together by van der Waals forces or chalcogen interactions. Examples of such materials include TiS_3, NbS_3, $TaSe_3$, and $ZrTe_3$ [9–16]. MX_3 materials exfoliate into nanowire- and nanoribbon-type structures, as opposed to atomic planes of quasi-2D van der Waals MX_2 materials. We previously discovered that bundles of quasi-1D $TaSe_3$ atomic threads and $ZrTe_3$ nanoribbons could support high current densities of $J_B \sim 10\ \mathrm{MA/cm^2}$ and $J_B \sim 100\ \mathrm{MA/cm^2}$, respectively [12,13,17]. In this group of MX_3 materials, $TaSe_3$ is particularly interesting. Reported studies generally agree that it is a metal with superconducting properties at low temperatures, although some studies suggest that it is semimetal [18–21]. The exact band and specifics of electron transport in bulk and

exfoliated nanowires of $TaSe_3$ at various temperatures are still under intensive debate. In this Proposal, we first demonstrate that quasi-1D van der Waals materials like $TaSe_3$ can be used as the high-aspect-ratio metallic fillers in polymer composites to provide important functionality—efficient electromagnetic interference (EMI) shielding—in a wide frequency range that is relevant to the current 5G and future communication technologies: X-band ($f = 8.2\ \mathrm{GHz} - 12.4\ \mathrm{GHz}$) and the extremely high frequency (EHF) band ($f = 220\ \mathrm{GHz} - 320\ \mathrm{GHz}$). In the end, we will provide the potential functionalities of these composites and a framework for future studies.

1.2 Quasi-One-Dimensional-Based Composites in EMI Applications

The proliferation of portable devices and wireless communications has led to problems with environmental electromagnetic pollution. There is a need for more efficient EMI shielding materials characterized by low weight, mechanical stability, resistance to oxidation, flexibility, and ease of manufacturing. Many applications also require EMI shielding films to be electrically insulating to avoid short-circuiting of electronic components. The conventional materials for EMI shielding are metals, which are utilized as coatings and enclosures [22]. Metals have charge carrier concentrations that enable them to block EM waves mostly by reflection. However, metallic EMI shields are heavy and prone to oxidation. An alternative approach to EMI shielding is based on the use of polymers containing electrically conductive fillers [23–25]. The first generation of polymer composites for EMI shielding utilized large loading fractions of metallic particles, such

that their concentrations are above the electrical *percolation threshold*, resulting in overall electrically conductive films. The high loading fraction of metallic fillers are required to provide sufficient EMI shieling at a given thickness of the film. Recently, attention has turned to carbon allotrope fillers, including carbon nanotubes and graphene, and transition metal carbide fillers referred to as MXenes [23,26–31]. For example, we demonstrated efficient EMI shielding in the wide GHz and sub-THz frequency ranges with high-loading graphene composites [32,33]. The advantages of quasi-2D graphene fillers include low weight, high thermal stability, anti-corrosive properties, and low cost at mass production. Mxenes, are metallic-like fillers that are reported to provide high EMI shielding in the X-band frequency range. Being highly electrically conductive, the MXene-based composites and films can be utilized in applications where the electrical insulation among the components is not a design parameter. Here, we demonstrate that quasi-1D van der Waals materials can be used as efficient fillers for EMI shielding that, in certain aspects, outperform their quasi-2D counterparts. The synthesized composites and films with these fillers provide electrical insulation.

1.3 $TaSe_3$: A Quasi-One-Dimensional Material for EMI Applications

For experiments with quasi-1D fillers in electrically insulating films for EM shielding, we selected $TaSe_3$. This quasi-1D van der Waals material is well-suited for this application due to its metallic electronic structure and good stability with respect to oxidation. The fact that this material revealed extremely high current densities when exfoliated into the

bundles of atomic threads was an additional important factor [12]. Recent interest in $TaSe_3$ has included studies of its topological phases [20,34–36], the effect of strain on its metallic *vs.* semiconducting states [37], low-temperature charge density wave states [21], and our own work characterizing its current carrying capacity and low-frequency electronic noise [38].

1.3.1 Material Growth and Structure

In this study, the bulk crystalline $TaSe_3$ was prepared by iodine-mediated chemical vapor transport (CVT) from the element. A schematic of the growth procedure is presented in Figure **1-1** (a). 1.7315 g (9.57 mmol) of tantalum (STREM 99.98% purity) and 2.2718 g (28.8 mmol) of selenium (STREM 99.99% purity) were ground together gently with an agate mortar/pestle. This mixture was added to a 17.78 × 1 cm fused quartz ampule along with 62.3 mg iodine (J.T. Baker, 99.9% purity). The ampule was evacuated and backfilled with Ar three times while submerged in an acetonitrile/dry ice bath, then flame sealed under vacuum. The ampule was placed in a Carbolite EZS 12/450B three-zone horizontal tube furnace and heated to 750 – 650 °C (source zone – growth zone) for 336 h. After the ampule had cooled to room temperature and was opened, the isolated shiny black crystals were left to sit in a fume hood for 1-2 h to allow excess iodine to sublime. $TaSe_3$ crystals grew preferentially along the *b*-axis, leading to ribbon- or needle-like, filamentary morphologies ranging from less than one micron to tens of microns in width (Figure **1-1** (b)).

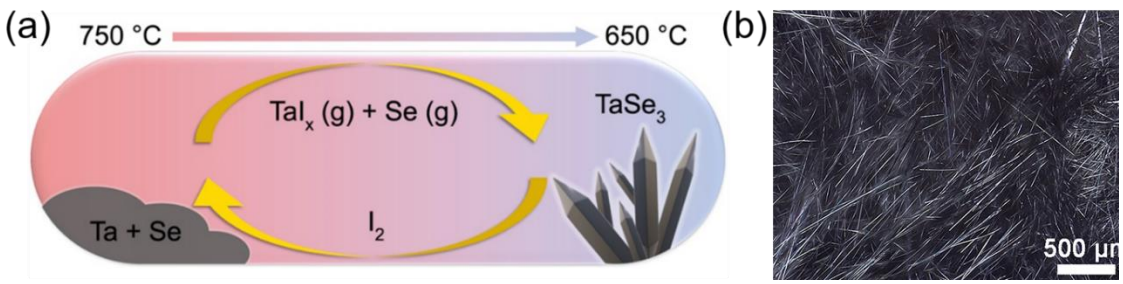

Figure 1-1: Crystal growth and image of bulk material. (a) A schematic illustrating the iodine-mediated CVT used in this study to prepare bulk crystalline $TaSe_3$. (b) Optical image of as-synthesized $TaSe_3$ crystals. Reprinted with permission from Barani et al., Advanced Materials. 33 (2021) 2007286, Copyright © 2021, Wiley - VCH VERLAG GMBH & CO. KGAA.

The room temperature, monoclinic crystal structure of $TaSe_3$ (Figure **1-2** (a)) exhibits aligned chains of trigonal prismatic [$TaSe_6$] units oriented along the *b*-axis [39]. These chains are assembled into corrugated bilayers (sets of blue and purple chains in Figure **1-2** (a)) through Ta···Se interactions between adjacent chains. Neighboring bilayers are separated by van der Waals gaps.

1.3.2 Material Characterization

$TaSe_3$ samples for SEM-EDS were prepared by mounting the crystals on carbon tape and then mechanically exfoliating with Scotch™ tape. Data were acquired with an FEI Teneo FE-SEM instrument equipped with an Oxford Instruments X-MAX^N EDS detector at 10-20 keV. The scanning electron microscopy (SEM) image in Figure **1-2** (b) shows a $TaSe_3$ crystal that was freshly mechanically exfoliated for energy dispersive spectroscopy (EDS) analysis. EDS mapping shows an excellent overlap of Ta and Se (Figure **1-2** (c)), and

quantitative EDS averaged across the entire mapped area (SI) provides a slightly Se-deficient composition of $TaSe_{2.85}$ similar to other samples prepared by CVT [36]. The quantitative results from the energy-dispersive X-ray spectroscopy (EDS) analysis of the CVT-grown crystals are listed in Table **1-1**. The area-averaged atomic ratio of Se to Ta in the crystals used in this work is 2.85.

$TaSe_3$ samples for powder XRD were prepared by pressing bulk crystals into an aluminum mount. Data were acquired with a Bruker D8-Advance diffractometer (Co-Kα radiation) from 10-80 2θ at a rate of 0.1 s per step at 40 mA, 35 kV. Powder x-ray diffraction (XRD) is consistent with the anticipated monoclinic $TaSe_3$ structure, and it confirms the phase purity of the as-prepared material (Figure **1-2** (d)).

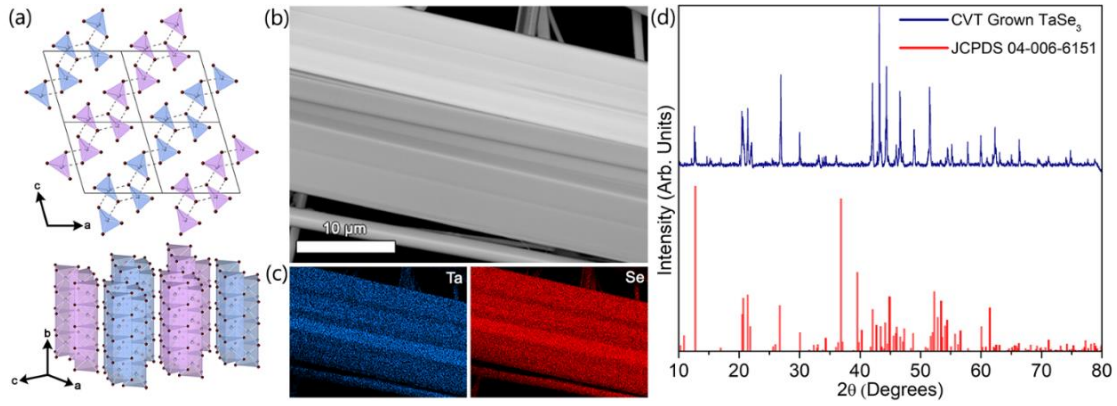

Figure 1-2: Structure and composition of as-synthesized $TaSe_3$. (a) Crystal structure of $TaSe_3$; red spheres represent Se and blue/purple spheres represent Ta. The parallelograms in the top panel outline unit cells viewed along the *b*-axis, perpendicular to the $TaSe_3$ chains. The side view in the bottom panel shows the quasi-1D nature of trigonal prismatic [$TaSe_6$] units extending along the *b*-axis. The corrugated bilayer nature of this structure is emphasized with the Ta···Se interchain interactions and the purple/blue coloring; bilayers are separated from their neighbors by van der Waals gaps. (b) SEM image of a mechanically-exfoliated $TaSe_3$ crystal. (c) Corresponding EDS mapping showing a uniform overlap of Ta and Se along the length of the crystal. (d) Powder XRD pattern of CVT-grown $TaSe_3$ crystals (blue) matching a reference pattern of monoclinic $TaSe_3$ (red). Reprinted with permission from Barani et al., Advanced Materials. 33 (2021) 2007286, Copyright © 2021, Wiley - VCH VERLAG GMBH & CO. KGAA.

Table 1-1: EDS characterization of the CVT-grown crystals

	Ta	Se	Se/Ta
Theoretical at. %	25.00	75.00	3.00
Experimental at. % (area-averaged EDS)	26.00	74.00	2.85

1.4 Sample Preparation

The preparation of composites with quasi-1D fillers involved chemical phase exfoliation and inclusion of high aspect-ratio exfoliated threads into three polymeric matrices of

sodium alginate (SA), epoxy, and a special type of UV-light cured polymer (UV-polymer) as the base. In samples in which SA and epoxy were used as the base polymers, the CVT-grown crystals were exfoliated and used. For UVP samples, the $TaSe_3$ was outsourced from HQ Graphene Inc. Here, we provide a detailed description of the liquid phase exfoliation and composite sample preparation.

1.4.1 Liquid Phase Exfoliation

For the liquid exfoliation process, we used two different solvents: DMF and acetone (see Figure **1-3** (a-c). In this study, although the exfoliation process using DMF takes much less time, we mostly used acetone owing to its shorter evaporation time.

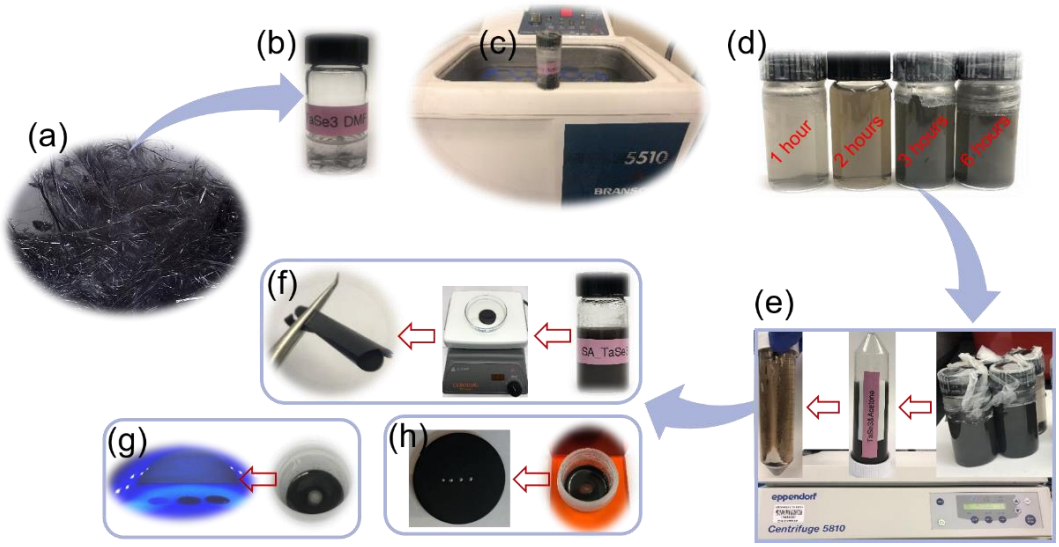

Figure 1-3: Liquid-phase exfoliation and composite preparation. (a) SEM image of fibrous $TaSe_3$ bundles. (b, c) $TaSe_3$ crystals and fibers added into DMF and acetone. Low-power bath sonication was used for the liquid phase exfoliation process. (d) The vials of $TaSe_3$ and acetone solution after one, two, three, and six hours of exfoliation. (e) After exfoliation, vials were centrifuged to separate the solid phase from the solution. (f, g) Synthesis of flexible polymeric films using sodium alginate and a special UV-cured polymer as the base matrix, respectively. (h) Optical image of the epoxy composite before and after solidification. Reprinted with permission from Barani et al., Advanced Materials. 33 (2021) 2007286, Copyright © 2021, Wiley - VCH VERLAG GMBH & CO. KGAA.

The bulk $TaSe_3$ crystals were filled into acetone with starting concentration of 0.5 mg/ml in 10 ml cylindrical vials and sonicated in a low-power sonic bath (Branson 5510) for several hours as shown in Figure **1-3** (c). The Temperature was kept under 25° C by continuously adding ice into the sonic bath. The vials were inspected visually every 1 to 2 hours to verify the quality of the dispersion as shown in Figure **1-3** (d). Note that the time needed for vials to be completely exfoliated was different even among those with the same volume fraction of $TaSe_3$ bundles. The optical microscopy analysis of the final exfoliated threads of $TaSe_3$ by acetone and DMF showed no significant difference (see **Figure 1-4**).

It could be related to the thickness and lateral dimensions of the different parts of the crystal. Next, the solution in all vials was poured into bigger vials (see Figure **1-3**(e)-middle) and centrifuged (Eppendorf Centrifuge 5810) at 7000 rpm for 5 to 10 minutes. The supernatant of the dispersion was collected and poured into a Peltier dish to dry for characterization purposes. The precipitant part of the dispersion, as well as some parts of the material which were stuck to the sidewalls of the vial after centrifugation, were collected and left in the ambient air, so the remaining portion of the solvent evaporated (Figure **1-3** (e)-left). The result is dark brown exfoliated $TaSe_3$ threads with different aspect ratios. The exfoliated threads were used to prepare the composites with different polymer bases for electrical conductivity and EMI shielding experiments (Figure **1-3** (f-h)).

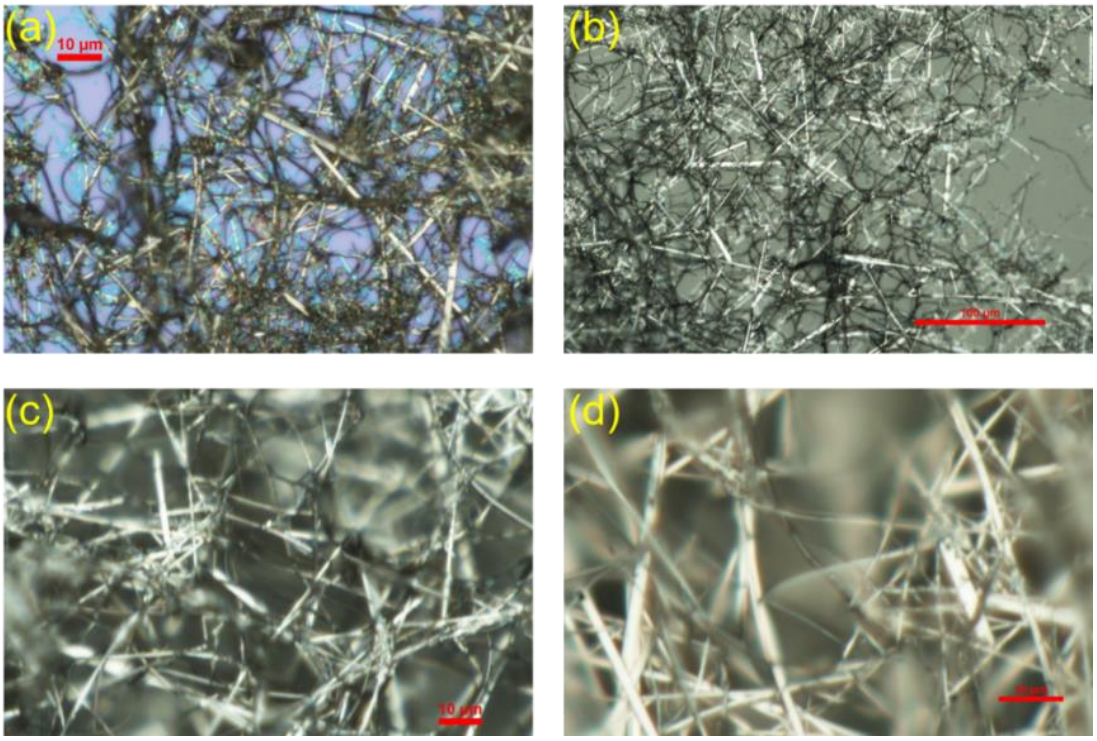

Figure 1-4: Optical images of liquid-phase exfoliated $TaSe_3$. (a) Microscopic images of $TaSe_3$ thread being completely exfoliated in DMF. (b-d) Microscopic images of $TaSe_3$ thread being completely exfoliated in acetone. Reprinted with permission from Barani et al., Advanced Materials. 33 (2021) 2007286, Copyright © 2021, Wiley - VCH VERLAG GMBH & CO. KGAA.

1.4.2 Composite Preparation

Three different polymers were used to make films and composites in this study:

Sodium Alginate (SA)/$TaSe_3$ flexible films: Commercially available sodium alginate powder was mixed with DI water with a ratio of 1mg/2ml, respectively. Using magnetic stir bars, the solution was mixed for about 3 hours on a hot plate set to 50 ºC. The $TaSe_3$ threads were weighed and added to the mixture. **Figure 1-3**-f-right shows the final mixture after stirring for almost one hour and sonicated for about 30 minutes. In the next step, the

solution was drop cast on a Peltier dish. The dish was placed on a hot plate at 50 ºC for less than one hour (see Figure **1-3** (f)-middle.) The final film was a dark brown flexible film shown in Figure **1-3** (f)-left.

UVP/$TaSe_3$ flexible films: An off-the-shelf polymer that cures under the illumination of UV light was used in this case. The $TaSe_3$ fillers were added to the UV polymer and were mixed at 500 rpm for 10 minutes using a high-shear speed mixer (Flacktek Inc.). The Final mixture was homogeneously dispersed, which is shown in Figure **1-3** (g). The mixture was then sandwiched between two pieces of nylons. Afterward, it was pressed gently until a thin film formed in between. The sandwich was left under the 36 W UV lamp for 2 minutes to cure. The final product is shown in Figure **1-3** (g)-left.

Epoxy/$TaSe_3$ composites: The epoxy resin (bisphenol-A-(epichlorohydrin) and the $TaSe_3$ fillers were mixed using the high-shear speed mixer (Flacktek Inc.) at 500 rpm for 10 minutes. Then, the homogeneous mixture of epoxy and fillers were put inside a vacuum chamber for ~10 minutes to extract the possibly trapped air bubbles. The curing agent (triethylenetetramine, Allied High-Tech Products, Inc.) was then added in the prescribed mass ratio of 12:100 with respect to the epoxy resin. The mixture was mixed at 300 rpm for about 10 minutes each, vacuumed, and then poured into special molds and left at room temperature for 8 hours (Figure **1-3** (h)-right.) Finally, the mixture was placed in an oven for ~2 hours at 50º C (Figure **1-3** (h)-left.). SEM images of the exfoliated fillers and fillers embedded in polymeric matrices are shown in Figure **1-5** (c, d).

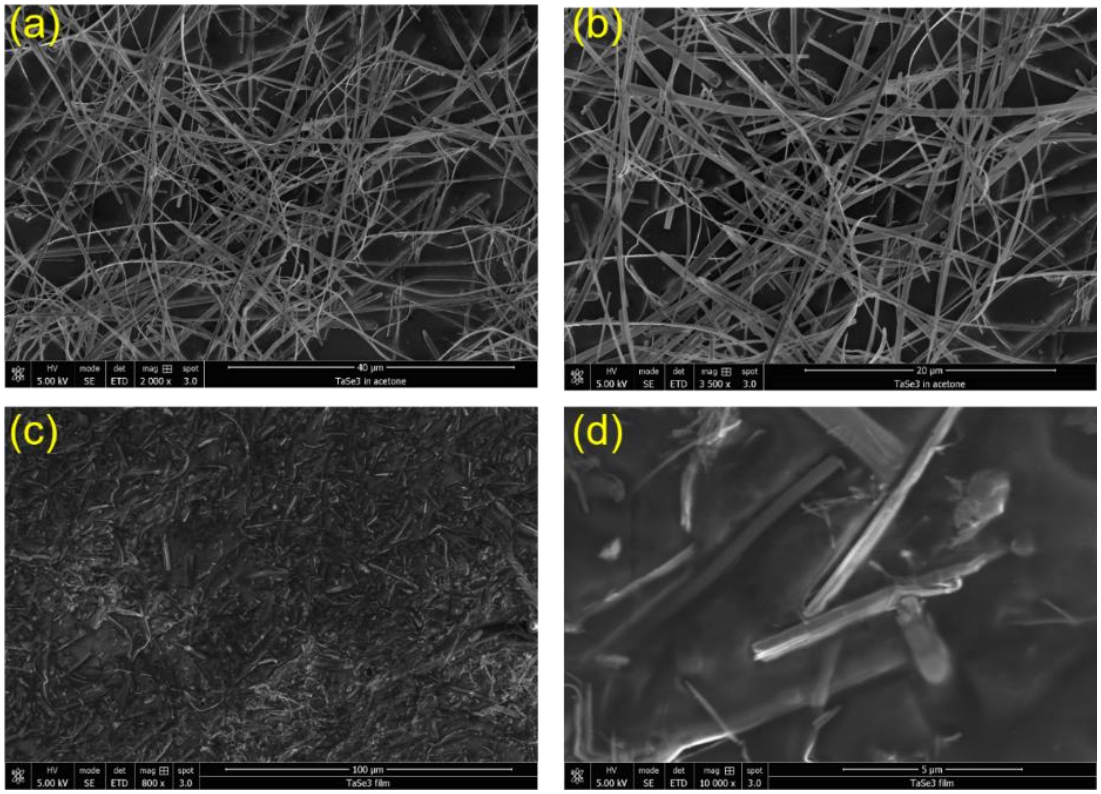

Figure 1-5: SEM images of the exfoliated threads and composites with TaSe3 as filler. (a,b) SEM images of $TaSe_3$ crystals and fibers separated using low-power bath sonication (c,d) The SEM images of the SA film containing about 3 vol. %. Reprinted with permission from Barani et al., Advanced Materials. 33 (2021) 2007286, Copyright © 2021, Wiley - VCH VERLAG GMBH & CO. KGAA.

Chapter 2 Polymeric Composites for EMI Applications

2.1 Quasi-1D-Based Polymeric Composites: Preparation and Characterization

In the previous chapter, we described the liquid phase exfoliation of $TaSe_3$ and the synthesis of polymeric composites with threads of quasi-1D $TaSe_3$ fillers. Figure **2-1** shows a summary of the procedure with the additional characterization of the exfoliated fillers and prepared composites. The $TaSe_3$ crystals were subjected to solvent-assisted exfoliation separately in two different solvents of acetone and dimethylformamide (DMF). During this process, the bulk $TaSe_3$ was dispersed and exfoliated in the solvents using low-power ultrasonic bath sonication. The dispersion was centrifuged to isolate the solids, and the procedure of sonication/centrifugation was repeated several times. A photograph of the resultant dispersion is shown in Figure **2-1** (d). The SEM image in Figure **2-1** (e) shows the size and morphology of $TaSe_3$ nanowires post-exfoliation. The typical diameter of the exfoliated bundles of the atomic threads of $TaSe_3$ ranges from 50 nm to 100 nm, while their length is in the range of several hundred micrometers. The fillers were mixed with UV-polymer, epoxy, and SA. The obtained flexible thin films and composites are shown in Figure **2-1** (f-h).

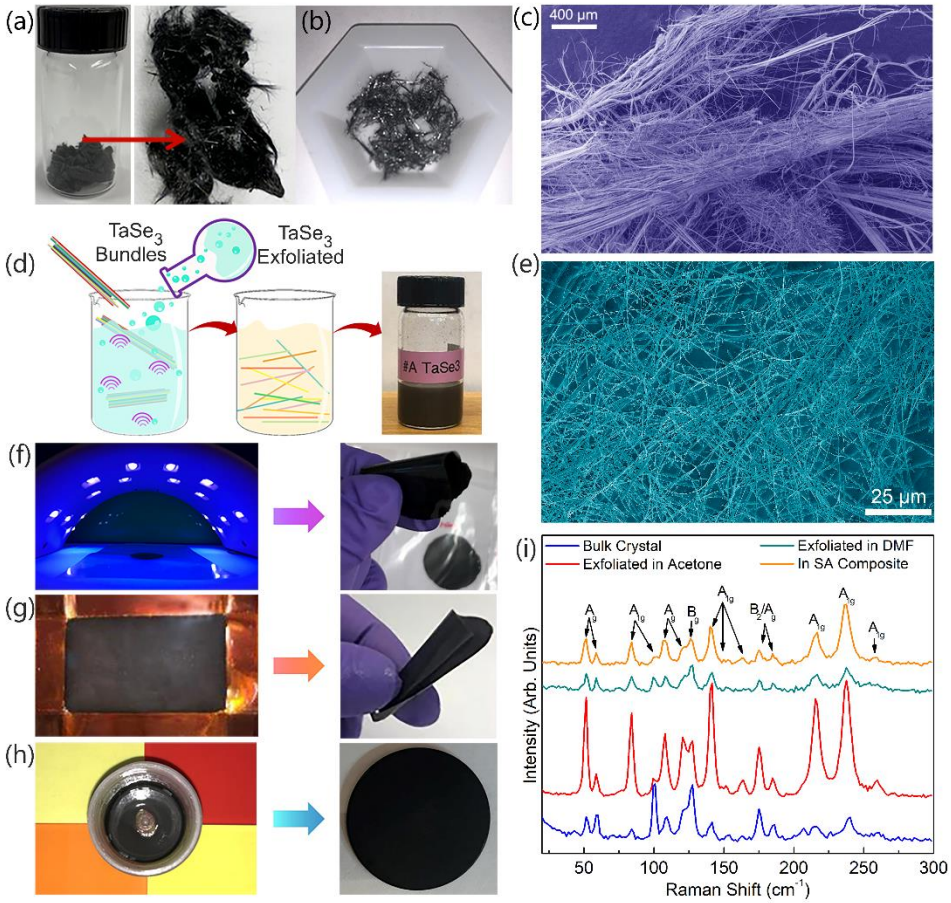

Figure 2-1: Composite film preparation and characterization. (a, b) As-prepared $TaSe_3$ crystals and fibers. (c) SEM image of fibrous $TaSe_3$ bundles. (d) Schematic showing the process of chemical liquid-phase exfoliation using low-power bath sonication. The vial contains exfoliated $TaSe_3$ in acetone. (e) SEM image of $TaSe_3$ threads after liquid-phase exfoliation in acetone. Note the high aspect ratio morphologies. (f, g) Synthesis of flexible polymeric films using a special UV-cured polymer (f) and sodium alginate (g) as the matrix and exfoliated $TaSe_3$ as filler. (h) Optical image of the 1 mm thick epoxy composite containing about 1.3 vol % concentration of exfoliated $TaSe_3$ threads. (i) Raman spectra of the $TaSe_3$ before (blue) and after solvent-assisted exfoliation in acetone (red) and DMF (cyan). The orange curve shows the Raman spectrum of the $TaSe_3$ filler mixed with sodium alginate (SA). The characteristic Raman peaks of $TaSe_3$ do not change as it is exfoliated or combined with SA polymer. Reprinted with permission from Barani et al., Advanced Materials. 33 (2021) 2007286, Copyright © 2021, Wiley - VCH VERLAG GMBH & CO. KGAA.

2.1.1 Raman Characterization

Raman spectra of $TaSe_3$ were taken before and after exfoliation in different solvents and after mixing with the polymer matrix to confirm the quality and stability of the quasi-1D $TaSe_3$ fillers. The results are shown in Figure **2-1** (i). The measurements were performed in the backscattering configuration under $\lambda = 488$ nm laser excitation using low power to prevent local heating. The spectrum displays characteristic peaks between $25\ cm^{-1}$ to $300\ cm^{-1}$, which originate from the primitive monoclinic structure of $TaSe_3$ [36,37]. The peaks at $140\ cm^{-1}$, $164\ cm^{-1}$, $214\ cm^{-1}$ and $238\ cm^{-1}$ are assigned to the out-of-plane A_{1g} phonon modes, whereas the peaks at $176\ cm^{-1}$ and $185\ cm^{-1}$ to the B_2/A_g modes [37]. The Raman data confirm the crystalline nature of the $TaSe_3$ filler and the preservation of its structural integrity after all processing steps.

2.1.2 Mass Density Measurements

Using an electronic scale (Mettler Toledo), the weight of the samples was measured in air (w_a) and in DI water (w_w). In the case of SA flexible films, the weights of the films were measured in air and ethanol (w_e) since SA is soluble in DI water. The mass density of the samples was calculated according to Archimedes' principle $\rho_c = (w_a/(w_a - w_{w,e})) \times (\rho_{w,e} - \rho_a) + \rho_a$ where ρ is the density and subscripts "a", "w", and "e" corresponds to air, water, and ethanol, respectively. The volume fraction, ϕ, of the $TaSe_3$ filler was

calculated according to the rule of mixtures as $\phi = (\rho_c - \rho_p)/(\rho_f - \rho_p)$ where ρ_p and ρ_f are the density of the base polymer and $TaSe_3$ filler, respectively

2.2 EMI Shielding Performance of Quasi-1D composites

2.2.1 EMI Measurements in X-Band

To determine EMI characteristics, we measured the scattering parameters, S_{ij}, using a two-port programmable network analyzer (PNA) Keysight N5221A. The indices i and j represent the ports which are receiving and emitting the EM waves. The PNA was calibrated for 2-port measurements of scattering parameters S_{ij} at input power $P_{in} =$ 3 dBm. A WR-90 commercial grade straight waveguide with two adapters at both ends with SMA coaxial ports was used as a sample holder. Special cables were used for high-temperature RF measurements. The samples were a bit larger than the rectangular cross-section (22.8×10.1 mm^2) of the central hollow part of the waveguide in order to prevent the leakage of EM waves from the sender to the receiver antenna. A photo of the actual system is shown in Figure **2-2**.

In PNA, each port can simultaneously emit and detect the EM waves, and thus, the results of the measurements include four parameters of S_{11}, S_{12}, S_{21}, and S_{22}. Owing to the symmetry of the samples, one can expect that $|S_{11}| = |S_{22}|$ and $|S_{12}| = |S_{21}|$. The

measurements were performed in the X-Band frequency range (8.2 – 12.4 GHz) with a frequency resolution of 3 MHz.

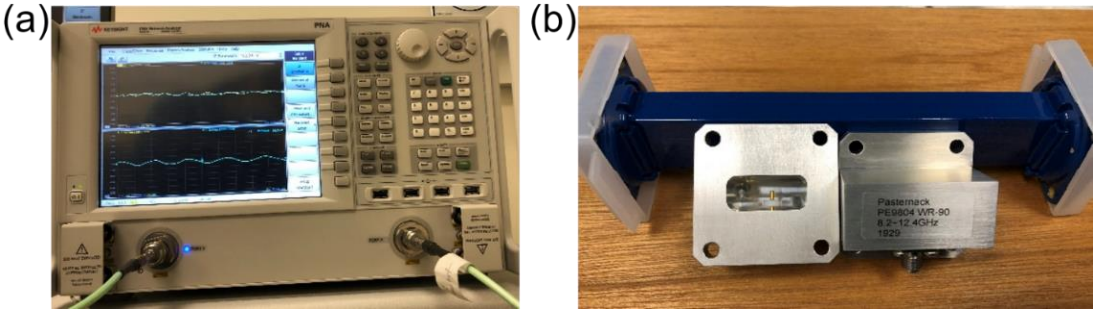

Figure 2-2: Experimental setup used for electromagnetic shielding interference characterization of flexible films with quasi-one-dimensional vdW fillers. Reprinted with permission from Barani et al., Advanced Materials. 33 (2021) 2007286, Copyright © 2021, Wiley - VCH VERLAG GMBH & CO. KGAA.

To determine EMI characteristics, we measured the scattering parameters, S_{ij} The scattering parameters define the EM coefficients of reflection, $R = |S_{11}|^2$, and transmission, $T = |S_{21}|^2$, which, in turn, allows one to calculate the coefficient of absorption, A, as $A = 1 - R - T$. A fraction of the energy of the EM wave, incident on the film, is reflected at the interface. The rest is absorbed inside the film or transmitted through it. Because part of EM energy is reflected from the interface, the coefficient of absorption, defined as the power percentile of the absorbed EM way in the medium to the total power of the incident wave, is not truly indicative of the material's ability to absorb the EM waves. For this reason, the effective absorption coefficient, A_{eff}, is defined as $A_{eff} = (1 - R - T)/(1 - R)$. The total shielding efficiency, SE_T, describes the total attenuation of the incident EM wave by the material of interest. This parameter determines the

material's ability to block the EM waves and consists of two terms – the reflection shielding efficiency, SE_R, and the absorption shielding efficiency, SE_A. It should be noted that as the EM wave passes through the composite medium, it experiences internal reflections, which adds to the shielding by absorption. These parameters can be calculated in terms of R, T, and A_{eff} as follows:

$$SE_R = 10\log[(P_i/(P_i - P_r)] = -10\log(1 - R), \quad (1)$$

$$SE_A = 10\log\left[\frac{P_i - P_r}{P_i - P_r - P_a}\right] = 10\log\left[\frac{1-R}{1-R-A}\right] = -10\log\left[\frac{1-R-A}{1-R}\right] = -10\log\left(1 - \frac{A}{1-R}\right) = -10\log(1 - A_{eff}), \quad (2)$$

$$SE_T = 10\log\left(\frac{P_i}{P_t}\right) = SE_R + SE_A = -S_{21}. \quad (3)$$

2.2.2 Measurements in EHF-Band

Due to a small cross-section of the WR-3 waveguide, EMI characteristics in the sub-THz range were measured in free space. One of the most commonly used free-space techniques at THz and sub-THz frequencies is time-domain spectroscopy (THz-TDS) [40]. Its efficiency is limited to frequencies below 300 GHz due to the low power of the excitation signal in this spectral range [41]. Characterization of highly absorptive materials using THz-TDS may not be feasible. For this reason, the EMI shielding efficiency was determined from the measured scattering parameters using an Agilent N5245A vector

network analyzer (VNA) with a pair of frequency extenders from Virginia Diodes Inc [33,42]. The quasi-optical path of the measurement setup consisted of two high-gain horn antennas and two double convex lenses to focus the EM wave on the sample under test. The measurements were performed in the frequency range from 220 GHz to 320 GHz. The VNA with frequency extenders was calibrated using the Thru – Reflect–Line (TRL) method. The reference planes for 2-port measurements were achieved at the ends of the waveguide ports of both extenders. To compensate for the transmission losses in the measurement path, two additional reference measurements were performed. The measurement with an empty optical path and the measurement with a metal plate allows one to calculate the actual transmission and reflection coefficients, respectively. In order to improve the reliability of the collected data, additional time-domain gating was applied (see [42–44] for more details).

2.3 Results and Discussion

2.3.1 EMI Effectiveness in The X-Band

The reflection, transmission, and absorption coefficients of the samples were calculated from the scattering parameters and are shown in Figure **2-3**. The reflection, absorption, and total EMI shielding efficiencies of the UV-cured flexible polymer films with low concentrations of $TaSe_3$ fillers are presented in Figure **2-4** (a-c). As one can see, a thin film with 130 µm thickness and an extremely low concentration of 1.14 vol% of quasi-1D

$TaSe_3$ fillers reveals strong EMI shielding of ~10 dB, *i.e.*, 90% of the incident EM power on the film is shielded via reflection at the air-composite interface or absorption as it passes through the composite. Typically, the EMI shielding efficiency increases with the increasing filler loading.

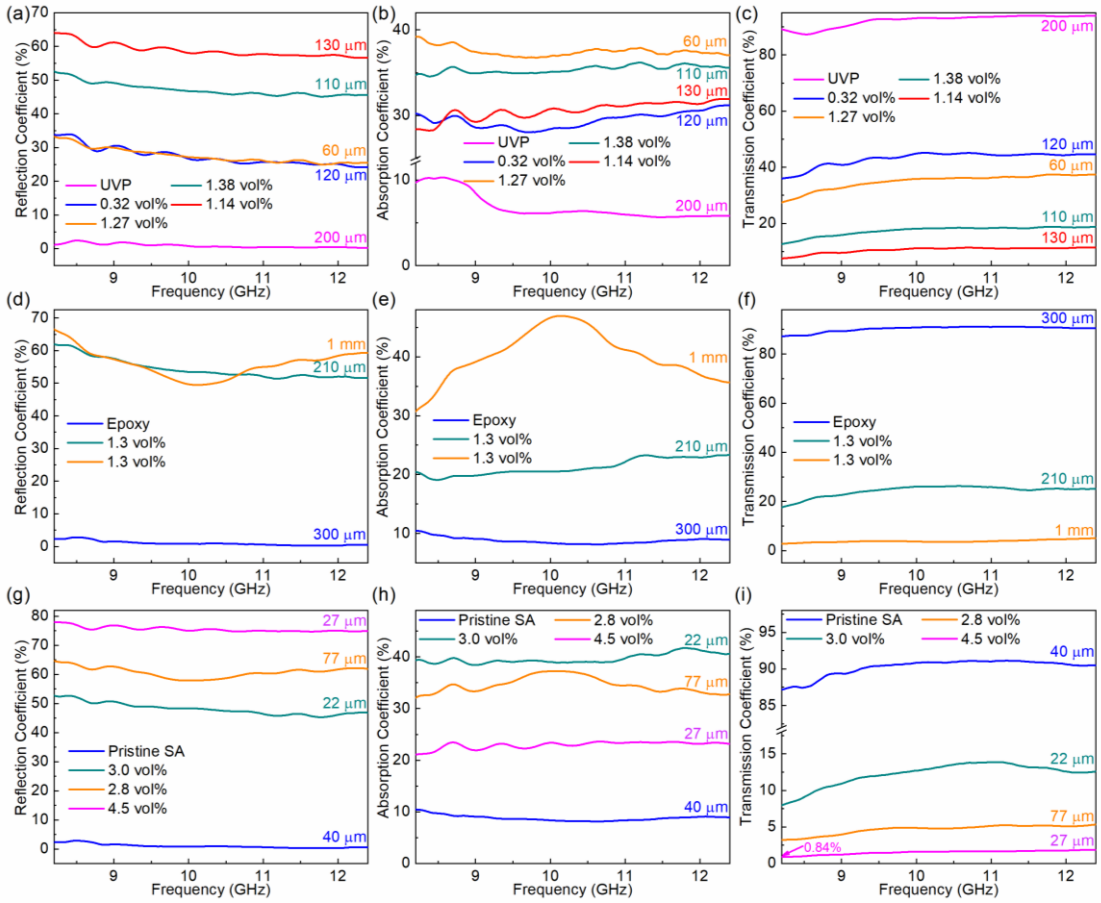

Figure 2-3: Reflection, absorption, and transmission coefficients of films and composites with a low concentration of quasi-1D fillers in the X-band frequency range. Reprinted with permission from Barani et al., Advanced Materials. 33 (2021) 2007286, Copyright © 2021, Wiley - VCH VERLAG GMBH & CO. KGAA.

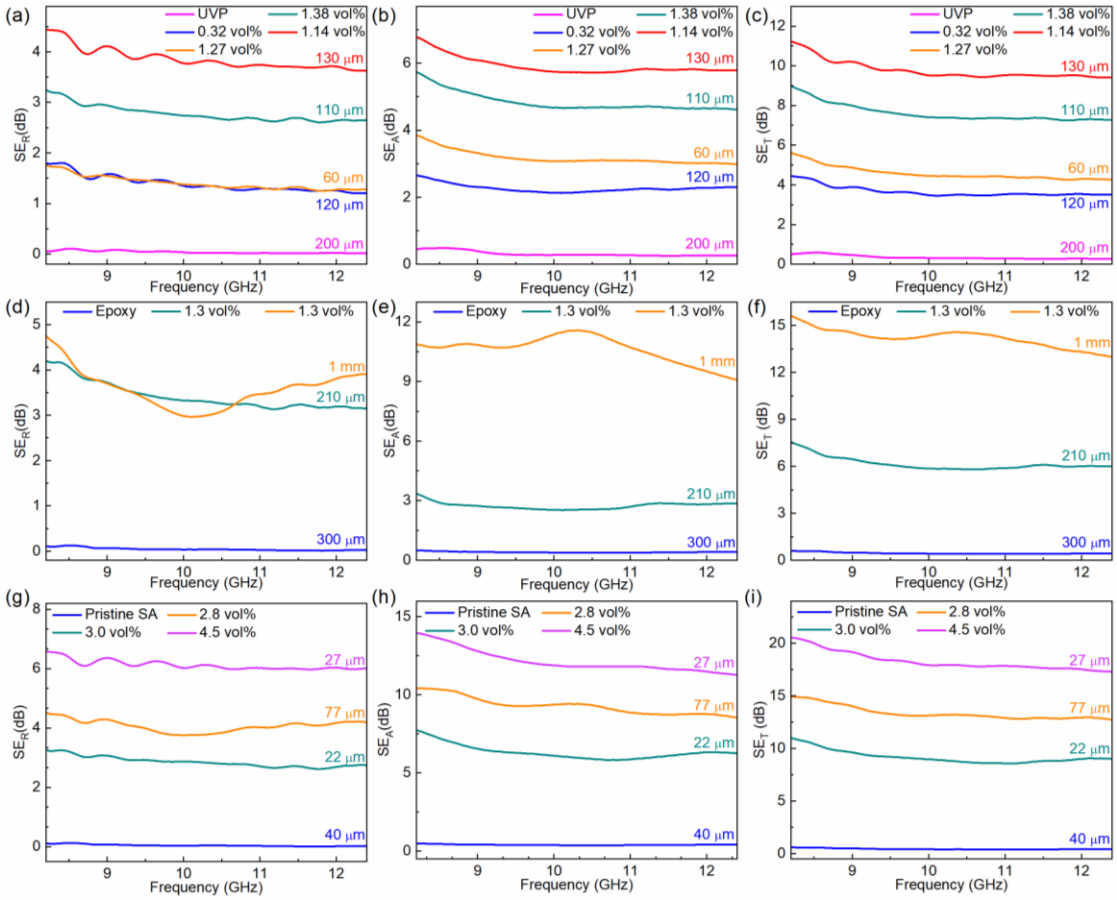

Figure 2-4: Electromagnetic characteristics of films and composites with low concentrations of quasi-1D $TaSe_3$ fillers in X-band frequency range. Reflection (SE_R), absorption (SE_A), and total (SE_T) electromagnetic interference shielding efficiency of (a-c) UV-cured polymer (d-f) epoxy, and (g-i) sodium alginate films and composites with a low concentration of quasi-1D $TaSe_3$ bundles of atomic threads as fillers. The concentration is indicated in the legends. Reprinted with permission from Barani et al., Advanced Materials. 33 (2021) 2007286, Copyright © 2021, Wiley - VCH VERLAG GMBH & CO. KGAA.

One can see from Figure **2-4** (i) that ~20 dB of total EMI shielding at $f = 8.2$ GHz can be achieved in $27 -$ μm thick SA-based films with only 4.5 vol % of quasi-1D van der Waals fillers. The shielding due to the absorption of EM waves is approximately twice as much as that due to the reflection of the waves. The total EMI shielding efficiency, SE_T, which indicates how much EM energy is blocked by a film of a particular thickness, is not the

only characteristic that has to be considered for practical purposes. Another commonly used metric is the efficiency normalized by the mass density, $SSE = SE_T/\rho$. However, SSE does not fully describe the EMI shielding of a given material because, by increasing the thickness of a film at a constant mass density, one can achieve higher and higher SSE values. To better describe the EMI shielding at the material level, one can normalize SSE by the thickness, t, and use SSE/t to compare the effectiveness of different composites [23,45]. Here, we argue that, for many practical purposes, it is meaningful to normalize $SSE/t = SE_T/(\rho \times t)$ by the loading fraction of the fillers. Achieving higher EMI shielding in the composite with the lowest loading of the fillers makes sense from the weight and cost considerations as well as for maintaining electrical insulation of the composite when required. Indeed, if one composite can deliver the required SE with a low loading of lightweight fillers while another needs 90 % loading of silver (Ag) particles, it is clear that the Ag composite likely will be heavy, expensive, and electrically conductive.

To assess the performance of the polymeric composites with fillers, we define the figure-of-merit $Z_B = SE_T/(\rho \times t \times m_f)$ by introducing normalization by the mass fraction of the fillers $m_f = M_F/(M_B + M_F)$, where M_F and M_B are the masses of the filler and the base polymer, respectively. Here, we summarize the parameters for evaluating the EMI effectiveness of the composites and the physical interpretation of the Z_B figure-of-merit:

$$SEM = SE/m_f, \quad (4)$$

$$SSE = SE/\rho, \tag{5}$$

$$SSE = SE/\rho = SE \times V/(M_B + M_F), \tag{6}$$

in which, V, M_B, and M_F are the volume and total mass of the base polymer and mass of filler in the composite. If we normalize SSE by thickness:

$$SSE/t = SE \times V/[t(M_B + M_F)] = SE \times A/(M_B + M_F). \tag{7}$$

Here, A is the surface area of the composite. The Z_B-factor is the normalization of the SSE/t with respect to the filler mass loading fraction ($m_f = M_f/(M_B + M_f)$) as follow:

$$Z_B = \frac{SSE}{t \times m_f} = [SE \times A/(M_B + M_F)][\ (M_B + M_F)/M_F] = \ SE \times (\frac{A}{M_F}). \tag{8}$$

It is interesting to note that the physical meaning of the Z_B figure-of-merit is the total shielding efficiency of the films per the areal density of the fillers, *i.e.*, $Z_B = SE_T/(M_F/A)$, here $A = V/t$ is the area of the sample of the volume V and thickness t. The defined metric puts more emphasis on the material performance, and specifically the filler performance. **Figure 2-5** (a,b) show the SSE/t and Z_B for several polymer composites with different fillers. One can see that our composites with quasi-1D van der Waals fillers outperform composites with carbon nanotubes and graphene. Although a composite with Ag has better performance in terms of SSE/t, the composites with quasi-1D fillers exhibit superior Z_B

efficiency. The latter means that the polymer composites with a low areal density of quasi-1D fillers are extremely effective in blocking EM waves.

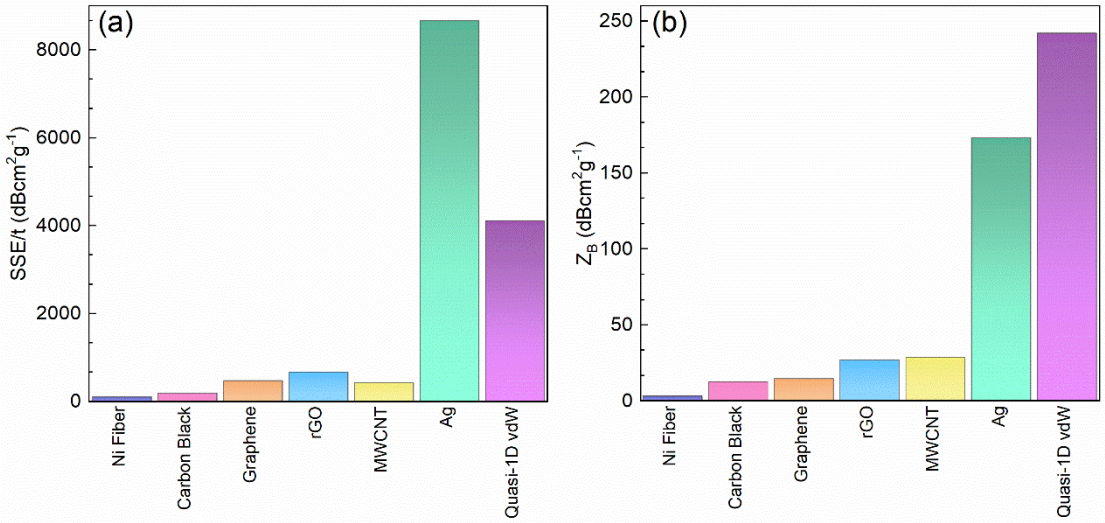

Figure 2-5: EMI shielding characteristics of polymeric composites with different fillers. (a) The specific EMI shielding efficiency normalized by thickness. A polymer composite with 90 wt% of Ag inclusion exhibit the highest SSE/t. (b) The same plot in panel (a) normalized by the filler weight loading fraction. The Z_B factor indicates composite's shielding effectiveness per aerial density of the filler. The lower the thickness, density, and filler weight loading fraction and the higher the total shielding effectiveness, the higher the Z_B. The data for other composites are from: Ni fiber [46], carbon black [47], graphene [32], rGO [48], MWCNT [47], and Ag [49]. Reprinted with permission from Barani et al., Advanced Materials. 33 (2021) 2007286, Copyright © 2021, Wiley - VCH VERLAG GMBH & CO. KGAA.

A summary of the shielding efficiency of several composites with different fillers is listed in **Table 2-1**. In this table, ϕ_f, m_f, t, and ρ are the filler volume fraction, filler mass fraction, thickness, and density of the composite.

Table 2-1: Comparison of different composites used for electromagnetic shielding

Polymer/ Filler	ϕ_f (%)	m_f (%)	t (cm)	ρ (gcm^{-3})	SE (dB)	SEM (dB)	SSE ($dBcm^3g^{-1}$)	SSE/t ($dBcm^2g^{-1}$)	Z_B	Ref.
UVP/$TaSe_3$	1.14	6.43	0.013	1.31	11.00	1.71	8.40	645	100.44	This work
UVP/$TaSe_3$	1.38	7.70	0.011	1.33	9.00	1.17	6.79	617	80.23	
UVP/$TaSe_3$	1.27	7.12	0.006	1.32	5.50	0.77	4.17	695	97.67	
SA/$TaSe_3$	3.00	12.32	0.0022	1.80	10.30	0.84	5.72	2601	211.18	
SA/$TaSe_3$	3.00	12.3	0.0077	1.80	15.00	1.22	8.33	1082	87.87	
SA/$TaSe_3$	4.5	17	0.0027	1.89	21	1.24	11.1	4115	242	
Epoxy/Graphene	19.5	32.00	0.1000	1.375	65.00	2.03	47.27	472	14.77	[32]
PC/MWCNT	/	20.0	0.21	/	39.00	1.95	34.50	164	8.21	[50]
ABS/MWCNT	/	15.0	0.11	/	50.00	3.33	47.60	432	28.85	[47]
PS/MWCNT	/	20.0	0.20	/	30.00	1.50	57.00	285	14.25	[51]
ABS/CB	/	15.0	0.11	/	20.00	1.33	20.90	190	12.67	[47]
EPDM/CB	/	37.5	0.20	/	18.00	0.48	30.30	151	4.04	[52]
PS/rGO	3.47	7	0.2500	1.084	45	6.42	41.51	166	23.72	[31]
Phenolic resin/rGO	/	70	0.0300	1.67	43.4	0.62	25.99	866	12.38	[53]
PEDOT/rGO	/	25	0.0800	1.3	70	2.8	53.85	673	26.92	[48]
Cellulose/Ag	/	50.00	0.0045	2.62	101	2.02	38.55	8662	173.26	[49]
PES/Ni fiber	7	32	0.2850	1.87	58	1.81	31.02	108	3.40	[46]

2.3.2 EMI effectiveness in the EHF-band

As the next step, we examined the EMI shielding effectiveness of the composites with the low loading of quasi-1D $TaSe_3$ fillers in the EHF band. The measurements were performed using the quasi-optical free space method. The coefficients of reflection, absorption, effective absorption, and transmission presented in **Figure 2-6** (a) – (d) demonstrate the superior performance of the flexible films with quasi-1D fillers in the EHF band. Note that only 0.0002% of the incident EM wave is transmitted through the 1-mm-thick film with only 1.3 vol% of quasi-1D $TaSe_3$ fillers. **Figure 2-6** (b,c) indicates clearly that absorption

is the dominant mechanism of the EMI shielding in the EHF range. This is different from the situation in the X-band, where the reflection was substantial. The absorption SE_A increases from 55 dB to 76 dB as the frequency varies from 220 GHz to 320 GHz. The EMI shielding by reflection contributes only ~ 1.5 dB to the total shielding, and it slightly decreases from 1.7 dB to 1.4 dB as the frequency increases. For comparison, the inset shows pristine epoxy's characteristics in the same frequency range. As expected, epoxy by itself is a poor shielding material and provides only the mean value of $\mathrm{SE_T} \sim 1.5$ dB in the EHF range. The EMI shielding performance of quasi-1D fillers in insulating epoxy films is exceptional as compared to other fillers.

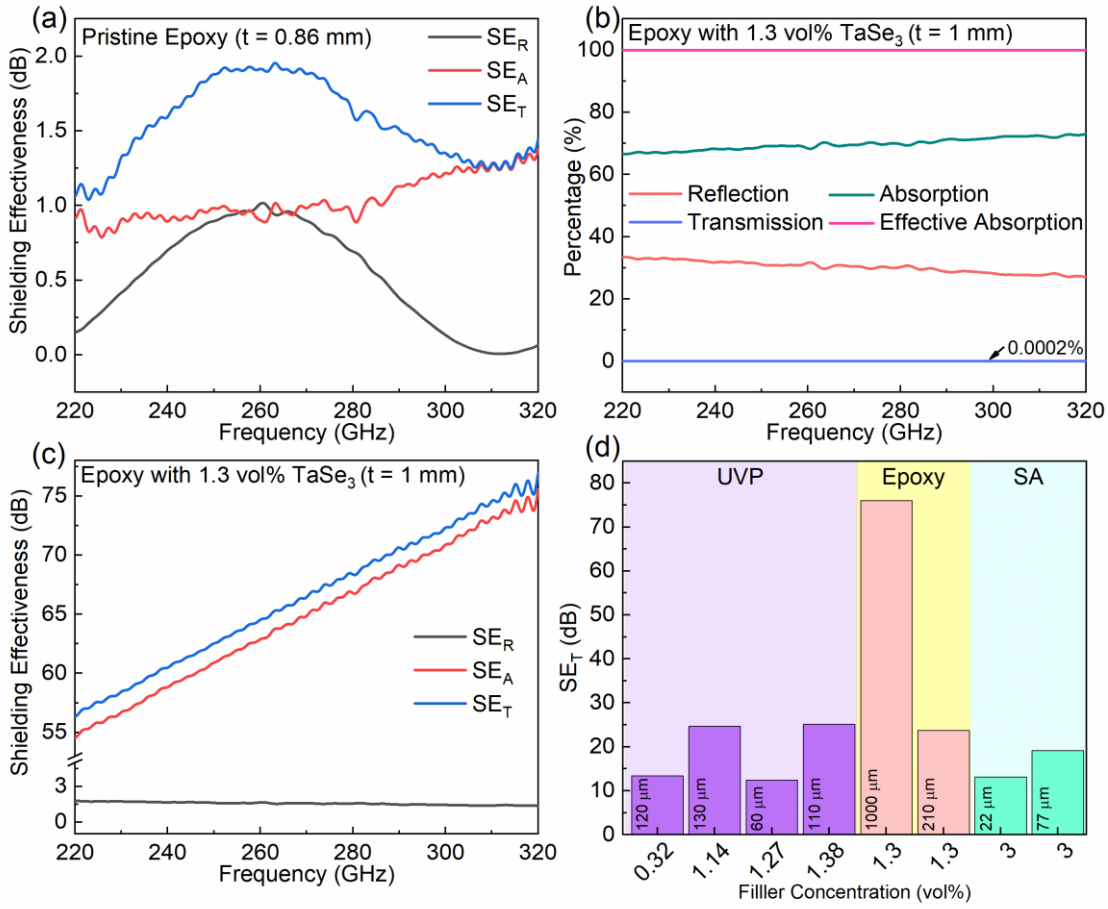

Figure 2-6: Electromagnetic shielding characteristics of the films with low concentration of quasi-1D $TaSe_3$ fillers in EHF band. (a) Shielding effectiveness of pristine epoxy used as the base material for some of the composites. (b) Reflection, absorption, effective absorption, and transmission coefficients of epoxy with 1.3 vol% loading of the quasi-1D $TaSe_3$ fillers. Note that in the EHF range, almost all the incident EM wave energy is blocked and only 0.0002% is transmitted. (c) Reflection, absorption, and total shielding effectiveness of the same composite. Note that absorption is the dominant mechanism in blocking the EM waves in EHF band. (d) Total shielding effectiveness of all samples tested in the EHF band. The results are shown for the frequency 320 GHz. The total shielding effectiveness scales with the loading fraction of quasi-1D fillers and the thickness of the films. Reprinted with permission from Barani et al., Advanced Materials. 33 (2021) 2007286, Copyright © 2021, Wiley - VCH VERLAG GMBH & CO. KGAA.

An important feature of the synthesized films is their electrical insulation. We verified that the DC electrical conductivity of the films is below the instrumentation measurement limit.

The upper bound of the electrical resistivity is 10^{15} Ω-cm. This means that the loading fraction of the quasi-1D van der Waals fillers is below the percolation threshold. This is rather surprising because, according to the conventional theories developed for carbon nanotubes and other materials with high aspect ratio, the electrical percolation should be attained at an even lower loading < 1 vol% [54–58]. The disagreement with the known models can be explained by the fact that the conventional theories used the mathematical approximation of the fillers as straight cylinders, whereas we often observed $TaSe_3$ bending (see Figure 2), which could affect the percolation threshold. During material processing, we paid special attention to the uniformity of the filler dispersion and verified it with microscopy. Some deviation from the uniformity over the total sample area is a possible factor that requires a separate investigation.

Another interesting question is why electrically insulating films are so effective in blocking the EM waves. Even though the quasi-1D fillers do not create a percolated, electrically conductive network, they effectively couple with EM waves. The electric field of EM waves interacts with the free carriers in the quasi-1D conductors and thus enables reflection and absorption of EM energy. One should also note that at the frequency of 10 GHz, the EM wavelength $\lambda = c/(\varepsilon_r^{1/2}\, f) \sim 19$ mm (here $\varepsilon_r \sim 2.4$ is the relative dielectric constant of polymer base material). A few connecting quasi-1D fillers with a high aspect ratio would make something similar to an antenna, effective at receiving and re-emitting EM energy. A few connecting and bent quasi-1D fillers that form a circular loop would act similarly to a magnetic antenna in this frequency range. These considerations can explain the efficiency

of quasi-1D bundles of atomic threads as fillers in EMI shielding films. The "antenna" action in the X-band is consistent with the fact that the reflection of EM waves made a substantial contribution to the overall EMI shielding at these frequencies. In the EHF range, where the EM wavelength at $f = 300$ GHz is $\lambda \sim 0.65$ mm, the randomly distributed quasi-1D fillers can act more as the scattering objects, which explains the dominance of absorption in the overall EMI shielding.

One should note that the electrical conduction properties of $TaSe_3$ itself are still not completely understood. Bulk $TaSe_3$ has not been studied in as much detail as other TMT materials, possibly due to its low superconducting phase transition T_c ~2 K [18,59]. A variety of measurements indicate that $TaSe_3$ is metallic or semi-metallic down to T_c [60–63]. At the same time, some reports suggested that stress or strain can produce a semiconducting gap [37,64]. Moreover, many published studies on $TaSe_3$ do not include detailed compositional data (e.g., EDS, EPMA, ICP-MS/OES). At least some CVT-grown $TaSe_3$ crystals appear selenium deficient [21,65], approximately $TaSe_{2.8}$, like the ones used in this work. Surprisingly, selenium-deficient $TaSe_3$ can be produced even in selenium-rich CVT conditions [36,66,67]. Stoichiometric $TaSe_3$ has been isolated from high-pressure conditions and selenium-flux growth [35,68]. Although selenium deficiency does not seem to affect the overall electrical conductivity of $TaSe_3$ or its T_c [18,39,61–63], several studies indicate that doping can modify its electronic structure. For example, the mixed chalcogenide $Ta(S_xSe_{1-x})_3$ becomes semiconducting with increasing sulfur content [69], and indium impurities from contacts to $TaSe_3$ can produce a metal-insulator transition

[70,71]. In addition, the intercalation of copper into $TaSe_3$ causes T_c lowering and weak induced CDWs [72]. Further investigations clearly are needed to understand the impact of defects and dopants on the electrical properties of $TaSe_3$.

2.4 Summary and Conclusions

In conclusion, we demonstrated that quasi-1D van der Waals materials could be used as fillers in flexible polymer films providing excellent EMI shielding capability in the X-band and EHF-band. Polymer composites films (27 μm thickness) with only 4.5 vol% of quasi-1D $TaSe_3$ exfoliated atomic thread fillers delivered ~20 dB of total EMI shielding in the practically important X-band GHz frequency range. The EMI shielding efficiency of the developed materials is expressed via the total shielding efficiency normalized by the mass density, thickness, and filler loading fraction, Z_B~242 dB/cm^{2}g, exceeds that of other polymers with various metallic, carbon nanotubes, or graphene fillers. The EMI shielding performance of the films with the quasi-1D fillers in the EHF-band of sub-THz frequencies was particularly impressive. Total shielding efficiency SE_T changed from 60 dB to above 70 dB as the frequency varied from 240 GHz to 320 GHz. This performance was achieved in composite films with only 1.3 vol% loading of exfoliated quasi-1D fillers of $TaSe_3$ and the film thickness of 1 mm. Interestingly, efficient EMI shielding was achieved in polymer films, which retained their DC electrically insulating properties, essential for many applications. The developed polymer films with quasi-1D fillers are promising for 5G-and-

beyond communication technologies, which require electromagnetic shielding films, which are flexible, lightweight, corrosion resistive, electrically insulating, and inexpensive.

Chapter 3 Quasi-1D-Based Electromagnetic-Polarization Selective Polymeric Composites

3.1 Introduction

Commonly, one selects functional materials with known characteristics to build a device or a system. In more elaborate approaches, one can engineer and synthesize materials with the required properties for specific applications. The inspiration for material selection, composition, and assembly can come from diverse sources. In one well-known approach – biomimetics – the models and elements of nature are applied to the design of synthetic systems [73,74]. In an analogous approach, well-developed design solutions for macroscopic objects are translated into micro-, nano-, or atomic-scale structures. We followed this innovative path to create a polymer composite with polarization-sensitive electromagnetic interference (EMI) shielding characteristics by emulating the macroscopic structure and, to some degree, the functionality of an electromagnetic (EM) grid aperture antenna at the nanoscale level. A polarization-selective grid antenna is a set of parallel metal grid lines that allow transmission or reflection of radio-frequency (RF) radiation depending on the polarization of the radiation [75]. This design allows a single structure to act as a mirror for RF radiation or become transparent to such radiation. When the polarization of the electric field is parallel to the grid lines, the electric field induces a

current in the grid lines, which reflects the EM wave. In the alternate case, with the polarization of the electric field perpendicular to the grid lines, no current is induced, and the EM radiation passes through the grid. Polarization selection grids are often manufactured with metal wire tracks, usually copper, on a dielectric substrate. The spacings between grid lines must be small relative to the wavelength of the linear polarized EM waves. Here we use a similar antenna design, albeit at the nanometer scale, to create a "grid-antenna film."

In this chapter, we mimic the grid antenna design in nano-composites by employing chemically-exfoliated *bundles* of a quasi-one-dimensional (1D) van der Waals material, tantalum triselenide ($TaSe_3$). We recently demonstrated the potential of $TaSe_3$ for extremely high current density [12,14,38] and effective EMI shielding, even with random filler distribution and low filler loading fractions [1]. Such quasi-1D van der Waals materials are less well-investigated compared with two-dimensional (2D) layered van der Waals materials, such as graphene and transition metal dichalcogenides (TMDs) [6–8]. The quasi-1D van der Waals materials include the transition metal trichalcogenides (TMTs) with formula MX_3 (M = transition metal, X = S, Se, Te), such as TiS_3, NbS_3, $TaSe_3$, and $ZrTe_3$, as well as other materials containing 1D structural motifs [76–78]. As opposed to TMDs, TMTs exfoliate into nanowire- or nanoribbon-type structures [12,15,17,77,78], which stem from their unique chain-based crystal structures, illustrated for $TaSe_3$ in **Figure 3-1**a. In principle, these low-dimensional materials can be exfoliated into individual atomic chains or few-chain atomic threads. Theory suggests that there are many quasi-1D van der

Waals materials that retain their metallic or semiconductor properties when exfoliated to atomic chains [16,79,80]. The exfoliated bundles of $TaSe_3$ atomic threads with cross-sections in the range of 10 nm × 10 nm to 100 nm × 100 nm revealed exceptionally high current densities of up to ~ 30 MA/cm^2, an order of magnitude higher than that of copper [81,82]. Additionally, the liquid phase exfoliated (LPE) $TaSe_3$ bundles can be millimeters in length, providing substantial aspect ratios. The unique current-carrying capability of the metallic $TaSe_3$, in addition to their high-aspect-ratios, allows us to use them as "metallic grids" even when scaled down to 100-nm features or below. The quasi-1D van der Waals metallic fillers can be mass-produced at low cost via liquid phase exfoliation. This adds a significant extra benefit to such materials as compared to carbon nanotubes.

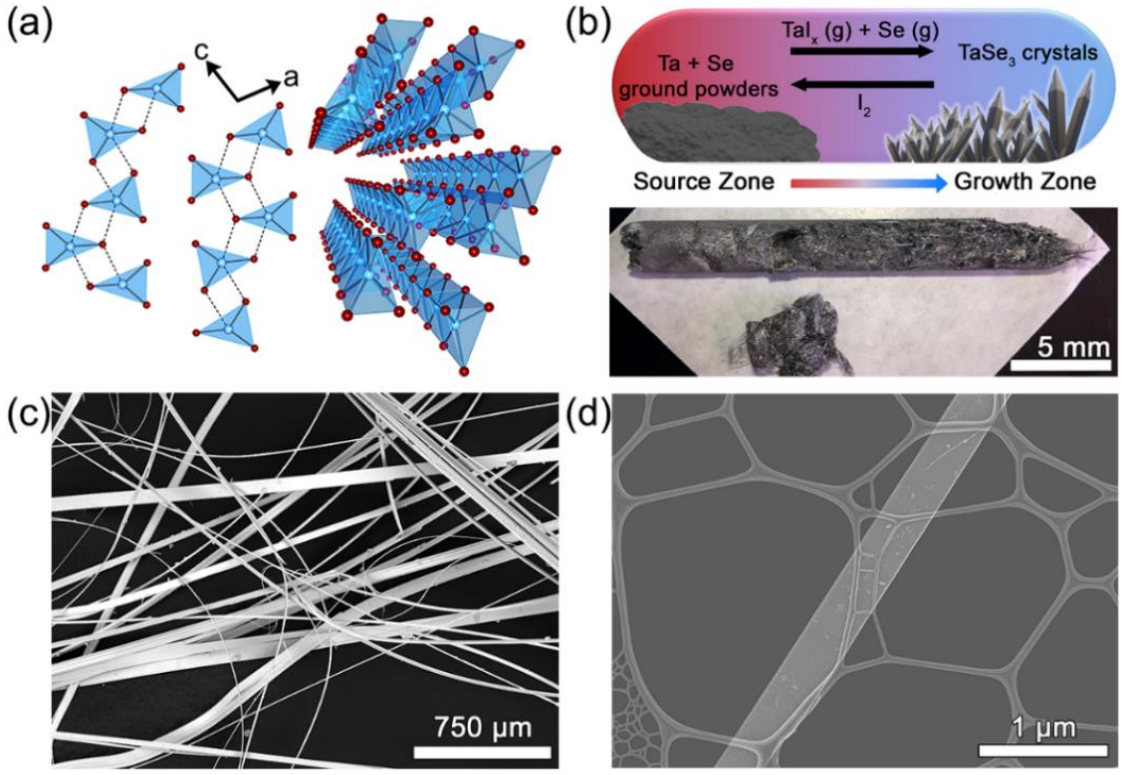

Figure 3-1: Crystal structure of quasi-1D $TaSe_3$ used in this study. (a) Crystal structure of $TaSe_3$ (blue = Ta, red = Se) with two views illustrating interchain interactions and emphasizing this material's 1D nature originating from chains extending along the b-axis. (b) Schematic of the CVT process employed here to prepare $TaSe_3$ crystals (top) and a photograph of an as-synthesized mass of crystals removed from its growth ampule (below). (c) SEM image of $TaSe_3$ crystals highlighting their high aspect ratio. (d) Secondary electron (SE) image of a $TaSe_3$ nanowire produced by solvent exfoliation. Reprinted with permission from Barani et al., ACS Applied Materials & Interfaces. 13 (2021) 21527–21533. Copyright © 2021 American Chemical Society.

3.2 Experimental Section

3.2.1 Materials

For this study, we used $TaSe_3$ crystals prepared by chemical vapor transport (CVT). In contrast to typical CVT reactions, where the goal is the growth of a relatively small number of larger crystals [1,12,17,38], here we varied reaction conditions to yield 0.7-1.5 g batches of $TaSe_3$ crystals for composite preparation. Transport was achieved using iodine as the transport agent and/or by using a 625 °C – 600 °C temperature gradient. As can be seen in **Figure 3-1**b, the scale of these reactions led to the growth of $TaSe_3$ crystals, almost entirely filling the ampule volume. The resulting mat of crystals could be removed easily, providing 18 % - 38 % yields of mm- to cm-long needlelike or fibrous crystals (**Figure 3-1**b) and also leaving behind a quantity of microcrystalline solid that was not used for subsequent exfoliation. We used three batches of $TaSe_3$ crystals with slightly different growth conditions as follows:

Powder: Tantalum (99.98%) and selenium (99.99%) powders were purchased from STREM. Iodine (99.9%) was obtained from J.T. Baker.

Preparation of $TaSe_3$ (Batch 1): A stoichiometric mixture of 1.7310 g (9.57 mmol) tantalum and 2.2710 g (28.8 mmol) selenium was ground gently using an agate mortar and pestle. The ground mixture was transferred to a quartz glass ampule (10 mm ID, 14 mm

OD, 170 mm length) containing 80.5 mg I_2 (5.4 mg cm^{-3} for the ~15 cm^3 volume ampule). The ampule was evacuated and backfilled with Ar three times while submerged in a CH_3CN/CO_2(s) bath before being vacuum sealed (10^{-2} Torr). The ampule was placed in a two-zone furnace and heated at 3.5 °C min^{-1} to 620 °C. After 12 d, the reaction was cooled to 420 °C and held at that temperature for 12 h, then cooled to 220 °C and held at that temperature for 12 h, then cooled to 120 °C and held at that temperature for 12 h, and finally cooled to room temperature. The resulting grey-black, needle-like crystals were removed from the ampule and aired in a fume hood to allow residual I_2 to sublime. 0.719 g of $TaSe_3$ crystals were isolated (~18% yield).

Preparation of $TaSe_3$ (Batch 2): 1.7302 g (9.56 mmol) tantalum and 2.2716 g (28.8 mmol) selenium were ground gently together using an agate mortar and pestle before being transferred to a quartz glass ampule (10 mm ID, 14 mm OD, 170 mm length) with 62.4 mg I_2 (4.2 mg cm^{-3} for this ~15 cm^3 volume). The ampoule was evacuated and backfilled with Ar three times while submerged in a CH_3CN/CO_2(s) bath and subsequently sealed under vacuum (10^{-2} Torr). The ampule was placed in a three-zone furnace and heated at 5 °C min^{-1} to 625–600 °C source zone–growth zone. After 7 d, the reaction was cooled at 50 °C h^{-1} to a final temperature of 25 °C. The resulting grey-black crystals were removed from the ampule and aired in a fume hood. 1.516 g of $TaSe_3$ crystals were isolated (~38% yield).

Preparation of $TaSe_3$ (Batch 3): 1.7305 g (9.56 mmol) tantalum and 2.2712 g (28.8 mmol) selenium were ground gently together using an agate mortar and pestle before being transferred to a quartz glass ampule (10 mm ID, 14 mm OD, 170 mm length). The ampule

was evacuated and backfilled with Ar three times while submerged in a CH_3CN/CO_2(s) bath before being vacuum sealed (10^{-2} Torr). The ampule was heated/cooled according to the same parameters as batch 2. The resulting grey-black crystals were removed from the ampule and aired in a fume hood. 1.238 g of $TaSe_3$ crystals were isolated (~31% yield).

Characterization: Optical microscopy was performed with a Leica DVM6 digital stereoscope using Z-stacking to eliminate depth-of-field irregularities (**Figure 3-2**). SEM imaging and EDS measurements were performed with a FEI Teneo FE-SEM equipped with an Oxford Instruments X-MAX^N EDS detector. The secondary electron imaging in Figure 1d was performed with a Hitachi SU9000EA instrument. PXRD was conducted with a Bruker D8-Advance diffractometer (Co-Kα radiation) with the following parameters: 10-80 2θ at a rate of 0.1 s per step at 40 mA, 35 kV. The long crystals have smooth faces and straight edges that characterize high-quality $TaSe_3$ samples (**Figure 3-1**c-d and **Figure 3-2**). Powder x-ray diffraction (**Figure 3-3**) and energy dispersive spectroscopy (see Table 3-1 for compositional analysis) provided analytical results consistent with the standard structure of $TaSe_3$, albeit with some variation in Se content.

Table 3-1: EDS measurements and compositional analyses of representative crystals

	Ta	**Se**	**Se/Ta**
Theoretical at. %	25.0	75.0	3.00
Batch 1 experimental at. %	26.9	73.1	2.71
Batch 2 experimental at. %	24.3	75.7	3.11
Batch 3 experimental at. %	27.4	72.6	2.65

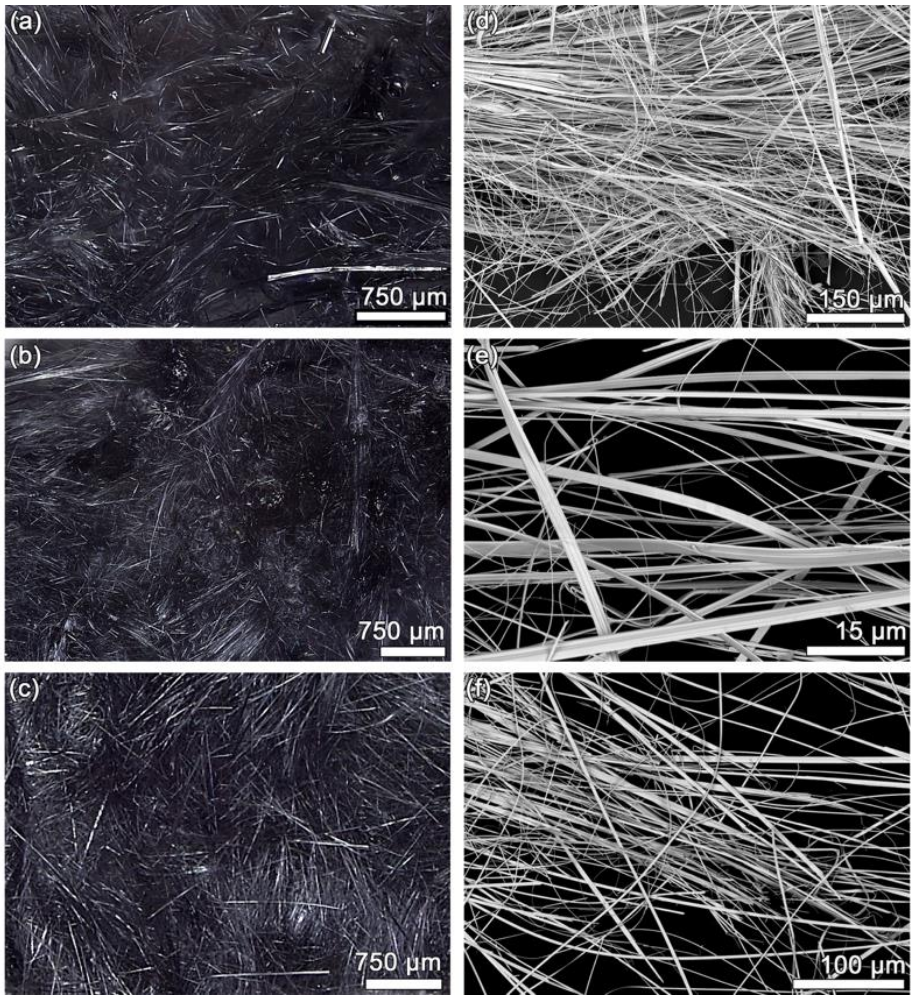

Figure 3-2: Optical and scanning electron microscopy of $TaSe_3$ crystals. (a) Optical microscopy images of crystals from (a) batch 1, (b) batch 2, and (c) and batch 3. SEM images of crystals from (d) batch 1, (e) batch 2, and (f) batch 3. Reprinted with permission from Barani et al., ACS Applied Materials & Interfaces. 13 (2021) 21527–21533. Copyright © 2021 American Chemical Society.

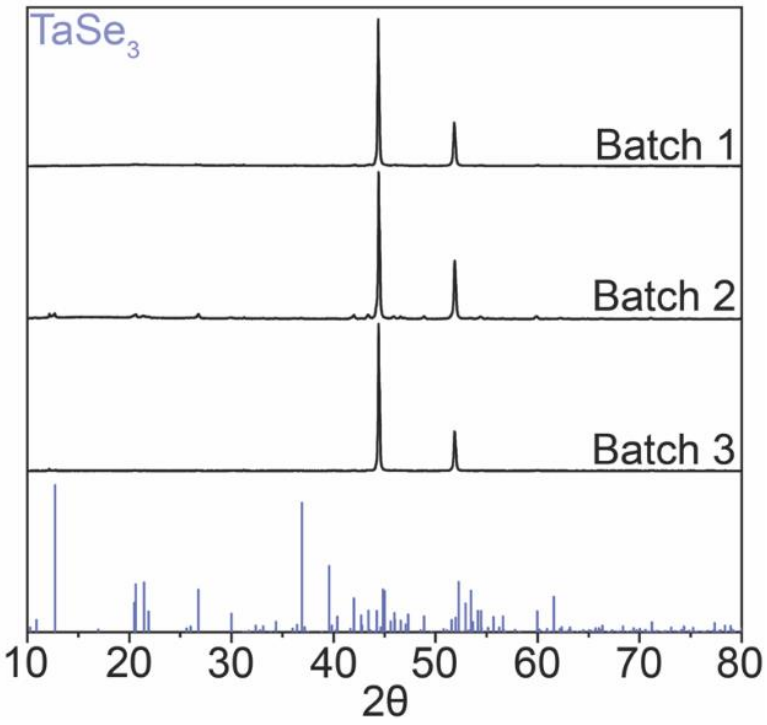

Figure 3-3: Powder x-ray diffraction of $TaSe_3$ crystals. Experimental PXRD patterns of $TaSe_3$ from batches 1–3 and corresponding $TaSe_3$ droplines in blue (JCPDS 04-006-6151). Reprinted with permission from Barani et al., ACS Applied Materials & Interfaces. 13 (2021) 21527–21533. Copyright © 2021 American Chemical Society.

3.2.2 Composite Preparation and Characterization

These CVT-grown $TaSe_3$ crystals were subjected to the LPE following the process reported by us elsewhere [1,83]. **Figure 3-4** summarizes our approach of mimicking the grid antenna design using material synthesis and presents optical images of the partially aligned fillers in the polymer composites and the resulting films. We used the "blade coating" method to prepare flexible thin films with a thickness of 100 µm ± 10 µm with a particular type of UV-cured polymer and exfoliated $TaSe_3$ as fillers. In this method, a small amount of polymer-filler solution is dropped cast on a rigid substrate with a smooth surface [84–

86]. A blade with an adjustable distance from the top surface of the substrate is gradually run over the mixture and spreads the compound over the substrate (**Figure 3-4**b). Using this technique, the quasi-1D fillers are aligned, to some extent, in the direction of the coating owing to the applied viscoelastic shear stress as a result of blade movement [84,85] (**Figure 3-4**c, **Figure 3-5**, **Figure 3-6**). All composites are thin and flexible (**Figure 3-4**d). The samples are referred to as A, B, C, and D throughout this manuscript, with filler concentrations of 2.2 vol%, 1.03 vol%, 1.87 vol%, and 1.61 vol%, respectively. We also fabricated a composite with random filler alignment using the compressional molding technique for comparison (Sample E). **Figure 3-7** illustrates the step-by-step preparation and characterization of the samples. Table 3-2 provides an overview of synthesized films in this study with their EMI shielding effectiveness. In this table, ϕ_f, t, and ρ are the filler volume fraction, thickness, and composite density. SE_T represents the total shielding effectiveness of the composite.

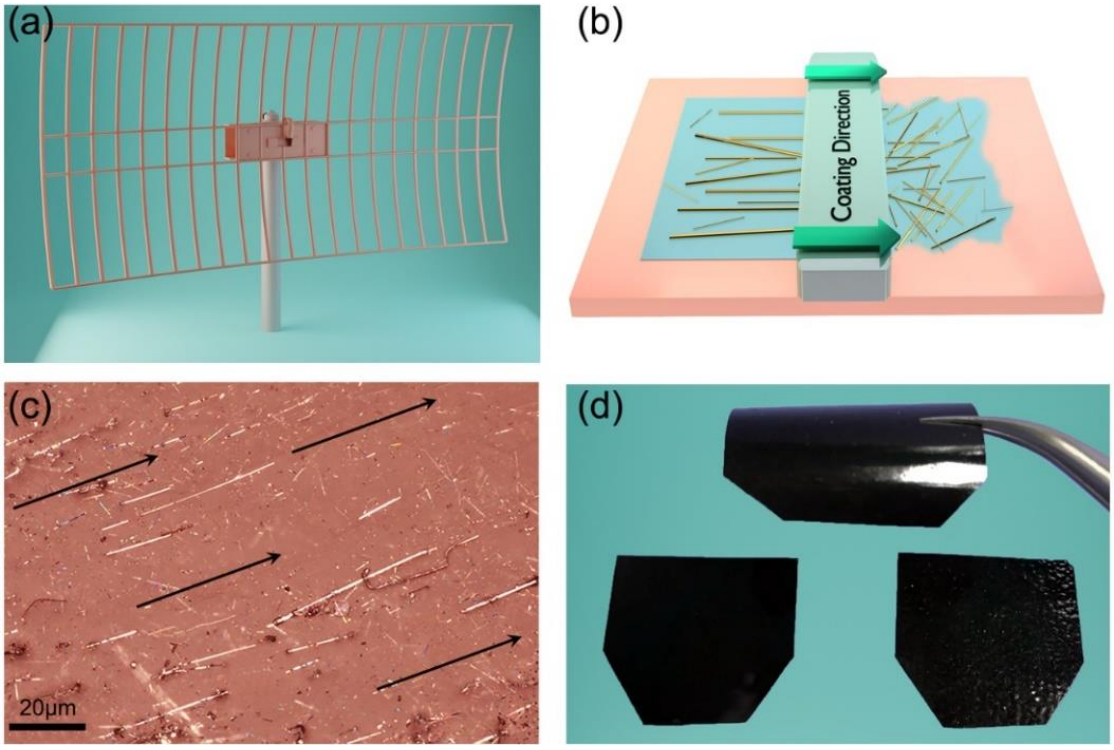

Figure 3-4: System-level concept and material-level implementation. (a) View of the aperture grid antenna illustrating the required function – polarization selectivity. (b) Schematic of the "blade coating" filler alignment process in the polymer films, in which the bundles of quasi-1D atomic threads function as metal wires in a grid antenna. (c) Optical microscopy image of the UV-cured polymer film with 1.8 vol% of $TaSe_3$ quasi-1D fillers. Note the aligned high-aspect-ratio $TaSe_3$ fillers along the coating direction. (d) Optical image of the resulting flexible polymer films with incorporated quasi-1D fillers, which mimic the action of a grid antenna. Reprinted with permission from Barani et al., ACS Applied Materials & Interfaces. 13 (2021) 21527–21533. Copyright © 2021 American Chemical Society.

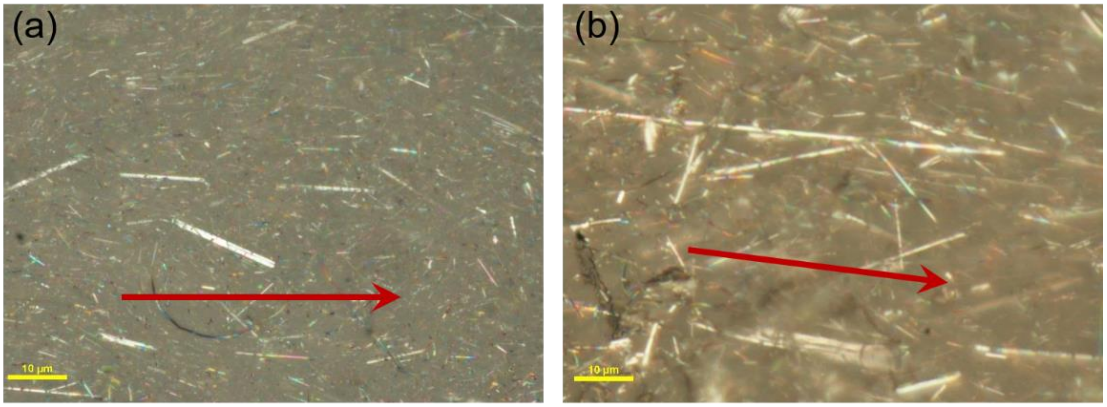

Figure 3-5: Optical microscopy images of sample C with aligned $TaSe_3$ fillers. The red arrows show the coating direction. Reprinted with permission from Barani et al., ACS Applied Materials & Interfaces. 13 (2021) 21527–21533. Copyright © 2021 American Chemical Society.

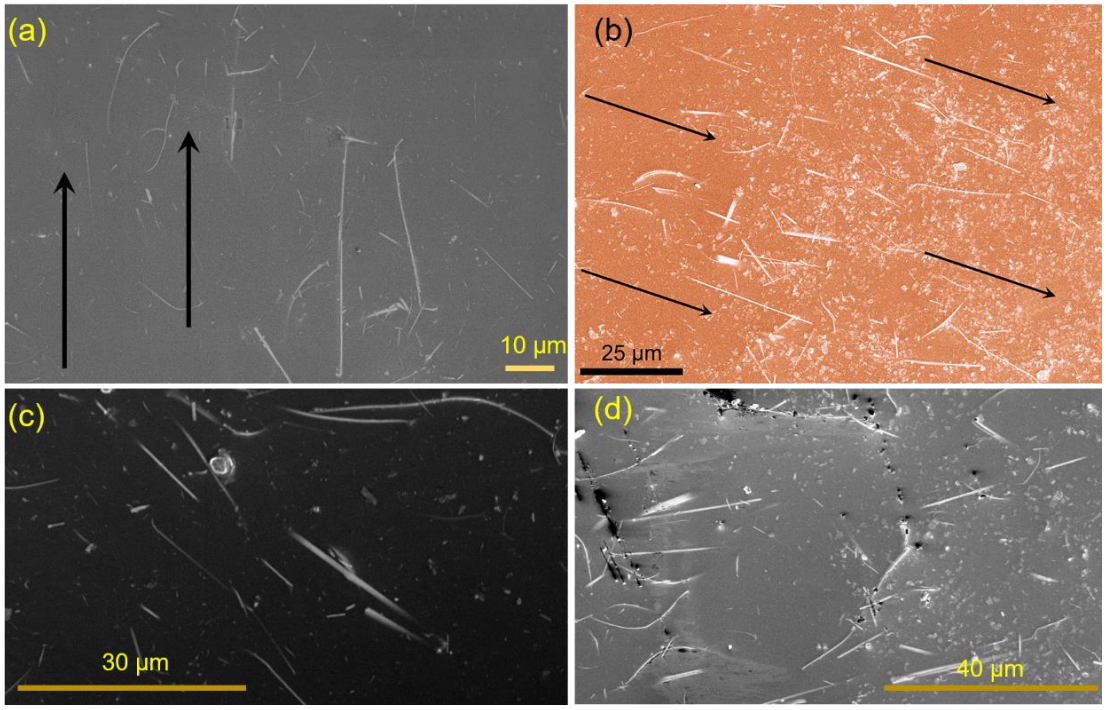

Figure 3-6: Scanning electron microscopy of the films with aligned $TaSe_3$ threads. Reprinted with permission from Barani et al., ACS Applied Materials & Interfaces. 13 (2021) 21527–21533. Copyright © 2021 American Chemical Society.

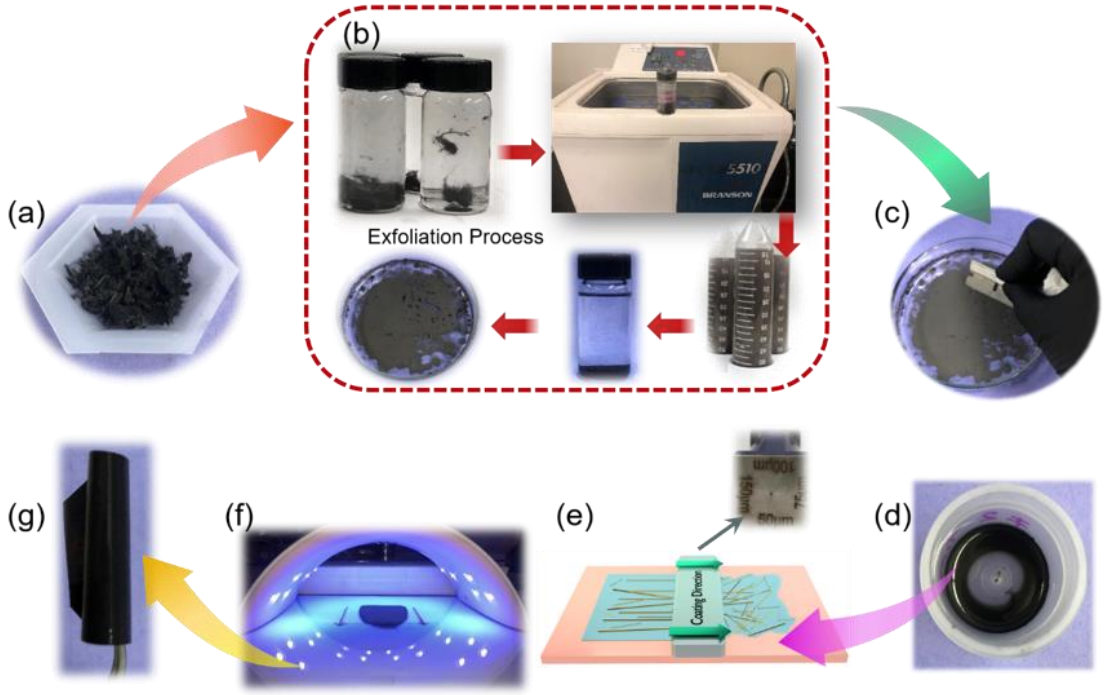

Figure 3-7: Preparation of composites with aligned quasi-1D fillers. (a) Optical image of $TaSe_3$ bulk crystal. (b) $TaSe_3$ crystals and fibers were added to acetone. Low-power bath sonication was used for the liquid phase exfoliation process. (c) The dispersion's precipitant part was collected and left in the ambient air for 24 hours to be completely dried. (d) $TaSe_3$ fillers were added to the UV polymer. The mixture was mixed at 500 rpm for 20 minutes using a high-shear speed mixer. (e) Schematic showing UV film preparation using Dr. blade coating method. (f) Optical image of the UV-cured polymer kept under UV light for 2 minutes to cure and solidify. (g) optical image of the flexible film with aligned $TaSe_3$ fillers. Reprinted with permission from Barani et al., ACS Applied Materials & Interfaces. 13 (2021) 21527–21533. Copyright © 2021 American Chemical Society.

Table 3-2: Characterization and EMI shielding effectiveness of synthesized films

Sample	ϕ_f (%)	t (μm)	ρ (gcm^{-3})	SE_T at 0° (dB) §	SE_T at 90° (dB) §	η (%)¥	Batch
Pristine Film†	0	100	1.23	0.54	0.52	-	-
Pristine Film‡	0	110	1.23	0.53	0.71	30	-
Sample A	2.2	90	1.34	3.16	7.2	128	3
Sample B	1.03	110	1.27	2.8	5.8	107	1
Sample C	1.87	110	1.32	6.4	10.74	68	2
Sample D	1.61	110	1.31	3.35	7.32	118	1,2
Sample E	1.6	110	1.3	7.2	6.9	-	2
SA Film	6	55	2	18.8	17.4	-	3

† Made by compressional molding
‡ Made by blade-coating
§ Measured at 8.2 GHz
¥ Enhancement defined as $\boldsymbol{\eta = (SE_{T,composite} - SE_{T,pristine})/SE_{T,pristine}}$

3.2.3 EM Shielding Measurements

We conducted EM testing of the prepared films in the X-band frequency range ($f = 8.2\ \text{GHz} - 12.4\ \text{GHz}$), which is pertinent to the current and future communication technologies. To determine the polarization selectivity, we followed the measurement protocols used in EMI shielding testing [30,32,45,87,88]. We measured the scattering parameters, S_{ij}With the two-port programmable network analyzer (PNA; Keysight N5221A). The scattering parameters are related to the coefficients of reflection, $R = |S_{11}|^2$And transmission, $T = |S_{21}|^2$. The measurements were carried out in a WR-90 commercial grade straight waveguide with two adapters at both ends with SMA coaxial ports. The samples were made a bit larger than the rectangular cross-section ($a = 22.8\ \text{mm}, b = 10.1\ \text{mm}$) of the central hollow part of the waveguide to prevent the leakage

of the EM waves from the sender to the receiver antenna. The cut-off frequency for different fundamental transverse electric (TE) modes in rectangular-shaped waveguides is $(f_c)_{mn} = \frac{1}{2\pi\sqrt{\mu\varepsilon}} \sqrt{(m\pi/a)^2 + (n\pi/b)^2}$ [Hz] where m and n are positive integer numbers [89]. Therefore, the dominant EM mode in WR-90 waveguide is TE_{10} mode, with the electrical field (E) oscillating in the vertical direction perpendicular to the larger side of the inlet aperture (see **Figure 3-8**). The frequencies of other modes exceed the X-band frequency range and are not of interest in this study.

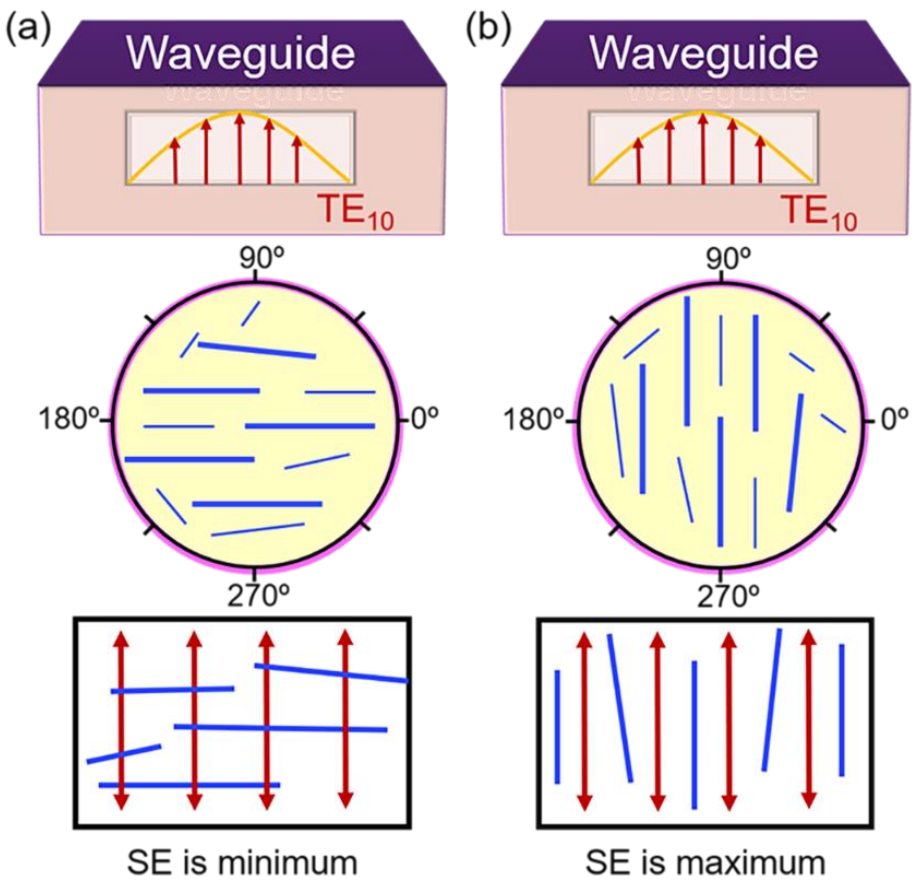

Figure 3-8: Schematic of the experimental waveguide and polarization-dependent EMI shielding. Front-view schematic of the standard WR-90 waveguide and polarization of the allowed fundamental TE_{10} mode propagating in this type of waveguide at a given frequency range. (a) At $\alpha = 0°$, the bundles of the quasi-1D atomic chains are parallel to the large side of the aperture and perpendicular to the electric field of TE_{10} mode. (b) At $\alpha = 90°$, the bundles are perpendicular to the large side of the aperture and, thus, parallel with the electric field of TE_{10} mode. Reprinted with permission from Barani et al., ACS Applied Materials & Interfaces. 13 (2021) 21527–21533. Copyright © 2021 American Chemical Society.

3.3 Results and Discussion

To investigate the effect of the filler alignment on the EM characteristics of the composites, measurements were carried out at different sample orientation angles (α) by rotating the

sample about the guide axis. Note that α is the angle between the aligned filler chains in the composite with respect to the larger side of the guide's aperture. Therefore, at $\alpha = 0°$, the fillers are parallel to the larger side, and E is perpendicular to them. The front-view schematic of the WR-90 waveguide, the electric field configuration of TE_{10} mode, and its mutual orientation with respect to the quasi-1D fillers of the composites are shown in **Figure 3-8**. **Figure 3-9** presents the reflection (SE_R), absorption (SE_A), and total (SE_T) shielding effectiveness of samples A and C with 2.2 vol% and 1.87 vol% filler concentration as a function of EM frequency when the polarization of the incident EM wave is either parallel with (||) or transverse to (⊥) the quasi-1D fillers. Note that the shielding effectiveness of the films is significantly enhanced when E is parallel with the filler alignment comparing to the case it is perpendicular to the filler chains. For samples A and C, the enhancement in total shielding effectiveness is defined as $\eta = (SE_{T,\parallel} - SE_{T,\perp})/SE_{T,\perp}$, is 128% and 107%, respectively (see Table S2 for more details).

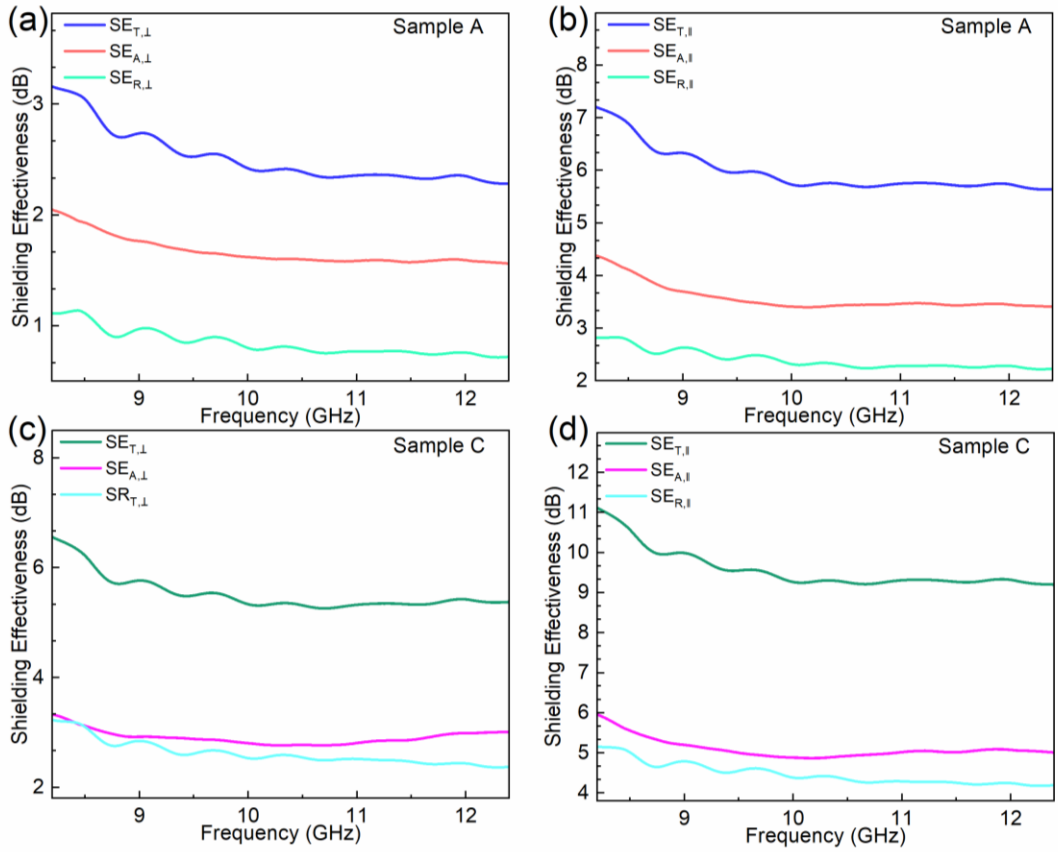

Figure 3-9: Electromagnetic shielding effectiveness at different orientations. Reflection (SE_R), absorption (SE_A), and total (SE_T) EMI shielding effectiveness of (a-b) sample A and (c-d) sample C for two cases of the EM wave polarization transverse to (⊥) and parallel with (||) the quasi-1D fillers. Note that the EMI shielding is significantly higher when the polarization is parallel to the filler alignment. Reprinted with permission from Barani et al., ACS Applied Materials & Interfaces. 13 (2021) 21527–21533. Copyright © 2021 American Chemical Society.

We measured the angular dependence of SE_T of all four samples at the constant frequency of $f = 8.2$ GHz to elucidate the effect of the filler alignment on EM shielding properties of the composites. The results of these measurements are presented in **Figure 3-10**. Note that at $\alpha = 0°$, E is perpendicular to the filler atomic chains. One can notice the sinusoidal characteristic of the SE_T (solid lines) with a period of 180 degrees as a function of α. When the fillers are aligned in one direction, the composite film becomes anisotropic, given that

the embedding matrix is isotropic. This behavior is consistent for all examined samples with different loading of the aligned quasi-1D fillers. If the fillers were randomly distributed inside the polymers, one would expect isotropic EMI shielding properties, *i.e.*, with rotating the sample, EMI properties would remain almost the same. In fact, the shielding effectiveness of the samples prepared by the "compressional molding" with randomly oriented fillers does not exhibit any angular dependency characteristic.

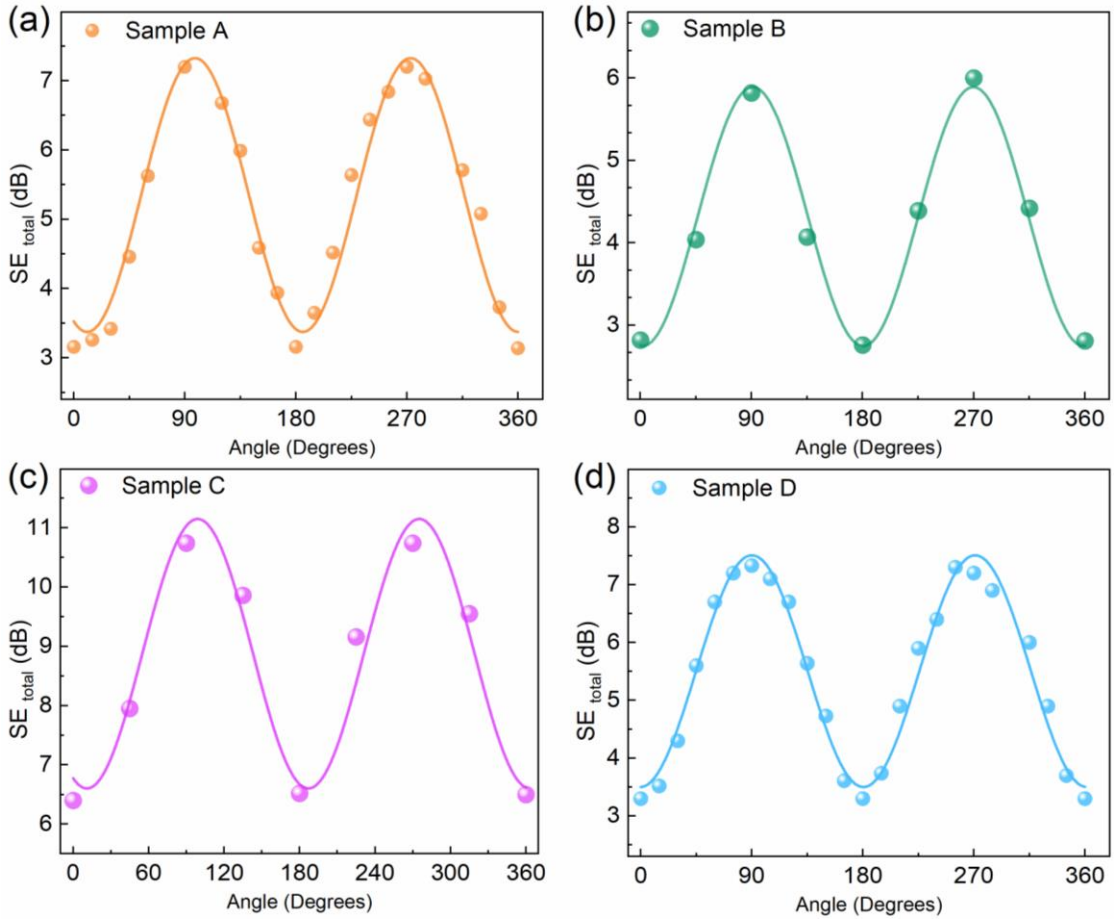

Figure 3-10: Electromagnetic-polarization selective composites. Total shielding effectiveness of samples with filler content of (a) 2.2 vol%, (b) 1.03 vol%, (c) 1.87 vol%, and (d) 1.61 vol% as a function of the composite orientation angle α, measured at 8.2 GHz frequency. At $\alpha = 0°$, the polarization of the EM wave is perpendicular to the filler alignment. The results are fitted with sine functions. Note the periodicity of the SE_T with a period of 180 degrees. Reprinted with permission from Barani et al., ACS Applied Materials & Interfaces. 13 (2021) 21527–21533. Copyright © 2021 American Chemical Society.

The periodic EM shielding characteristics observed in our composites originate from two different effects: (i) the prolate ellipsoid needle-like geometry of the fillers, assuming semi-axes of $a_x > a_y = a_z$; and (ii) the anisotropic complex permittivity properties of the quasi-1D $TaSe_3$ fillers [90]. Because the filler inclusion is low in all the samples, the Maxwell-

Garnett (M-G) effective medium theory can be used to explain the observed characteristics [90,91]. For composites with aligned dielectric fillers, the M-G effective complex permittivity of the composite along the *x* direction, $\varepsilon_{c,x}$, can be described as:

$$\varepsilon_{c,x} = \varepsilon_p + \phi_f \varepsilon_p \frac{\varepsilon_f - \varepsilon_p}{\varepsilon_p + (1-\phi_f) N_x (\varepsilon_f - \varepsilon_p)} \quad (1)$$

In this equation, ε_p and ε_f are the permittivity of the polymer and filler and ϕ_f is the filler volume fraction. For ellipsoidal fillers, the depolarization factor, $N_x = (\frac{1-e^2}{2e^3})(\ln\frac{1+e}{1-e} - 2e)$ in which the eccentricity is $e = \sqrt{1 - a_y^2/a_x^2}$.[32] Considering the large aspect ratio of the exfoliated fillers ($a_x \gg a_y$), it can be easily inferred that the effective permittivity of the composites would be largely different along different directions, *i.e.*, parallel with and perpendicular to the aligned atomic chains. Note that to obtain the effective permittivity along other directions, y and z, the depolarization factor should be replaced by N_y and N_z And calculated accordingly.

The special geometrical shape of the aligned fillers is not the only parameter causing anisotropic behavior of composites with quasi-1D fillers. Owing to the monoclinic crystal structure of $TaSe_3$, the EM properties of the fillers are highly directional. The polarized reflectance data of $TaSe_3$ exhibits metallic characteristics in the infrared region [63]. To the best of our knowledge, there is no data on the dielectric properties of $TaSe_3$ in the microwave region. However, one can describe the complex dielectric parameter of $TaSe_3$

as a function of EM frequency, ω, by the Lorentz-Drude model, $\varepsilon(\omega) = \varepsilon_\infty - \frac{\omega_p^2}{\omega^2 - i\omega\Gamma_0} + \sum_{n=1}^{m} \frac{\omega_{p,n}^2}{\omega_{0,n}^2 - \omega^2 - i\omega\Gamma_n}$ [63]. In this model, ε_∞ is the permittivity of the material when the frequency goes to infinity, m is the number of the oscillators with the frequency of $\omega_{0,n}$ and the lifetime of $1/\Gamma_n$, respectively. The plasma frequency, $\omega_p = \sqrt{Nq^2/m^*\varepsilon_0}$, depends on the electron density, N, electron absolute charge, q, and the effective mass of electrons, m^*. The second and third terms are associated with the interaction of EM waves with the intra-band, or free-electrons, and inter-band, or bound-electrons, respectively. The $\hbar\omega_p$ in $TaSe_3$ along the crystallographic "a" (perpendicular to the chains) and "b" (along the chains) axes are 0.42 eV and 0.68 eV [63]. Therefore, one would expect an anisotropic frequency-dependent reflectance (R) and conductance (σ) along with and perpendicular to the atomic chains in the microwave region, with both parameters being larger in the direction along the atomic chains. Such strong, anisotropic reflectance properties have been reported for $TaSe_3$ in the EM energy range between 0.05 eV to 5 eV, previously [92].

Figure 3-11 (a-b) exhibits the angular-dependent reflection, absorption, and transmission shielding effectiveness and coefficients of sample D, respectively. The four-fold symmetry of all plots shown in both panels confirms the alignment of quasi-1D fillers. More importantly, as is seen in **Figure 3-11** (b), reflection is the dominant mechanism of shielding the EM waves in the microwave region. The reflection coefficient increases more than two times comparing the two extreme cases of $\alpha = 0°$ and $\alpha = 90°$ whereas the absorption almost does not vary. The four-fold symmetric transmission curve in **Figure**

3-11 (b) demonstrates the applicability of prepared, flexible films as microwave attenuators or grid polarizers. For reference, the shielding effectiveness in the samples prepared by the "compressional molding" does not reveal any angular dependence (see **Figure 3-12**a, **Figure 3-13**, and **Figure 3-13**). The observed EM property is similar to the linear dichroism, which has been reported in the visible light region for bulk and exfoliated MPX_3 crystals with strong optical anisotropy [93,94]. Bulk TiS_3 exhibits a linear dichroism with transmittance ratio of $\zeta = T_{\perp}/T_{\parallel} = 30$ at the wavelength of 633 nm [95].

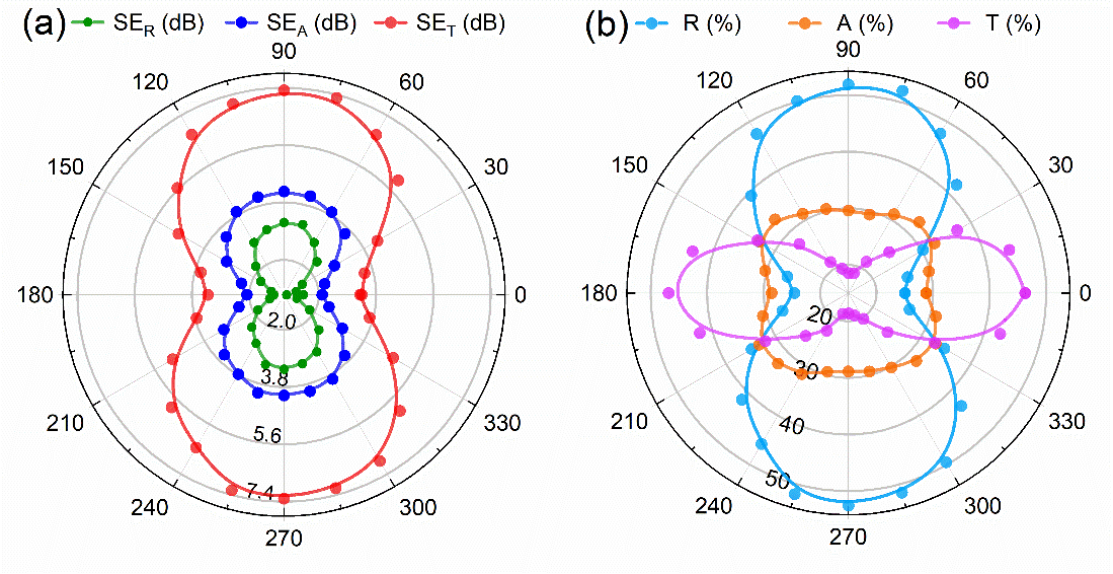

Figure 3-11: Contribution of different mechanisms to interaction with EM waves. The angular dependency of (a) the reflection, absorption, and total shielding effectiveness, and (b) reflection absorption, and transmission coefficients of sample D with 1.61 vol% aligned quasi-1D $TaSe_3$ fillers. Note the extremes at 0 and 90 degrees and the symmetry of the curves in both panels, confirming the alignment of fillers inside the polymer matrix. As shown in (b) the reflection is highly correlated with sample orientation, whereas absorption varies weakly. Reprinted with permission from Barani et al., ACS Applied Materials & Interfaces. 13 (2021) 21527–21533. Copyright © 2021 American Chemical Society.

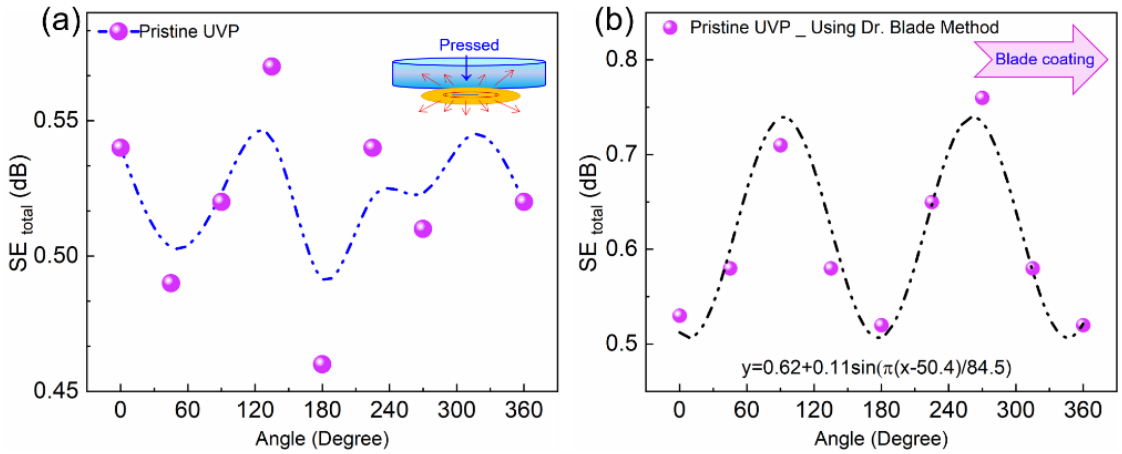

Figure 3-12: Total shielding effectiveness of pristine UV polymer synthesized by (a) compressional molding and (b) directional blade-coating methods. Reprinted with permission from Barani et al., ACS Applied Materials & Interfaces. 13 (2021) 21527–21533. Copyright © 2021 American Chemical Society.

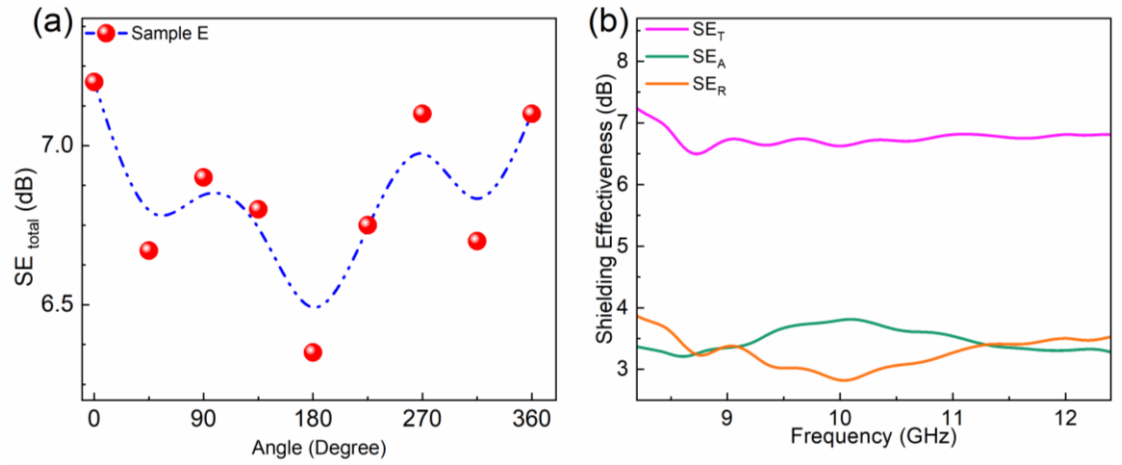

Figure 3-13: Total shielding effectiveness of UV-cured polymer with 1.6 vol% $TaSe_3$ fillers prepared by compressional molding method as a function of (a) films' orientation angle and (b) frequency. The data in (a) and (b) were acquired at a frequency of 8.2 GHz and an orientation angle of zero degrees, respectively. Note the random dependence of SE_{total} on the orientation angle of the film in (a). There is no periodic behavior here. Reprinted with permission from Barani et al., ACS Applied Materials & Interfaces. 13 (2021) 21527–21533. Copyright © 2021 American Chemical Society.

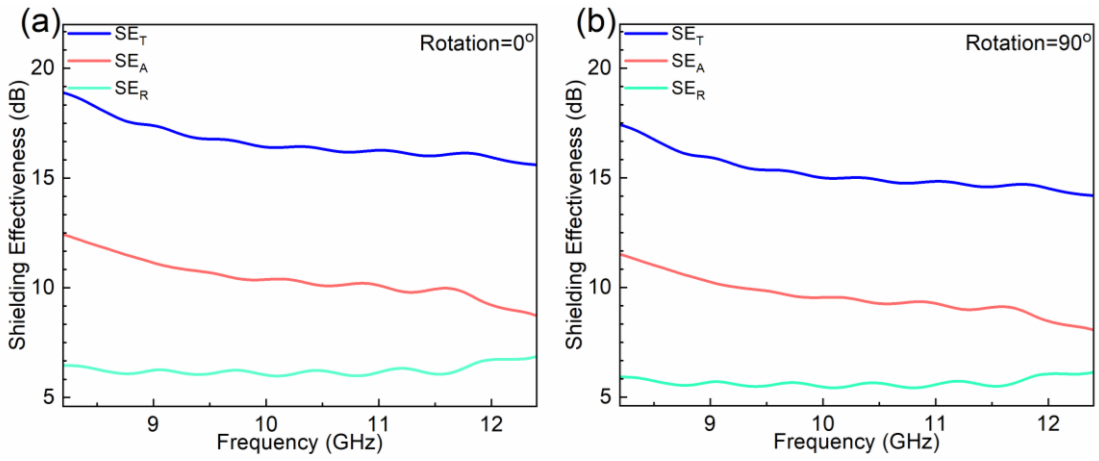

Figure 3-13: Reflection (SE_R), absorption (SE_A), and total (SE_T) electromagnetic interference shielding effectiveness of sodium alginate films with randomly dispersed quasi-1D $TaSe_3$ threads as fillers in the film. (a) and (b) shows randomly chosen reference point 0 and 90 degrees, respectively. Reprinted with permission from Barani et al., ACS Applied Materials & Interfaces. 13 (2021) 21527–21533. Copyright © 2021 American Chemical Society.

3.4 Summary and Conclusions

In conclusion, we have described the preparation and properties of flexible polymer composite films with aligned metallic fillers made of bundles of quasi-one-dimensional (1D) van der Waals metal, characterized by high current density. The material functionality, embedded at the nanoscale level, was achieved by mimicking the design of an electromagnetic aperture grid antenna. The synthesized composites use the quasi-1D van der Waals nanowires as the grid building block incorporated within the thin-film structure. The measurements conducted in the X-band frequency range demonstrated that the electromagnetic transmission through such films could be varied by changing the mutual orientation of the quasi-1D fillers and polarization of the electromagnetic wave. The films with low loading of the quasi-1D fillers (< 2 vol. %) and only partial alignment

of the fillers can already produce ~5 dB variation in the transmitted signal. We argue that such polarization-sensitive polymer films with quasi-1D fillers can be used for advanced electromagnetic interference shielding in future communication systems.

Chapter 4 Efficient Terahertz Radiation Absorption by Dilute Graphene Composites

4.1 Introduction

It is useful to put the research of composites with quasi-1D van der Waals fillers in the general context of composite research. A comparison with composites that utilize quasi-2D fillers such as graphene would be particularly illustrative. In this chapter, we provide our results for composites with low loading of graphene. We specifically address the performance of such composites in the high-frequency range. The shielding of the electromagnetic (EM) energy in the terahertz (THz) frequency range is important for both reducing EM interference among various devices and protecting humans [96–98]. While efficient THz sources are still under development, electromagnetic interference (EMI) shielding approaches for the relevant frequency band have already attracted significant attention [99,100]. Absorbing EM radiation in the THz band and simultaneously meeting all practical constraints can be challenging. There are numerous requirements imposed on the materials used for EM interference (EMI) shielding, such as the thickness of the coating layer, weight limits, mechanical and thermal properties, electrical isolation or conductance, reliability, and cost. Absorbing EM energy rather than reflecting it back to the environment is often required for commercial, *e.g.,* 6G technology and defense applications [101]. Many

existing EMI shielding materials for the high-frequency bands, including metallic coatings, mostly redirect the EM energy by reflection owing to their high electrical conductivity. The reflection protects electronic components but, at the same time, may negatively affect human health [97,98].

An alternative promising approach for EMI shielding is the use of polymer-based materials with electrically conductive fillers [1,102,103]. Recent studies reported the use of carbon fibers [104,105], carbon black [105,106], bulk graphite [107,108], carbon nanotubes [109–112], reduced graphene oxide [31,113–117], graphene [118,119] and a combination of carbon allotropes with other particles [117,119–122]. Graphene was used successfully as the filler in composites, which were tested in the MHz and GHz frequency ranges [115,119,123,124]. There were a few reports on the use of graphene composites in the sub-THz and THz range [33,40,125,126]. Experimental and theoretical studies with individual graphene layers and graphene meta-surfaces suggest that graphene interacts efficiently with EM radiation in the THz range [127–131]. Available data suggest that graphene particularly absorbs the radiation well in the high GHz frequency range rather than reflecting it back to the surroundings [33]. Further work is needed to understand EM characteristics of such composites at different loading of graphene and assess their application potential. In this chapter, we report the results of testing of composites with epoxy base and low loadings of graphene, below 1.2 wt. %. The term graphene, in the context of composite studies, is used to identify a mixture of graphene and few-layer graphene (FLG) with the micrometer-scale lateral dimensions.

4.2 Composite Preparation and Characterization

For this study, we utilized FLG powder (xGnP®H-25, XG-Sciences, U.S.A.) as a starting material to prepare the composites. The composite samples were prepared by mixing graphene flakes with epoxy using a high-shear speed mixer (Flacktek Inc., U.S.A. with the in-house designed elements) at 800 rpm and 2000 rpm each for 5 minutes. The mixture was vacuumed for 30 minutes. After that time, the curing agent (Allied High-Tech Products, Inc., U.S.A.) was added in the mass ratio of 12: 100 with respect to the epoxy resin. The compound was mixed and vacuumed one more time and left in the oven for ~2 hours at 70 ℃ in order to cure and solidify. Microscopy characterization data are presented in **Figure 4-1**. The as-synthesized FLG flakes have average lateral dimensions in the range from 15 μm to 25 μm, an average FLG thickness of ~15 nm, and a typical surface-area-to-mass ratio of 50 m^2/g to 80 m^2/g. It should be noted that the actual thickness of the graphene fillers in the composite is less due to the further exfoliation during the composite preparation, which includes the use of the high-shear mixer. The "bulk" in-plane and cross-of-plane electrical conductivity of the graphene flakes are up to ~10^7 S/m and ~10^2 S/m, respectively. We found the optimum exfoliation and shear mixing parameters *via* extensive trial-and-error effort. A particular emphasis was on obtaining a uniform, even dispersion of graphene fillers. The samples were prepared in the form of disks with a diameter of 25.6 mm and thicknesses from 0.9 mm to 1.0 mm. The quality of the dilute graphene composites was verified using scanning electron microscopy (SEM) and Raman spectroscopy. Raman

spectroscopy with the laser excitation of 488 nm was used to characterize the epoxy and composite samples. **Figure 4-2** shows the obtained data for the pristine epoxy, graphene filler, and the epoxy with 1.0 wt. % graphene loading. As seen, the Raman spectra for the composite is overloaded with the many active Raman peaks of the pristine epoxy. However, the graphene Raman signature peak at 1580 cm^{-1} is clearly observed.

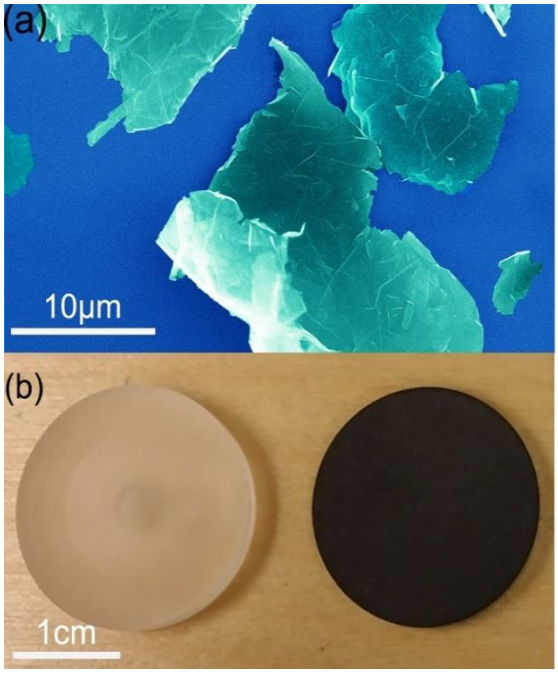

Figure 4-1: (a) Scanning electron microscopy image of the graphene fillers with the average lateral dimension of ~25 μm used in the composite preparation. (b) Optical image of the pristine epoxy (left) and epoxy with 1 wt. % of graphene loading (right). Reprinted with permission from Barani et al., Applied Physics Letters. 120 (2022) 063104. Copyright © 2022 AIP Publishing.

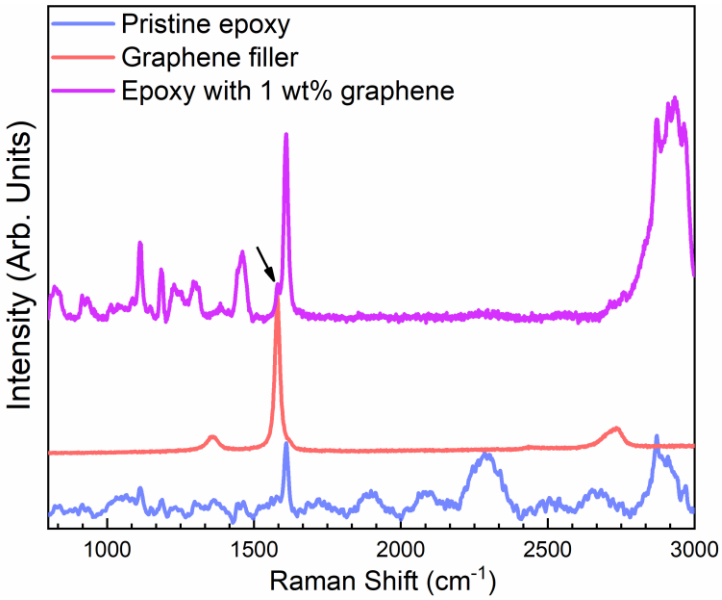

Figure 4-2: Raman spectra of pristine epoxy, graphene filler, and epoxy composite with 1 wt. % graphene loading. The arrow in the purple curve shows graphene's Raman signature peak at 1580 cm^{-1}. Reprinted with permission from Barani et al., Applied Physics Letters. 120 (2022) 063104. Copyright © 2022 AIP Publishing.

4.3 Experimental Method

The EMI shielding effectiveness of the dilute graphene composites was investigated using the Terahertz-Time Domain Spectroscopy (THz-TDS) system (Toptica Photonics AG) [132–134]. A train of short THz pulses of ~1 ps duration and the repetition rate of 100 MHz was sent through the sample pellets made of the composites or was reflected from their surfaces depending on the experimental geometry. The high-mobility InGaAs photoconductive antennas were used as both transmitter (Tx) and receiver (Rx). The antennas were fed with an all-fiber pulsed laser centered at 1.56 µm wavelength. As opposed to 1 ps duration of the THz pulses, the duration of the laser pulses was much

shorter, $\tau \sim 80\ fs$. Owing to this property, a time narrow fraction of the THz pulse could be sampled at one given delay of the laser pulse. To retrieve temporal profiles of the pulses from the THz pulse train, a variable delay stage scanned the THz wave packet with the laser probe pulse. The high repetition rate of the pulse train allowed us to obtain effective wave packets sampling at the rate of ~30 traces/s and to average over $1000 - 2000$ pulses during a single minute duration of an individual measurement. A Fast Fourier Transform (FFT) algorithm was used to calculate the amplitudes and phases of the transmitted and reflected fields as a function of frequency.

A schematic of the THz-TDS experimental setup is shown in **Figure 4-3**. In addition to the laser part, it includes the THz beam delivery part based on the so-called $4f$ optical arrangement [135], consisting of four 90° off-axis parabolic mirrors. The two of these mirrors, applied to compensate for the divergence of the beam, were located after the transmitter and after the sample. The other two provided focusing before the pellet and detector. The focal lengths of the mirrors were chosen to ensure symmetrical propagation of the beam on the distance from the radiation source to the sample and from the sample to the detector. The diameter of all mirrors was 25.4 mm, and the shorter and longer focal lengths were 50.8 mm and 101.6 mm, respectively. Using these values one can estimate that the Rayleigh lengths $z_R = \pi\omega_0^2/\lambda$ (ω_0– beam waist in focus, $\lambda = c/f$, where c– speed of light and f– radiation frequency) of the pulse frequency components ($0.25 - 4.0$ THz) were not shorter than ~ 1.5 mm, *i.e.*, sufficiently longer than the thickness of the composite pellet. Such a situation typically indicates good collimation of the beam near the focal spot,

providing equal absorption lengths for all frequency components. Note that the setup shown in **Figure 4-3** was used only for the measurements of the transmission coefficients, *T*. To measure the reflection coefficients, *R*, the receiver was placed on the same side of the sample as the transmitter, and the amplitude of the EM radiation reflected from the surface of the pellet was measured. Special care was taken to deliver the beam at nearly normal incidence with respect to the sample, resulting in a small deviation of only 4° from the vertical.

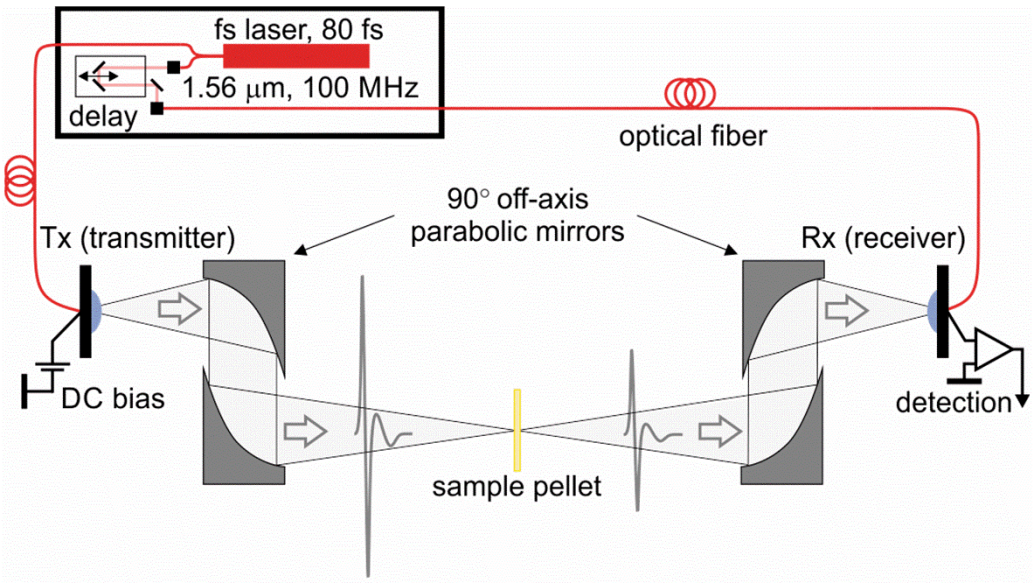

Figure 4-3: Schematic of the experimental setup used for the measurements in the high-frequency range from 0.25 THz to 4.0 THz. Reprinted with permission from Barani et al., Applied Physics Letters. 120 (2022) 063104. Copyright © 2022 AIP Publishing.

A procedure involving measurements of the transmission, *T*, and reflection, *R*, coefficients commonly used in the *S*-matrix method [110] was applied to determine the absorption properties of composites. The transmission coefficient of composites was calculated by

measuring the amplitude of the electric field transmitted through the sample, $\hat{E}_{21s}$, and through the reference field, $\hat{E}_{21e}$. The latter was measured in an empty space after the removal of the composite. On the basis of these two measurements, T was calculated as:

$$T = |S_{21}|^2 = \left|\hat{E}_{21s}/\hat{E}_{21e}\right|^2. \quad (1)$$

Similarly, the reflection coefficient was determined by measuring the electric field, $\hat{E}_{11s}$, reflected from the surface of the epoxy composite. The reference field, $\hat{E}_{11s}$, was measured with the THz pulse reflected from the polished metallic plate, which is a good approximation of an ideal reflector in the THz band. An equivalent of Eq. (1) was used to calculate R as follows:

$$R = |S_{11}|^2 = \left|\hat{E}_{11s}/\hat{E}_{11m}\right|^2. \quad (2)$$

The electric fields from Eqs. (1) and (2) and the phase relations required to calculate the amplitude ratios were provided by the FFT. Finally, to determine the absorption characteristics of EMI shielding material, the measured values of *T* and *R* were used to calculate the effective absorption coefficient, A_{eff}, defined as:

$$A_{eff} = (1 - R - T)/(1 - R). \quad (3)$$

Compared with the standard definition of the absorption coefficient $A = 1 - R - T$, the modified definition describes the actual absorption of the composite material accounting for the fact that some part of the incident EM energy is always reflected from the surface

of the sample. The total shielding effectiveness, SE_T, and shielding *via* different mechanisms of reflection, SE_R, and absorption, SE_A, can be calculated knowing R and A_{eff} as follows [33]:

$$SE_R = -10\log(1 - R), \quad (4)$$

$$SE_A = -10\log(1 - A_{eff}), \quad (5)$$

$$SE_T = SE_R + SE_A. \quad (6)$$

4.4 Results and Discussion

Figure 4-4 (a) shows the reflection coefficient, R, for the pristine epoxy and three epoxy-based composites with the graphene loading ranging from 0.8 wt. % to 1.2 wt. %. The data are presented in the frequency range from 0.25 THz to 4 THz. The oscillations of the reflectivity at low frequencies are due to the multiple reflections from the sample's front and back surfaces, causing Fabry–Pérot interference features. The sharp spikes at $f >$ 1.5 THz are due to the absorption by the water molecules in the atmosphere. Within the whole frequency range, the reflection from the epoxy-based composites is small. **Figure 4-4** (b) presents the reflection shielding effectiveness of samples as a function of frequency. One can see that the shielding by reflection in the whole frequency range is below 1 dB.

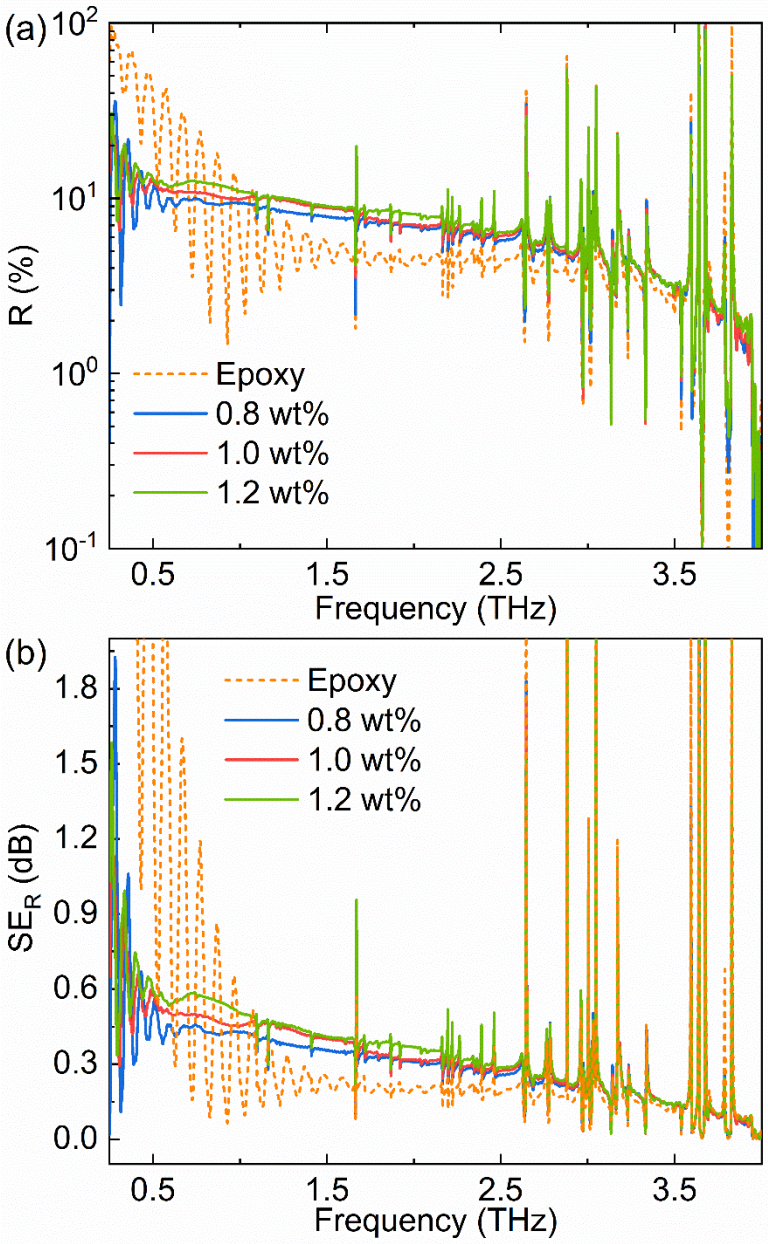

Figure 4-4: (a) Reflection coefficient, R, and (b) reflection shielding effectiveness, SE_R, of the pristine epoxy and the composites with low loadings of graphene as a function of frequency. Note that the shielding by reflection is negligible in all composites. The experiments have been conducted using an aluminum plate as a reference. Reprinted with permission from Barani et al., Applied Physics Letters. 120 (2022) 063104. Copyright © 2022 AIP Publishing.

The transmission coefficient, T, for the same set of samples is shown in **Figure 4-5** (a). It is interesting to note that the transmission decreases with the increasing frequency. For composites with graphene loading of 1.2 wt. %, and at $f = 1.6$ THz, $T \sim 10^{-7}$%, confirming that almost all the incident EM wave is blocked by the composites. This level of the measured signal is already close to the sensitivity limit of the measurements. As expected, the higher the graphene loading, the smaller the transmission. The exception is only observed at the frequencies below $f = 0.4$ THz, where the transmission spectra for the composites with 1.0 wt. % and 1.2 wt. % loading of graphene coincide. The low reflection and low transmission of the epoxy-based composites in the THz frequency band show that this material effectively shields EM radiation mainly due to the absorption. It is important to note that our dilute graphene composites are electrically insulating, and their resistivity could not be measured by standard four-probe measurement setup. Our previous studies with the same polymer and graphene fillers have shown that the electrical percolation occurs at ~ 5 wt. % of the filler loading [33]. This is a loading fraction required for graphene fillers to physically touch each other and form a conductive path. The dashed lines in **Figure 4-5** (a) show the result of recalculation of the experimental data for 1-mm thick sample to the thickness of 200 μm. Given that most of the loss is caused by absorption mechanism (*i.e.*, $SE_R < 1$ dB), we used Beer-Lambert law to extrapolate the transmission and total shielding effectiveness in thinner samples. It is seen that even these thin layers can protect effectively at the THz frequency band. The total shielding effectiveness of the dilute graphene composites, SE_T, is presented in **Figure 4-5** (b). One can see that 1.2 wt. % graphene composites provide total shielding above ~ 70 dB at $f \sim 1.6$ THz, which is more

than sufficient for many industrial applications. One should note that generally, it is accepted that if the total shielding exceeds ~15 dB, the multi-reflection effect can be neglected. Multiple reflections have not been observed in our dilute graphene samples above 0.25 THz owing to the strong absorption. The latter was verified from the analysis of the delayed pulses following the first transmitted pulse. Such pulses give rise to distinguishable Fabry-Perot interference patterns in the measured spectra, for example, of pristine epoxy, which has low absorption.

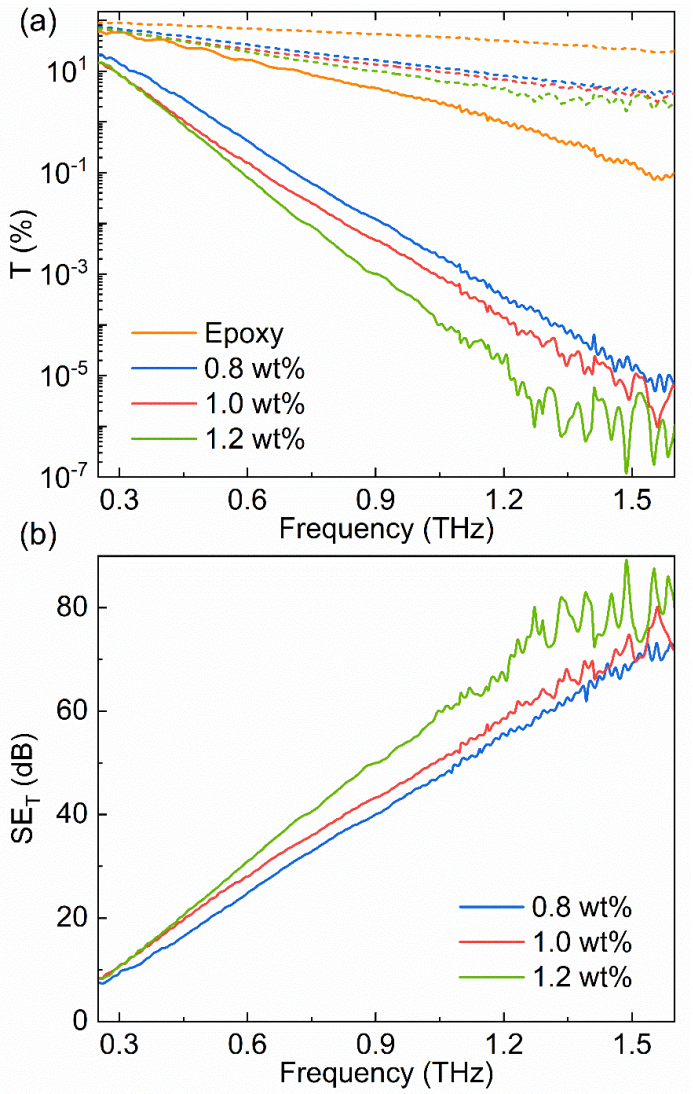

Figure 4-5: (a) Transmission coefficient, T, and (b) total shielding effectiveness, SE_T of the composites with low loadings of graphene as a function of frequency. Note that SE_T increases linearly with the frequency. For $f \geq 1.6$ THz, the shielding effectiveness of the dilute graphene composites increases beyond the measurable upper limit of the instrument. The solid lines are the experimental results for samples with 1 mm thickness. The dashed lines in panel (a) are the calculated T and SE_T for 200 µm thick samples, provided for comparison. Note the change in the slopes of the curves at f=0.4 THz. Reprinted with permission from Barani et al., Applied Physics Letters. 120 (2022) 063104. Copyright © 2022 AIP Publishing.

The frequency dependence of A_{eff} and SE_A are shown in **Figure 4-6** (a-b). The data demonstrate conclusively that absorption is the dominant mechanism for blocking the EM waves in our dilute graphene polymer composites. One can see that, especially at frequencies $f > 0.6$ THz, these composites absorb EM radiation almost completely. The composites with 1.2 wt.% of graphene loading provides ~45 dB and ~80 dB shielding effectiveness by absorption at $f \sim 0.8$ THz and $f = 1.6$ THz, respectively (**Figure 4-6** (b)). These samples reveal substantially higher absorption shielding effectiveness compared to PDMS composites with 3 wt.% graphene content in the near-THz frequency range [40].

At this point, the physical mechanism of THz absorption in dilute graphene composites can be analyzed only qualitatively. We start with comments on the intrinsic properties of graphene fillers. The electrical conductivity of graphene is a strong function of the carrier concentration, *e.g.*, Fermi level position, which can change over a wide range. Unlike in individual graphene devices [7], where gating can provide accurate information on the Fermi level position, in composites, everything changes due to the "chemical doping" from the base material. It is not possible to determine exactly the electrical conductivity of graphene fillers inside the matrix. Typical values of the in-plane electrical conductivity reported for large layers of chemical vapor deposition (CVD) grown graphene are in the range of 10^3 - 10^6 S/cm [136,137]. The sheet resistance for CVD graphene was reported to be in the range of 100 to 300 W/sq [138]. The “chemical doping” inside the base materials, defects, and disorder can change the electrical conductivity in a wide range of values. In terms of electrical conductivity, graphene fillers are similar to metal fillers, although

extremely thin ones. The EM absorption of graphene is known to have a peak at 4.62 eV related to the many-body interactions, *i.e.*, excitons [139]. However, in the context of THz absorption in composites, more important is the high aspect ratio of the fillers, their size, and distributed nature of the scatterers.

A recent study proposed a physical model based on the Maxwell-Garnett theory for the complex dielectric permittivity of composites [100]. The model was written in terms of the polarizability of inclusions, suitable for nanoscale carbon fillers. The agglomerates and connected fillers were considered as structures with a higher aspect ratio and lower effective conductivity. The effective conductivity decreases due to the presence of contact resistances between the fillers. The model was tested on polylactic acid composites with graphite nanoplates [100]. The model predicts a peak in the absorption in the relevant frequency range, from high-GHz to several THz, depending on the main parameters – aspect ratio, size, and electrical conductivity of the fillers. Our experimental results are in line with this Maxwell-Garnett-based model, and the absorption spectra can be reproduced by fitting the aspect ratio and electrical conductivity of the fillers within a reasonable range.

Another phenomenon that may affect the EM energy absorption in dilute graphene composites is the filler–matrix interaction. It was recently reported that polyethylene with graphite particles (2.5 wt. % loading) reveals a strong attenuation, *i.e.*, absorption, peak at ~2.2 THz [126]. The authors attributed this attenuation peak to graphite particles' interaction with the matrix or the presence of impurities in the sample. At higher frequencies, there was a monotonic growth of the attenuation with frequency increase,

which was explained by the Rayleigh scattering. The absorption mechanism related to graphene–matrix interaction was proposed in another study focused on the absorptive properties of graphene composites in the near-THz frequency range. They were explained by the activation of the interaction of atomic vibrations of polymer matrix with the π-band to polaron band transitions in graphene in the THz frequency range [140,141]. This transition, which is in resonance with THz radiation, can cause strong absorptive properties, yielding a significant THz-range EMI shielding behavior [140].

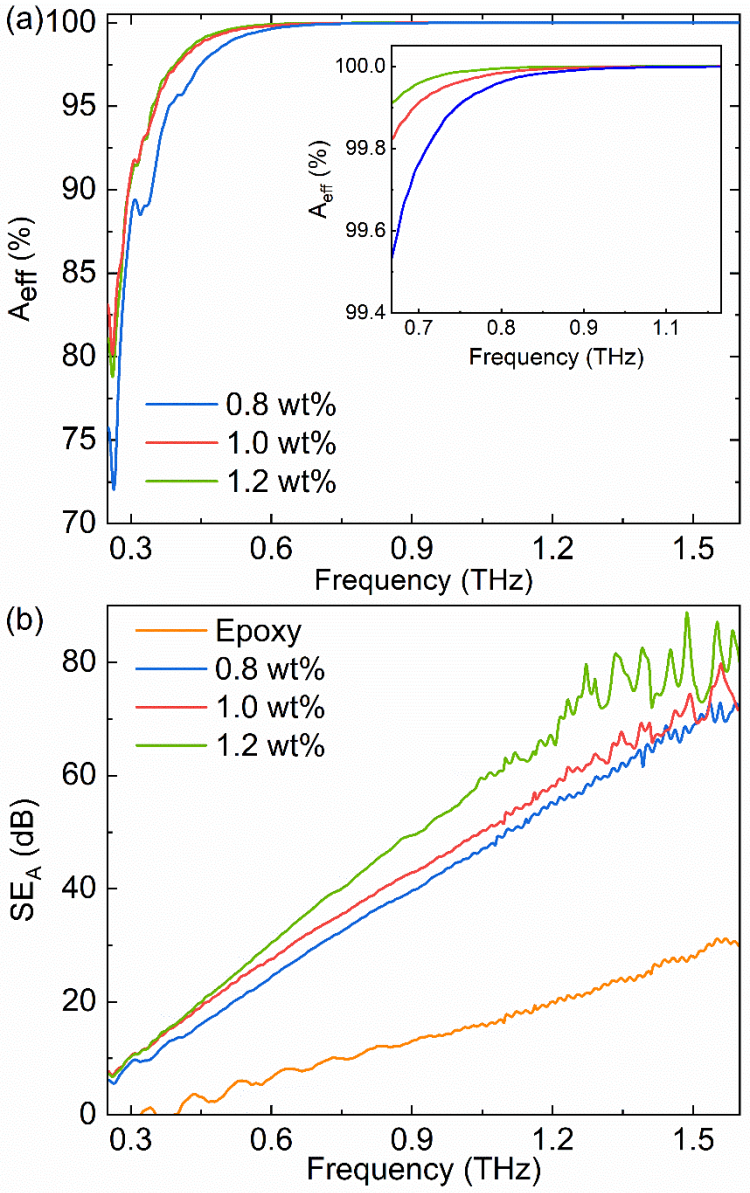

Figure 4-6: (a) Effective absorption coefficient, A_{eff}, of the epoxy composites with graphene as a function of frequency. The inset in (a) shows the same graph in the frequency range of 0.6 $THz \leq f \leq$ 1.2 THz. Note that at frequencies $f \geq$ 0.95 THz, the effective absorption reaches ~100%, indicating that the remaining fraction of the incident EM waves after reflection at the interface is completely absorbed by the composites. (b) Frequency-dependent shielding effectiveness of the composites by the absorption, SE_A. Reprinted with permission from Barani et al., Applied Physics Letters. 120 (2022) 063104. Copyright © 2022 AIP Publishing.

There is an additional interesting observation, which can be made from data presented in **Figure 4-5** and **Figure 4-6**. The slopes and the values of the transmission coefficient, *T*, and the shielding effectiveness, SE_T, are nearly the same for the composites containing 1.0 wt. % and 1.2 wt. % graphene at the frequencies below $f = 0.4$ THz (see **Figure 4-5**). On the other hand, the slopes of SE_T curves corresponding to the samples containing 1.0 wt. % and 0.8 wt. % of graphene are the same for the frequencies $f > 0.4$ THz. There is a change in the slope, specifically for the dilute composite with 1.0 wt. % of graphene, which happens at *f*=0.4 THz. A similar trend can be observed for the curves representing the shielding effectiveness related to the absorption, SE_A (see **Figure 4-6**). The slope of the SE_A curve is typically a good estimate of the high-frequency resistivity component of composite material, ρ [25,33]. We speculate that in this dilute composite, the displacement current, J_D, between graphene fillers separated by an insulating epoxy becomes significant, resulting in the changed characteristics. Since the displacement current density increases with frequency, this assumption should be valid for our electrically insulating samples. To facilitate the use of our experimental data for comparison with other materials, in **Figure 4-7** (a-b), we present the complex index of refraction, $n+i\kappa$, of our samples. The real and imaginary components, n and κ, were calculated from the magnitude and phase of the scattering parameters, S_{ij}, obtained in the TDS measurements.

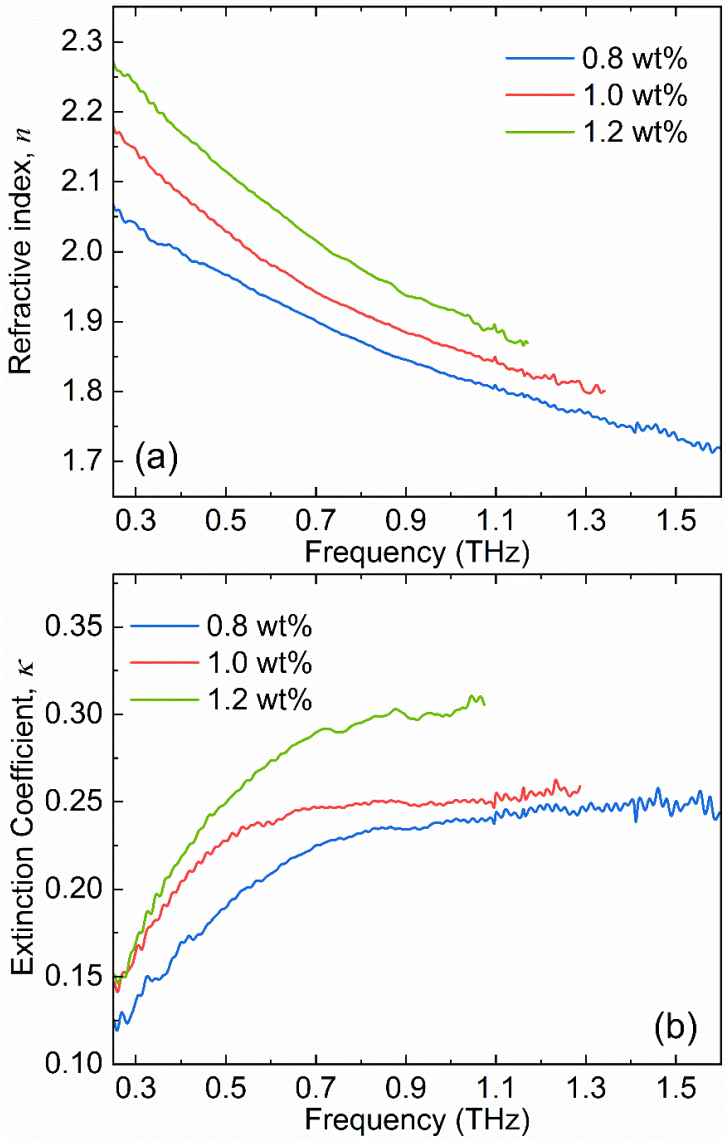

Figure 4-7: The complex index of refraction of the dilute graphene composites: (a) index of refraction, *n*, and (b) extinction coefficient, *κ*. Reprinted with permission from Barani et al., Applied Physics Letters. 120 (2022) 063104. Copyright © 2022 AIP Publishing.

We now turn to the applied aspect of the obtained results. The THz absorption shielding characteristics of the dilute graphene composites surpass most conventional polymeric composites with high loading of ceramic fillers, such as $BaTiO_3$ or Mxenes [142]. Ceramic fillers are usually used in composites to enhance the absorption component of total

shielding. The demonstrated electrically insulating composites can be used as adhesives and environment protective layers for electronic components without shortening them. Such graphene composite absorbers with small thicknesses can be deposited as a protective paint, *e.g.*, spray coatings. Shielding by absorption is crucial in many applications where the EM reflection is undesired. The dilute graphene composites have other advantages compared to various materials recently tested for THz shielding applications [143]. Alternative THz shielding materials include polyacrylonitrile - $Ti_3C_2T_x$ MXene - silver nanoparticle fiber membranes with different silver nanoparticle contents and thickness of porous structures. The reported shielding effectiveness of such fiber membranes with silver nanoparticles reaches up to 12 dB in the 0.2 THz – 1.6 THz range [143]. Another study reported the THz shielding performance of the few-layer borophene [144]. The maximum THz shielding effectiveness of borophene-based materials reached up to 50 and 21.5 dB for the reflection loss value in the examined frequency range from 0.1 THz to 2.7 THz. Most of the shielding reported in Ref [144] was achieved *via* reflection. Our dilute graphene composites have the benefit of being prepared from the "generic" graphene without surface functionalization or complicated processing steps. Graphene can be mass-produced *via* liquid-phase exfoliation (LPE) or graphene oxide (GO) reduction process [145–147]. Such graphene fillers are inherently better than metals owing to their low cost, absence of corrosion, and high aspect ratio allowing for higher THz absorption.

In this work, the EMI shielding was demonstrated for low power levels. The question of the dissipation of high-power THz energy is an interesting separate problem. Since energy

is transferred to heat, there is a limit to the dissipated power because epoxy can withstand a maximum of 150 C – 200 C. For the majority of applications, *e.g.*, communication, and security screening, which deal with small radiation power, the heating of the composite is negligible. If one needs to handle high-power levels, one would need composites with higher loading of graphene. Graphene and FLG have exceptionally high intrinsic thermal conductivity, which can become important if higher graphene loading layers are used together with the electrically insulating dilute graphene layers [30,32,148,149]. In addition to EMI shielding, high-loading graphene composites can dissipate the heat well [30,32,33,148]. Some of us have previously reported the thermal conductivity of epoxy composites with graphene and copper nanoparticles close to 15 W/mK [149].

4.5 Summary and Conclusions

In conclusions, we have demonstrated that dilute graphene composites with the low loading of graphene, below 1.2 wt. %, are efficient as electromagnetic absorbers in the THz frequency range. The THz radiation is mostly blocked by absorption rather than reflection. This is different from many other materials and composites used for EMI shielding, where reflection is the dominant mechanism for blocking EM waves. The efficiency of the THz radiation shielding by the lightweight, electrically insulating composites increases with increasing frequency. We argue that even the thin-film or spray coatings of graphene composites with a thickness in the few-hundred-micrometer range can be sufficient for

blocking THz radiation in many practical applications. The described graphene composites can be considered complementary to composites with quasi-1D van der Waals fillers.

References

[1] Z. Barani, F. Kargar, Y. Ghafouri, S. Ghosh, K. Godziszewski, S. Baraghani, Y. Yashchyshyn, G. Cywiński, S. Rumyantsev, T.T. Salguero, A.A. Balandin, Electrically Insulating Flexible Films with Quasi-1D van der Waals Fillers as Efficient Electromagnetic Shields in the GHz and Sub-THz Frequency Bands, Advanced Materials. 33 (2021) 2007286. https://doi.org/10.1002/adma.202007286.

[2] Z. Barani, F. Kargar, Y. Ghafouri, S. Baraghani, S. Sudhindra, A. Mohammadzadeh, T.T. Salguero, A.A. Balandin, Electromagnetic-Polarization-Selective Composites with Quasi-1D van der Waals Fillers: Nanoscale Material Functionality That Mimics Macroscopic Systems, ACS Appl Mater Interfaces. 13 (2021) 21527–21533. https://doi.org/10.1021/acsami.1c03204.

[3] Z. Barani, K. Stelmaszczyk, F. Kargar, Y. Yashchyshyn, G. Cywiński, S. Rumyantsev, A.A. Balandin, Efficient Terahertz Radiation Absorption by Dilute Graphene Composites, Appl Phys Lett. 120 (2022) 063104. https://doi.org/10.1063/5.0079891.

[4] Y. Zhang, Y.-W. Tan, H.L. Stormer, P. Kim, Experimental Observation of the Quantum Hall Effect and Berry's Phase in Graphene, Nature. 438 (2005) 201–204. https://doi.org/10.1038/nature04235.

[5] A.A. Balandin, Low-Frequency 1/f Noise in Graphene Devices, Nat Nano. 8 (2013) 549–555.

[6] A.K. Geim, I. v. Grigorieva, Van der Waals Heterostructures, Nature. 499 (2013) 419–425. https://doi.org/10.1038/nature12385.

[7] K.S. Novoselov, A.K. Geim, S. v Morozov, D. Jiang, Y. Zhang, S. v Dubonos, I. v Grigorieva, A.A. Firsov, Electric Field Effect in Atomically Thin Carbon Films, Science 306 (2004) 666–9. https://doi.org/10.1126/science.1102896.

[8] A.A. Balandin, Thermal Properties of Graphene and Nanostructured Carbon Materials, Nat Mater. 10 (2011) 569–581. https://doi.org/10.1038/nmat3064.

[9] M.A. Bloodgood, P. Wei, E. Aytan, K.N. Bozhilov, A.A. Balandin, T.T. Salguero, Monoclinic Structures of Niobium Trisulfide, APL Mater. 6 (2018) 026602. https://doi.org/10.1063/1.5005813.

[10] X. Liu, J. Liu, L.Y. Antipina, J. Hu, C. Yue, A.M. Sanchez, P.B. Sorokin, Z. Mao, J. Wei, Direct Fabrication of Functional Ultrathin Single-Crystal Nanowires from Quasi-One-Dimensional van der Waals Crystals, Nano Lett. 16 (2016) 6188–6195. https://doi.org/10.1021/acs.nanolett.6b02453.

[11] H. Yi, T. Komesu, S. Gilbert, G. Hao, A.J. Yost, A. Lipatov, A. Sinitskii, J. Avila, C. Chen, M.C. Asensio, P.A. Dowben, The Band Structure of The Quasi-One-Dimensional Layered Semiconductor TiS_3(001), Appl Phys Lett. 112 (2018) 052102. https://doi.org/10.1063/1.5020054.

[12] M.A. Stolyarov, G. Liu, M.A. Bloodgood, E. Aytan, C. Jiang, R. Samnakay, T.T. Salguero, D.L. Nika, S.L. Rumyantsev, M.S. Shur, K.N. Bozhilov, A.A. Balandin, Breakdown Current Density in h-BN-Capped Quasi-1D $TaSe_3$ Metallic Nanowires: Prospects of Interconnect Applications, Nanoscale. 8 (2016) 15774–15782. https://doi.org/10.1039/c6nr03469a.

[13] A. Geremew, M.A. Bloodgood, E. Aytan, B.W.K. Woo, S.R. Corber, G. Liu, K. Bozhilov, T.T. Salguero, S. Rumyantsev, M.P. Rao, A.A. Balandin, Current Carrying Capacity of Quasi-1D $ZrTe_3$ van Der Waals Nanoribbons, IEEE Electron Device Letters. 39 (2018) 735–738. https://doi.org/10.1109/LED.2018.2820140.

[14] T.A. Empante, A. Martinez, M. Wurch, Y. Zhu, A.K. Geremew, K. Yamaguchi, M. Isarraraz, S. Rumyantsev, E.J. Reed, A.A. Balandin, L. Bartels, Low Resistivity and High Breakdown Current Density of 10 nm Diameter van der Waals $TaSe_3$ Nanowires by Chemical Vapor Deposition, Nano Lett. 19 (2019) 4355–4361. https://doi.org/10.1021/acs.nanolett.9b00958.

[15] A. Lipatov, M.J. Loes, H. Lu, J. Dai, P. Patoka, N.S. Vorobeva, D.S. Muratov, G. Ulrich, B. Kästner, A. Hoehl, G. Ulm, X.C. Zeng, E. Rühl, A. Gruverman, P.A. Dowben, A. Sinitskii, Quasi-1D TiS_3 Nanoribbons: Mechanical Exfoliation and Thickness-Dependent Raman Spectroscopy, ACS Nano. 12 (2018) 12713–12720. https://doi.org/10.1021/acsnano.8b07703.

[16] G. Cheon, K.-A.N. Duerloo, A.D. Sendek, C. Porter, Y. Chen, E.J. Reed, Data Mining for New Two- and One-Dimensional Weakly Bonded Solids and Lattice-Commensurate Heterostructures, Nano Lett. 17 (2017) 1915–1923. https://doi.org/10.1021/acs.nanolett.6b05229.

[17] A.K. Geremew, S. Rumyantsev, M.A. Bloodgood, T.T. Salguero, A.A. Balandin, Unique Features of the Generation–Recombination Noise in Quasi-One-Dimensional van der Waals Nanoribbons, Nanoscale. 10 (2018) 19749–19756. https://doi.org/10.1039/C8NR06984K.

[18] S. Nagata, S. Ebisu, T. Aochi, Y. Kinoshita, S. Chikazawa, K. Yamaya, Superconductivity in the Filamentary Conductor $TaSe_3$, Journal of Physics and Chemistry of Solids. 52 (1991) 761–767. https://doi.org/10.1016/0022-3697(91)90074-A.

[19] B.J. Kim, B.J. Jeong, S. Oh, S. Chae, K.H. Choi, T. Nasir, S.H. Lee, H.K. Lim, I.J. Choi, M.-K. Hong, H.K. Yu, J.-H. Lee, J.-Y. Choi, Thickness-Dependence Electrical

Characterization of the One-Dimensional van der Waals $TaSe_3$ Crystal, Materials. 12 (2019) 2462. https://doi.org/10.3390/ma12152462.

[20] A.I.U. Saleheen, R. Chapai, L. Xing, R. Nepal, D. Gong, X. Gui, W. Xie, D.P. Young, E.W. Plummer, R. Jin, Evidence for Topological Semimetallicity in a Chain-Compound $TaSe_3$, NPJ Quantum Mater. 5 (2020) 1–8. https://doi.org/10.1038/s41535-020-00257-7.

[21] J. Yang, Y.Q. Wang, R.R. Zhang, L. Ma, W. Liu, Z. Qu, L. Zhang, S.L. Zhang, W. Tong, L. Pi, W.K. Zhu, C.J. Zhang, Observation of Charge Density Wave Transition in $TaSe_3$ Mesowires, Appl Phys Lett. 115 (2019) 033102. https://doi.org/10.1063/1.5099110.

[22] J.P. Gogoi, A. Shabir, High-Temperature Electromagnetic Interference Shielding Materials, in: Materials for Potential EMI Shielding Applications, Elsevier, 2020: pp. 379–390. https://doi.org/10.1016/B978-0-12-817590-3.00023-3.

[23] F. Shahzad, M. Alhabeb, C.B. Hatter, B. Anasori, S. Man Hong, C.M. Koo, Y. Gogotsi, Electromagnetic Interference Shielding with 2D Transition Metal Carbides (MXenes), Science 353 (2016) 1137–1140.

[24] D. Jiang, V. Murugadoss, Y. Wang, J. Lin, T. Ding, Z. Wang, Q. Shao, C. Wang, H. Liu, N. Lu, R. Wei, A. Subramania, Z. Guo, Electromagnetic Interference Shielding Polymers and Nanocomposites - A Review, Polymer Reviews. 59 (2019) 280–337. https://doi.org/10.1080/15583724.2018.1546737.

[25] R.M. Simon, EMI Shielding Through Conductive Plastics, Polym Plast Technol Eng. 17 (1981) 1–10. https://doi.org/10.1080/03602558108067695.

[26] D.D.L. Chung, Electromagnetic Interference Shielding Effectiveness of Carbon Materials, Carbon 39 (2001) 279–285. https://doi.org/10.1016/S0008-6223(00)00184-6.

[27] Z. Chen, C. Xu, C. Ma, W. Ren, H.-M. Cheng, Lightweight and Flexible Graphene Foam Composites for High-Performance Electromagnetic Interference Shielding, Advanced Materials. 25 (2013) 1296–1300. https://doi.org/10.1002/adma.201204196.

[28] N. Yousefi, X. Sun, X. Lin, X. Shen, J. Jia, B. Zhang, B. Tang, M. Chan, J.-K. Kim, Highly Aligned Graphene/Polymer Nanocomposites with Excellent Dielectric Properties for High-Performance Electromagnetic Interference Shielding, Advanced Materials. 26 (2014) 5480–5487. https://doi.org/10.1002/adma.201305293.

[29] B. Shen, W. Zhai, W. Zheng, Ultrathin Flexible Graphene Film: An Excellent Thermal Conducting Material with Efficient EMI Shielding, Adv Funct Mater. 24 (2014) 4542–4548. https://doi.org/10.1002/adfm.201400079.

[30] F. Kargar, Z. Barani, M. Balinskiy, A.S. Magana, J.S. Lewis, A.A. Balandin, Dual-Functional Graphene Composites for Electromagnetic Shielding and Thermal Management, Adv Electron Mater. 5 (2019) 1800558. https://doi.org/10.1002/aelm.201800558.

[31] D.-X. Yan, H. Pang, B. Li, R. Vajtai, L. Xu, P.-G. Ren, J.-H. Wang, Z.-M. Li, Structured Reduced Graphene Oxide/Polymer Composites for Ultra-Efficient Electromagnetic Interference Shielding, Adv Funct Mater. 25 (2015) 559–566. https://doi.org/10.1002/adfm.201403809.

[32] Z. Barani, F. Kargar, A. Mohammadzadeh, S. Naghibi, C. Lo, B. Rivera, A.A. Balandin, Multifunctional Graphene Composites for Electromagnetic Shielding and Thermal Management at Elevated Temperatures, Adv Electron Mater. 6 (2020) 2000520. https://doi.org/10.1002/aelm.202000520.

[33] Z. Barani, F. Kargar, K. Godziszewski, A. Rehman, Y. Yashchyshyn, S. Rumyantsev, G. Cywiński, W. Knap, A.A. Balandin, Graphene Epoxy-Based Composites as Efficient Electromagnetic Absorbers in the Extremely High-Frequency Band, ACS Appl Mater Interfaces. 12 (2020) 28635–28644. https://doi.org/10.1021/acsami.0c06729.

[34] S. Nie, L. Xing, R. Jin, W. Xie, Z. Wang, F.B. Prinz, Topological Phases in the $TaSe_3$ Compound, Phys Rev B. 98 (2018) 125143. https://doi.org/10.1103/PhysRevB.98.125143.

[35] W. Xia, X. Shi, Y. Zhang, H. Su, Q. Wang, L. Ding, L. Chen, X. Wang, Z. Zou, N. Yu, L. Pi, Y. Hao, B. Li, Z. Zhu, W. Zhao, X. Kou, Y. Guo, Bulk Fermi Surface of the Layered Superconductor $TaSe_3$ with Three-Dimensional Strong Topological State, Phys Rev B. 101 (2020) 155117. https://doi.org/10.1103/PhysRevB.101.155117.

[36] Y. Zhang, T. Zhu, H. Bu, Z. Cai, C. Xi, B. Chen, B. Wei, D. Lin, H. Xie, M. Naveed, X. Xi, F. Fei, H. Zhang, F. Song, Large Magnetoresistance in Topological Insulator Candidate $TaSe_3$, AIP Adv. 10 (2020) 095314. https://doi.org/10.1063/5.0015490.

[37] J.Á. Silva-Guillén, E. Canadell, Strain Control of the Competition between Metallic and Semiconducting States in Single-Layers of $TaSe_3$, 2D Mater. 7 (2020) 025038. https://doi.org/10.1088/2053-1583/ab72d9.

[38] G. Liu, S. Rumyantsev, M.A. Bloodgood, T.T. Salguero, M. Shur, A.A. Balandin, Low-Frequency Electronic Noise in Quasi-1D $TaSe_3$ van der Waals Nanowires, Nano Lett. 17 (2017) 377–383. https://doi.org/10.1021/acs.nanolett.6b04334.

[39] E. Bjerkelund, A. Kjekshus, On the Properties of TaS_3, $TaSe_3$ and $TaTe_4$, ZAAC - Journal of Inorganic and General Chemistry. 328 (1964) 235–242. https://doi.org/10.1002/zaac.19643280506.

[40] M. Zdrojek, J. Bomba, A. Lapińska, A. Dużyńska, K. Żerańska-Chudek, J. Suszek, L. Stobiński, A. Taube, M. Sypek, J. Judek, Graphene-Based Plastic Absorber for Total Sub-Terahertz Radiation Shielding, Nanoscale. 10 (2018) 13426–13431. https://doi.org/10.1039/c8nr02793e.

[41] M. Naftaly, Metrology Issues and Solutions in THz Time-Domain Spectroscopy: Noise, Errors, Calibration, IEEE Sens J. 13 (2012) 8–17. https://doi.org/10.1109/jsen.2012.2208624.

[42] Y. Yashchyshyn, K. Godziszewski, A New Method for Dielectric Characterization in Sub-THz Frequency Range, IEEE Trans Terahertz Sci Technol. 8 (2018) 19–26. https://doi.org/10.1109/TTHZ.2017.2771309.

[43] N. Dvurechenskaya, P.R. Bajurko, R.J. Zieliński, Y. Yashchyshyn, Measurements of Shielding Effectiveness of Textile Materials Containing Metal by the Free-Space Transmission Technique with Data Processing in the Time Domain, Metrol. Meas. Syst. 21 (2013) 217–228. https://doi.org/10.2478/mms-2013-0019.

[44] K. Godziszewski, Y. Yashchyshyn, Investigation of Influence of Measurement Conditions on Accuracy of Material Characterization in Sub-THz Frequency Range, in: 2016 21st International Conference on Microwave, Radar and Wireless Communications, MIKON 2016, Institute of Electrical and Electronics Engineers Inc., 2016. https://doi.org/10.1109/MIKON.2016.7491939.

[45] Q. Wei, S. Pei, X. Qian, H. Liu, Z. Liu, W. Zhang, T. Zhou, Z. Zhang, X. Zhang, H. Cheng, W. Ren, Superhigh Electromagnetic Interference Shielding of Ultrathin Aligned Pristine Graphene Nanosheets Film, Advanced Materials. 32 (2020) 1907411. https://doi.org/10.1002/adma.201907411.

[46] X. Shui, D.D.L. Chung, Nickel Filament Polymer-Matrix Composites with Low Surface Impedance and High Electromagnetic Interference Shielding Effectiveness, J Electron Mater. 26 (1997) 928–934. https://doi.org/10.1007/s11664-997-0276-4.

[47] M.H. Al-Saleh, U. Sundararaj, Electromagnetic Interference Shielding Mechanisms of CNT/Polymer Composites, Carbon 47 (2009) 1738–1746. https://doi.org/10.1016/J.CARBON.2009.02.030.

[48] N. Agnihotri, K. Chakrabarti, A. De, Highly Efficient Electromagnetic Interference Shielding Using Graphite Nanoplatelet/Poly(3,4-ethylenedioxythiophene)-Poly(styrenesulfonate) Composites with Enhanced Thermal Conductivity, RSC Adv. 5 (2015) 43765–43771. https://doi.org/10.1039/c4ra15674a.

[49] C. Liang, K. Ruan, Y. Zhang, J. Gu, Multifunctional Flexible Electromagnetic Interference Shielding Silver Nanowires/Cellulose Films with Excellent Thermal

Management and Joule Heating Performances, ACS Appl Mater Interfaces. 12 (2020) 18023–18031. https://doi.org/10.1021/acsami.0c04482.

[50] S. Pande, B. Singh, R. Mathur, T. Dhami, P. Saini, S. Dhawan, Improved Electromagnetic Interference Shielding Properties of MWCNT-PMMA Composites Using Layered Structures., Nanoscale Res Lett. 4 (2009) 327–34. https://doi.org/10.1007/s11671-008-9246-x.

[51] M. Arjmand, A.A. Moud, Y. Li, U. Sundararaj, Outstanding Electromagnetic Interference Shielding of Silver Nanowires: Comparison with Carbon Nanotubes, RSC Adv. 5 (2015) 56590–56598. https://doi.org/10.1039/C5RA08118A.

[52] P. Ghosh, A. Chakrabarti, Conducting Carbon Black Filled EPDM Vulcanizates: Assessment of Dependence of Physical and Mechanical Properties and Conducting Character on Variation of Filler Loading, Eur Polym J. 36 (2000) 1043–1054. https://doi.org/10.1016/S0014-3057(99)00157-3.

[53] A.P. Singh, P. Garg, F. Alam, K. Singh, R.B. Mathur, R.P. Tandon, A. Chandra, S.K. Dhawan, Phenolic Resin-Based Composite Sheets Filled with Mixtures of Reduced Graphene Oxide, γ-Fe_2O_3 and Carbon Fibers for Excellent Electromagnetic Interference Shielding in the X-band, Carbon 50 (2012) 3868–3875. https://doi.org/10.1016/j.carbon.2012.04.030.

[54] A. Celzard, J.F. Marêché, F. Payot, Simple Method for Characterizing Synthetic Graphite Powders, J Phys D Appl Phys. 33 (2000) 1556–1563. https://doi.org/10.1088/0022-3727/33/12/318.

[55] C.L. Huang, Y.J. Wang, Y.C. Fan, C.L. Hung, Y.C. Liu, The Effect of Geometric Factor of Carbon Nanofillers on the Electrical Conductivity and Electromagnetic Interference Shielding Properties of Poly(trimethylene terephthalate) Composites: A Comparative Study, J Mater Sci. 52 (2017) 2560–2580. https://doi.org/10.1007/s10853-016-0549-5.

[56] X. Xia, Y. Wang, Z. Zhong, G.J. Weng, A Theory of Electrical Conductivity, Dielectric Constant, and Electromagnetic Interference Shielding for Lightweight Graphene Composite Foams, J Appl Phys. 120 (2016) 085102. https://doi.org/10.1063/1.4961401.

[57] R. Ram, D. Khastgir, M. Rahaman, Electromagnetic Interference Shielding Effectiveness and Skin Depth of Poly(vinylidene fluoride)/Particulate Nano-Carbon Filler Composites: Prediction of Electrical Conductivity and Percolation Threshold, Polym Int. 68 (2019) 1194–1203. https://doi.org/10.1002/pi.5812.

[58] Y. Pan, G.J. Weng, S.A. Meguid, W.S. Bao, Z.H. Zhu, A.M.S. Hamouda, Percolation Threshold and Electrical Conductivity of a Two-Phase Composite Containing

Randomly Oriented Ellipsoidal Inclusions, J Appl Phys. 110 (2011) 123715. https://doi.org/10.1063/1.3671675.

[59] T. Sambongi, M. Yamamoto, K. Tsutsumi, Y. Shiozaki, K. Yamaya, Y. Abe, Superconductivity in One-Dimensional $TaSe_3$, J Physical Soc Japan. 42 (1977) 1421–1422. https://doi.org/10.1143/JPSJ.42.1421.

[60] E. Bjerkelund, J.H. Fermor, A. Kjekshus, The Properties of TaS_3 and $TaSe_3$, Acta Chem Scand. 20 (1966) 1836–1842.

[61] T. Sambongi, M. Ido, K. Tsutsumi, M. Yamamoto, T. Takoshima, Y. Abe, Phase Transitions and Electric Properties of MX_3, in: S. Barišić, A. Bjeliš, J.R. Cooper, B.A. Leontić (Eds.), Quasi One-Dimensional Conductors I. Lecture Notes in Physics, Springer, 1979: pp. 349–353.

[62] P. Haen, P. Monceau, B. Tissier, G. Waysand, A. Meerschaut, P. Molinie, J. Rouxel, Comparison Between Electrical Conductivity of Multilayered $NbSe_2$ and $TaSe_2$ and Filamentary Compounds $NbSe_3$ and $TaSe_3$, Ferroelectrics. 17 (1977) 447–449. https://doi.org/10.1080/00150197708236765.

[63] H.P. Geserich, G. Scheiber, F. Lévy, P. Monceau, Electrical Anisotropy of The Chain-Like Conductors $NbSe_3$ and $TaSe_3$, Physica B+C. 143 (1986) 174–176. https://doi.org/10.1016/0378-4363(86)90085-9.

[64] T.M. Tritt, R.L. Jacobsen, A.C. Ehrlich, D.J. Gillespie, Measure of the Elastic and Transport Properties of $TaSe_3$ Through the Stress-Induced Phase Transition, Physica B: Physics of Condensed Matter. 194–196 (1994) 1303–1304. https://doi.org/10.1016/0921-4526(94)90981-4.

[65] S. Kikkawa, K. Shinya, M. Koizumi, The Selenide Systems of Niobium and Tantalum, J Solid State Chem. 41 (1982) 323–328. https://doi.org/10.1016/0022-4596(82)90152-9.

[66] T.M. Tritt, E.P. Stillwell, M.J. Skove, Effect of Uniaxial Stress on the Transport Properties of $TaSe_3$, Phys Rev B. 34 (1986) 6799–6803. https://doi.org/10.1080/01411594.2016.1198963.

[67] G. Kumagai, T. Matsuura, K. Ichimura, S. Tanda, Cylinder Vortex of Superconductor in $TaSe_3$ Topological Ring Crystals, in: J Phys Conf Ser, Institute of Physics Publishing, 2009: p. 052134. https://doi.org/10.1088/1742-6596/150/5/052134.

[68] S. Kikkawa, N. Ogawa, M. Koizumi, Y. Onuki, High-Pressure Syntheses of TaS_3, NbS_3, $TaSe_3$, and $NbSe_3$ with $NbSe_3$-Type Crystal Structure, J Solid State Chem. 41 (1982) 315–322. https://doi.org/10.1016/0022-4596(82)90151-7.

[69] K. Yamaya, Y. Abe, Electrical Properties oF $Ta(S_xSe_{1-x})_3$, in: Molecular Crystals and Liquid Crystals, Taylor & Francis Group , 1982: pp. 133–140. https://doi.org/10.1080/00268948208072559.

[70] J. Gill, Dislocations and the Motion of Weakly Pinned Charge-Density Waves: Experiments on Niobium Triselenide Containing Mobile Indium Impurities, Phys Rev B Condens Matter Mater Phys. 53 (1996) 15586–15603. https://doi.org/10.1103/PhysRevB.53.15586.

[71] A. V. Zavalko, S. V. Zaitsev-Zotov, Impurity-Induced Metal-Insulator Transition in Quasi-One-Dimensional Metals $TaSe_3$ and $NbSe_3$, Journal de Physique IV (Proceedings). 131 (2005) 359–360. https://doi.org/10.1051/jp4:2005131093.

[72] A. Nomura, K. Yamaya, S. Takayanagi, K. Ichimura, S. Tanda, Effect of Cu Doping on Superconductivity in $TaSe_3$: Relationship between Superconductivity and Induced Charge Density Wave, EPL. 124 (2018) 67001. https://doi.org/10.1209/0295-5075/124/67001.

[73] A.R. Parker, H.E. Townley, Biomimetics of Photonic Nanostructures, Nat Nanotechnol. 2 (2007) 347–353. https://doi.org/10.1038/nnano.2007.152.

[74] Y. Li, J. John, K.W. Kolewe, J.D. Schiffman, K.R. Carter, Scaling Up Nature: Large Area Flexible Biomimetic Surfaces, ACS Appl Mater Interfaces. 7 (2015) 23439–23444. https://doi.org/10.1021/acsami.5b04957.

[75] T.A. Milligan, Modern Antenna Design, John Wiley & Sons, 2005.

[76] J.O. Island, A.J. Molina-Mendoza, M. Barawi, R. Biele, E. Flores, J.M. Clamagirand, J.R. Ares, C. Sánchez, H.S.J. Van Der Zant, R. D'Agosta, I.J. Ferrer, A. Castellanos-Gomez, Electronics and Optoelectronics of Quasi-1D Layered Transition Metal Trichalcogenides, 2D Mater. 4 (2017) 022003. https://doi.org/10.1088/2053-1583/aa6ca6.

[77] A. Patra, C.S. Rout, Anisotropic Quasi-One-Dimensional Layered Transition-Metal Trichalcogenides: Synthesis, Properties and Applications, RSC Adv. 10 (2020) 36413–36438. https://doi.org/10.1039/d0ra07160a.

[78] J. Dai, M. Li, X.C. Zeng, Group IVB Transition Metal Trichalcogenides: A New Class of 2D Layered Materials Beyond Graphene, Wiley Interdiscip Rev Comput Mol Sci. 6 (2016) 211–222. https://doi.org/10.1002/wcms.1243.

[79] G. Cheon, E.D. Cubuk, E.R. Antoniuk, L. Blumberg, J.E. Goldberger, E.J. Reed, Revealing the Spectrum of Unknown Layered Materials with Superhuman Predictive

Abilities, Journal of Physical Chemistry Letters. 9 (2018) 6967–6972. https://doi.org/10.1021/acs.jpclett.8b03187.

[80] Y. Saeed, A. Kachmar, M.A. Carignano, First-Principles Study of The Transport Properties in Bulk and Monolayer MX_3 (M = Ti, Zr, Hf and X = S, Se) Compounds, Journal of Physical Chemistry C. 121 (2017) 1399–1403. https://doi.org/10.1021/acs.jpcc.6b08067.

[81] J. Lienig, Electromigration and Its Impact on Physical Design in Future Technologies, in: Proceedings of the International Symposium on Physical Design, 2013: pp. 33–40. https://doi.org/10.1145/2451916.2451925.

[82] J.P. Gambino, T.C. Lee, F. Chen, T.D. Sullivan, Reliability Challenges for Advanced Copper Interconnects: Electromigration and Time-Dependent Dielectric Breakdown (TDDB), in: Proceedings of the International Symposium on the Physical and Failure Analysis of Integrated Circuits, IPFA, APS, 2009: pp. 677–684. https://doi.org/10.1109/IPFA.2009.5232553.

[83] V. Nicolosi, M. Chhowalla, M.G. Kanatzidis, M.S. Strano, J.N. Coleman, Liquid Exfoliation of Layered Materials, Science 340 (2013) 1226419–1226419. https://doi.org/10.1126/science.1226419.

[84] D. Doganay, S. Coskun, C. Kaynak, H.E. Unalan, Electrical, Mechanical and Thermal Properties of Aligned Silver Nanowire/Polylactide Nanocomposite Films, Compos B Eng. 99 (2016) 288–296. https://doi.org/10.1016/j.compositesb.2016.06.044.

[85] T. Hu, Y. Song, J. Di, D. Xie, C. Teng, Highly Thermally Conductive Layered Polymer Composite from Solvent-Exfoliated Pristine Graphene, Carbon 140 (2018) 596–602. https://doi.org/10.1016/j.carbon.2018.09.026.

[86] K. Kim, J. Hong, S.G. Hahm, Y. Rho, T.K. An, S.H. Kim, C.E. Park, Facile and Microcontrolled Blade Coating of Organic Semiconductor Blends for Uniaxial Crystal Alignment and Reliable Flexible Organic Field-Effect Transistors, ACS Appl Mater Interfaces. 11 (2019) 13481–13490. https://doi.org/10.1021/acsami.8b21130.

[87] J. Baker-Jarvis, M.D. Janezic, D.C. Degroot, High-Frequency Dielectric Measurements, IEEE Instrum Meas Mag. 13 (2010) 24–31. https://doi.org/10.1109/MIM.2010.5438334.

[88] X.-H. Li, X. Li, K.-N. Liao, P. Min, T. Liu, A. Dasari, Z.-Z. Yu, Thermally Annealed Anisotropic Graphene Aerogels and Their Electrically Conductive Epoxy Composites with Excellent Electromagnetic Interference Shielding Efficiencies., ACS Appl Mater Interfaces. 8 (2016) 33230–33239. https://doi.org/10.1021/acsami.6b12295.

[89] M.N.O. Sadiku, Elements of Electromagnetics, Third, Oxford University Press, New York, Oxford, 2005.

[90] A. Sihvola, Mixing Rules with Complex Dielectric Coefficients, Subsurface Sensing Technologies and Applications. 1 (2000) 393–415. https://doi.org/10.1023/A:1026511515005.

[91] J.C.M. Garnett, XII. Colours in Metal Glasses and in Metallic Films, Philosophical Transactions of the Royal Society of London. Series A, Containing Papers of a Mathematical or Physical Character. 203 (1904) 385–420.

[92] A. Perucchi, C. Søndergaard, S. Mitrovic, M. Grioni, N. Barisic, H. Berger, L. Forró, L. Degiorg, Spectroscopic and DC-Transport Investigations of the Electronic Properties of $TaSe_3$, European Physical Journal B. 39 (2004) 433–440. https://doi.org/10.1140/epjb/e2004-00214-x.

[93] N. Papadopoulos, R. Frisenda, R. Biele, E. Flores, J.R. Ares, C. Sánchez, H.S.J. Van Der Zant, I.J. Ferrer, R. D'Agosta, A. Castellanos-Gomez, Large Birefringence and Linear Dichroism in TiS_3 Nanosheets, Nanoscale. 10 (2018) 12424–12429. https://doi.org/10.1039/c8nr03616k.

[94] S.J. Gilbert, H. Yi, J.S. Chen, A.J. Yost, A. Dhingra, J. Abourahma, A. Lipatov, J. Avila, T. Komesu, A. Sinitskii, M.C. Asensio, P.A. Dowben, Effect of Band Symmetry on Photocurrent Production in Quasi-One-Dimensional Transition-Metal Trichalcogenides, ACS Appl Mater Interfaces. 12 (2020) 40525–40531. https://doi.org/10.1021/acsami.0c11892.

[95] J.O. Island, R. Biele, M. Barawi, J.M. Clamagirand, J.R. Ares, C. Sánchez, H.S.J. Van Der Zant, I.J. Ferrer, R. D'Agosta, A. Castellanos-Gomez, Titanium Trisulfide (TiS_3): A 2D Semiconductor with Quasi-1D Optical and Electronic Properties, Sci Rep. 6 (2016) 22214. https://doi.org/10.1038/srep22214.

[96] M.A. Seo, J.H. Yim, Y.H. Ahn, F. Rotermund, D.S. Kim, S. Lee, H. Lim, Terahertz Electromagnetic Interference Shielding Using Single-Walled Carbon Nanotube Flexible Films, Appl Phys Lett. 93 (2008) 231905. https://doi.org/10.1063/1.3046126.

[97] F. Deruelle, The Different Sources of Electromagnetic Fields: Dangers Are Not Limited to Physical Health, Electromagn Biol Med. 39 (2020) 166–175. https://doi.org/10.1080/15368378.2020.1737811.

[98] R.N. Kostoff, P. Heroux, M. Aschner, A. Tsatsakis, Adverse Health Effects of 5G Mobile Networking Technology Under Real-Life Conditions, Toxicol Lett. 323 (2020) 35–40. https://doi.org/10.1016/j.toxlet.2020.01.020.

[99] J. Pan, H. Hu, Z. Li, J. Mu, Y. Cai, H. Zhu, Recent Progress in Two-Dimensional Materials for Terahertz Protection, Nanoscale Adv. 3 (2021) 1515–1531. https://doi.org/10.1039/D0NA01046D.

[100] D. Bychanok, P. Angelova, A. Paddubskaya, D. Meisak, L. Shashkova, M. Demidenko, A. Plyushch, E. Ivanov, R. Krastev, R. Kotsilkova, F.Y. Ogrin, P. Kuzhir, Terahertz Absorption in Graphite Nanoplatelets/Polylactic Acid Composites, J Phys D Appl Phys. 51 (2018) 145307. https://doi.org/10.1088/1361-6463/AAB1A5.

[101] G. Li, N. Amer, H.A. Hafez, S. Huang, D. Turchinovich, V.N. Mochalin, F.A. Hegmann, L. V. Titova, Dynamical Control over Terahertz Electromagnetic Interference Shielding with 2D Ti_3C_2Ty MXene by Ultrafast Optical Pulses, Nano Lett. (2019). https://doi.org/10.1021/acs.nanolett.9b04404.

[102] Z. Tu, Z. Ma, J. Li, J. Liang, S. Li, Y. Shi, L. Pan, Prospective on Doping Engineering of Conductive Polymers for Enhanced Interfacial Properties, Appl Phys Lett. 119 (2021) 150504. https://doi.org/10.1063/5.0062125.

[103] D. Wanasinghe, F. Aslani, G. Ma, D. Habibi, Review of Polymer Composites with Diverse Nanofillers for Electromagnetic Interference Shielding, Nanomaterials. 10 (2020) 541. https://doi.org/10.3390/nano10030541.

[104] J. Wu, Z. Ye, H. Ge, J. Chen, W. Liu, Z. Liu, Modified Carbon Fiber/Magnetic Graphene/Epoxy Composites with Synergistic Effect for Electromagnetic Interference Shielding over Broad Frequency Band, J Colloid Interface Sci. 506 (2017) 217–226. https://doi.org/10.1016/J.JCIS.2017.07.020.

[105] S. Mondal, S. Ganguly, P. Das, D. Khastgir, N.C. Das, Low Percolation Threshold and Electromagnetic Shielding Effectiveness of Nano-Structured Carbon Based Ethylene Methyl Acrylate Nanocomposites, Compos B Eng. 119 (2017) 41–56. https://doi.org/10.1016/J.COMPOSITESB.2017.03.022.

[106] S. Kuester, C. Merlini, G.M.O. Barra, J.C. Ferreira, A. Lucas, A.C. de Souza, B.G. Soares, Processing and Characterization of Conductive Composites Based on Poly(styrene-b-ethylene-ran-butylene-b-styrene) (SEBS) and Carbon Additives: A Comparative Study of Expanded Graphite and Carbon Black, Compos B Eng. 84 (2016) 236–247. https://doi.org/10.1016/J.COMPOSITESB.2015.09.001.

[107] G. De Bellis, A. Tamburrano, A. Dinescu, M.L. Santarelli, M.S. Sarto, Electromagnetic Properties of Composites Containing Graphite Nanoplatelets at Radio Frequency, Carbon 49 (2011) 4291–4300. https://doi.org/10.1016/J.CARBON.2011.06.008.

[108] X. Jiang, D.-X. Yan, Y. Bao, H. Pang, X. Ji, Z.-M. Li, Facile, Green and Affordable Strategy for Structuring Natural Graphite/Polymer Composite with Efficient Electromagnetic Interference Shielding, RSC Adv. 5 (2015) 22587–22592. https://doi.org/10.1039/C4RA11332B.

[109] S.H. Park, P. Thielemann, P. Asbeck, P.R. Bandaru, Enhanced Dielectric Constants and Shielding Effectiveness of Uniformly Dispersed, Functionalized Carbon Nanotube Composites, Appl Phys Lett. 94 (2009) 243111. https://doi.org/10.1063/1.3156032.

[110] J.-M. Thomassin, C. Jérôme, T. Pardoen, C. Bailly, I. Huynen, C. Detrembleur, Polymer/Carbon Based Composites as Electromagnetic Interference (EMI) Shielding Materials, Materials Science and Engineering R. 74 (2013) 211–232. https://doi.org/10.1016/J.MSER.2013.06.001.

[111] J.-H. Lin, Z.-I. Lin, Y.-J. Pan, C.-L. Huang, C.-K. Chen, C.-W. Lou, Polymer Composites Made of Multi-Walled Carbon Nanotubes and Graphene Nano-Sheets: Effects of Sandwich Structures on Their Electromagnetic Interference Shielding Effectiveness, Compos B Eng. 89 (2016) 424–431. https://doi.org/10.1016/j.compositesb.2015.11.014.

[112] D.D.L. Chung, Carbon Materials for Structural Self-Sensing, Electromagnetic Shielding and Thermal Interfacing, Carbon 50 (2012) 3342–3353. https://doi.org/10.1016/j.carbon.2012.01.031.

[113] F. Wu, Q. Zeng, Y. Xia, M. Sun, A. Xie, The Effects of Annealing Temperature on The Permittivity and Electromagnetic Attenuation Performance of Reduced Graphene Oxide, Appl Phys Lett. 112 (2018) 192902. https://doi.org/10.1063/1.5028472.

[114] S.-T. Hsiao, C.-C.M. Ma, W.-H. Liao, Y.-S. Wang, S.-M. Li, Y.-C. Huang, R.-B. Yang, W.-F. Liang, Lightweight and Flexible Reduced Graphene Oxide/Water-Borne Polyurethane Composites with High Electrical Conductivity and Excellent Electromagnetic Interference Shielding Performance, ACS Appl Mater Interfaces. 6 (2014) 10667–10678. https://doi.org/10.1021/am502412q.

[115] J. Dalal, S. Lather, A. Gupta, S. Dahiya, A.S. Maan, K. Singh, S.K. Dhawan, A. Ohlan, EMI Shielding Properties of Laminated Graphene and $PbTiO_3$ Reinforced Poly(3,4-ethylenedioxythiophene) Nanocomposites, Compos Sci Technol. 165 (2018) 222–230. https://doi.org/10.1016/J.COMPSCITECH.2018.07.016.

[116] W. Yang, Z. Zhao, K. Wu, R. Huang, T. Liu, H. Jiang, F. Chen, Q. Fu, Ultrathin Flexible Reduced Graphene Oxide/Cellulose Nanofiber Composite Films with Strongly Anisotropic Thermal Conductivity and Efficient Electromagnetic Interference Shielding, J Mater Chem C Mater. 5 (2017) 3748–3756. https://doi.org/10.1039/C7TC00400A.

[117] F. Sharif, M. Arjmand, A.A. Moud, U. Sundararaj, E.P.L. Roberts, Segregated Hybrid Poly(methyl methacrylate)/Graphene/Magnetite Nanocomposites for Electromagnetic Interference Shielding, ACS Appl Mater Interfaces. 9 (2017) 14171–14179. https://doi.org/10.1021/acsami.6b13986.

[118] H.M. Mesfin, A.C. Baudouin, S. Hermans, A. Delcorte, I. Huynen, C. Bailly, Frequency Selective Microwave Absorption Induced by Controlled Orientation of Graphene-Like Nanoplatelets in Thin Polymer Films, Appl Phys Lett. 105 (2014) 103105. https://doi.org/10.1063/1.4895674.

[119] Y. Li, B. Shen, D. Yi, L. Zhang, W. Zhai, X. Wei, W. Zheng, The Influence of Gradient and Sandwich Configurations on the Electromagnetic Interference Shielding Performance of Multilayered Thermoplastic Polyurethane/Graphene Composite Foams, Compos Sci Technol. 138 (2017) 209–216. https://doi.org/10.1016/J.COMPSCITECH.2016.12.002.

[120] A. Plyushch, J. MacUtkevic, S. Svirskas, J. Banys, V. Plausinaitiene, D. Bychanok, S.A. Maksimenko, A. Selskis, A. Sokal, K.N. Lapko, P.P. Kuzhir, Silicon Carbide/Phosphate Ceramics Composite for Electromagnetic Shielding Applications: Whiskers vs Particles, Appl Phys Lett. 114 (2019) 183105. https://doi.org/10.1063/1.5093421.

[121] B. Zhao, S. Wang, C. Zhao, R. Li, S.M. Hamidinejad, Y. Kazemi, C.B. Park, Synergism between Carbon Materials and Ni Chains in Flexible Poly(vinylidene fluoride) Composite Films with High Heat Dissipation to Improve Electromagnetic Shielding Properties, Carbon 127 (2018) 469–478. https://doi.org/10.1016/J.CARBON.2017.11.032.

[122] Q. Song, F. Ye, X. Yin, W. Li, H. Li, Y. Liu, K. Li, K. Xie, X. Li, Q. Fu, L. Cheng, L. Zhang, B. Wei, Carbon Nanotube–Multilayered Graphene Edge Plane Core–Shell Hybrid Foams for Ultrahigh-Performance Electromagnetic-Interference Shielding, Advanced Materials. 29 (2017) 1701583. https://doi.org/10.1002/adma.201701583.

[123] J. Liang, Y. Wang, Y. Huang, Y. Ma, Z. Liu, J. Cai, C. Zhang, H. Gao, Y. Chen, Electromagnetic Interference Shielding of Graphene/Epoxy Composites, Carbon 47 (2009) 922–925. https://doi.org/10.1016/j.carbon.2008.12.038.

[124] C. Lan, L. Zou, Y. Qiu, Y. Ma, Tuning Solid–Air Interface of Porous Graphene Paper for Enhanced Electromagnetic Interference Shielding, J Mater Sci. 55 (2020) 6598–6609. https://doi.org/10.1007/s10853-020-04433-9.

[125] C. Pavlou, M.G. Pastore Carbone, A.C. Manikas, G. Trakakis, C. Koral, G. Papari, A. Andreone, C. Galiotis, Effective EMI Shielding Behaviour of Thin Graphene/PMMA Nanolaminates in the THZ Range, Nat Commun. 12 (2021). https://doi.org/10.1038/s41467-021-24970-4.

[126] P. Chamorro-Posada, J. Vázquez-Cabo, Ó. Rubiños-López, J. Martín-Gil, S. Hernández-Navarro, P. Martín-Ramos, F.M. Sánchez-Arévalo, A. V. Tamashausky, C. Merino-Sánchez, R.C. Dante, THz TDS Study of Several sp^2 Carbon Materials: Graphite, Needle Coke and Graphene Oxides, Carbon 98 (2016) 484–490. https://doi.org/10.1016/J.CARBON.2015.11.020.

[127] A. Tredicucci, M.S. Vitiello, Device Concepts for Graphene-Based Terahertz Photonics, IEEE Journal on Selected Topics in Quantum Electronics. 20 (2014). https://doi.org/10.1109/JSTQE.2013.2271692.

[128] R. Cheng, Y. Zhou, H. Liu, J. Liu, G. Sun, X. Zhou, H. Shen, Q. Wang, Y. Zha, Tunable Graphene-Based Terahertz Absorber via an External Magnetic Field, Opt Mater Express. 10 (2020) 501. https://doi.org/10.1364/ome.384147.

[129] A.M. Mahjoub, S. Motooka, N. Aoki, J. Song, J.P. Bird, Y. Kawano, D.K. Ferry, K. Ishibashi, Y. Ochiai, Towards Graphene GHz/THz Nanosensor, Jpn J Appl Phys. 50 (2011) 070119. https://doi.org/10.1143/JJAP.50.070119/XML.

[130] V. Ryzhii, T. Otsuji, M. Shur, Graphene Based Plasma-Wave Devices for Terahertz Applications, Appl Phys Lett. 116 (2020) 140501. https://doi.org/10.1063/1.5140712.

[131] V. Ryzhii, M. Ryzhii, V. Mitin, M.S. Shur, T. Otsuji, Negative Terahertz Conductivity in Remotely Doped Graphene Bilayer Heterostructures, J Appl Phys. 118 (2015) 183105. https://doi.org/10.1063/1.4934856.

[132] J.-L. Coutaz, F. Garet, V.P. Wallace, Principles of Terahertz Time-Domain Spectroscopy, CRC Press, 2018.

[133] N. Vieweg, F. Rettich, A. Deninger, H. Roehle, R. Dietz, T. Göbel, M. Schell, Terahertz-Time Domain Spectrometer with 90 dB Peak Dynamic Range, Journal of Infrared, Millimeter, and Terahertz Waves 2014 35:10. 35 (2014) 823–832. https://doi.org/10.1007/S10762-014-0085-9.

[134] J. Neu, C.A. Schmuttenmaer, Tutorial: An introduction to Terahertz Time Domain Spectroscopy (THz-TDS), J Appl Phys. 124 (2018) 231101. https://doi.org/10.1063/1.5047659.

[135] S.L. Dexheimer, Terahertz Spectroscopy: Principles and Applications, CRC press, 2017.

[136] Z.-S. Wu, W. Ren, L. Gao, B. Liu, C. Jiang, H.-M. Cheng, Synthesis of High-Quality Graphene with a Pre-Determined Number of Layers, Carbon 47 (2009) 493–499. https://doi.org/10.1016/J.CARBON.2008.10.031.

[137] J.S. Lewis, Z. Barani, A.S. Magana, F. Kargar, A.A. Balandin, Thermal and Electrical Conductivity Control in Hybrid Composites with Graphene and Boron Nitride Fillers, Mater Res Express. 6 (2019) 085325. https://doi.org/10.1088/2053-1591/ab2215.

[138] L. Colombo, X. Li, B. Han, C. Magnuson, W. Cai, Y. Zhu, R.S. Ruoff, Growth Kinetics and Defects of CVD Graphene on Cu, ECS Trans. 28 (2010) 109–114. https://doi.org/10.1149/1.3367942.

[139] K.F. Mak, J. Shan, T.F. Heinz, Seeing Many-Body Effects in Single- And Few-Layer Graphene: Observation of Two-Dimensional Saddle-Point Excitons, Phys Rev Lett. 106 (2011) 046401. https://doi.org/10.1103/PhysRevLett.106.046401.

[140] J. Lloyd-Hughes, T.-I. Jeon, A Review of the Terahertz Conductivity of Bulk and Nano-Materials, Journal of Infrared, Millimeter, and Terahertz Waves (2012) 871–925. https://doi.org/10.1007/S10762-012-9905-Y.

[141] T. Unuma, K. Fujii, H. Kishida, A. Nakamura, Terahertz Complex Conductivities of Carriers with Partial Localization in Doped Polythiophenes, Appl Phys Lett. 97 (2010) 033308. https://doi.org/10.1063/1.3466916.

[142] H. Xu, X. Yin, X. Li, M. Li, S. Liang, L. Zhang, L. Cheng, Lightweight Ti_2CT_x MXene/Poly(vinyl alcohol) Composite Foams for Electromagnetic Wave Shielding with Absorption-Dominated Feature, ACS Appl Mater Interfaces. 11 (2019) 10198–10207. https://doi.org/10.1021/ACSAMI.8B21671.

[143] Q. Zou, C. Shi, B. Liu, D. Liu, D. Cao, F. Liu, Y. Zhang, W. Shi, Enhanced Terahertz Shielding by Adding Rare Ag Nanoparticles to $Ti_3C_2T_x$ MXene Fiber Membranes, Nanotechnology. 32 (2021) 415204. https://doi.org/10.1088/1361-6528/ac1296.

[144] Z. Zhang, M. Zhou, T. Zhang, M. Yang, Q. Yang, J. Yu, Y. Zhang, Few-Layer Borophene Prepared by Mechanical Resonance and Its Application in Terahertz Shielding, ACS Appl Mater Interfaces. 12 (2020) 19746–19754. https://doi.org/10.1021/acsami.9b19407.

[145] Y. Hernandez, V. Nicolosi, M. Lotya, F.M. Blighe, Z. Sun, S. De, I.T. McGovern, B. Holland, M. Byrne, Y.K. Gun'Ko, J.J. Boland, P. Niraj, G. Duesberg, S. Krishnamurthy, R. Goodhue, J. Hutchison, V. Scardaci, A.C. Ferrari, J.N. Coleman, High-Yield Production of Graphene by Liquid-Phase Exfoliation of Graphite, Nat Nanotechnol. 3 (2008) 563–568. https://doi.org/10.1038/nnano.2008.215.

[146] M. Lotya, Y. Hernandez, P.J. King, R.J. Smith, V. Nicolosi, L.S. Karlsson, F.M. Blighe, S. De, Z. Wang, I.T. McGovern, G.S. Duesberg, J.N. Coleman, Liquid Phase

Production of Graphene by Exfoliation of Graphite in Surfactant/Water Solutions, J Am Chem Soc. 131 (2009) 3611–3620. https://doi.org/10.1021/ja807449u.

[147] S. Stankovich, D.A. Dikin, R.D. Piner, K.A. Kohlhaas, A. Kleinhammes, Y. Jia, Y. Wu, S.B.T. Nguyen, R.S. Ruoff, Synthesis of Graphene-Based Nanosheets via Chemical Reduction of Exfoliated Graphite Oxide, Carbon 45 (2007) 1558–1565. https://doi.org/10.1016/j.carbon.2007.02.034.

[148] F. Kargar, Z. Barani, R. Salgado, B. Debnath, J.S. Lewis, E. Aytan, R.K. Lake, A.A. Balandin, Thermal Percolation Threshold and Thermal Properties of Composites with High Loading of Graphene and Boron Nitride Fillers, ACS Appl Mater Interfaces. 10 (2018) 37555–37565. https://doi.org/10.1021/acsami.8b16616.

[149] Z. Barani, A. Mohammadzadeh, A. Geremew, C.Y. Huang, D. Coleman, L. Mangolini, F. Kargar, A.A. Balandin, Thermal Properties of the Binary-Filler Hybrid Composites with Graphene and Copper Nanoparticles, Adv Funct Mater. 30 (2020) 1904008. https://doi.org/10.1002/adfm.201904008.